DM

From Copper-based Nanoparticles to Carbon-based Dots

MASTER DISSERTATION

Joaquim Duarte Gonçalves Fernandes
MASTER IN NANOCHEMISTRY AND NANOMATERIALS

UNIVERSIDADE da MADEIRA
A Nossa Universidade
www.uma.pt

January | 2019

From Copper-based Nanoparticles to Carbon-based Dots

MASTER DISSERTATION

Joaquim Duarte Gonçalves Fernandes
MASTER IN NANOCHEMISTRY AND NANOMATERIALS

SUPERVISOR
Pedro Filipe Duarte Louzeiro Pires

CO-SUPERVISOR
Carla Sophia Brazão Andrade Sousa Alves

From Copper-based Nanoparticles to Carbon-based Dots

Dissertation submitted to the University of Madeira in fulfilment of the requirements for the degree of Master in Nanochemistry and Nanomaterials

by Joaquim Duarte Gonçalves Fernandes

Work developed under the supervision of
Prof. Pedro Filipe Duarte Louzeiro Pires and
co-supervised by Dr. Carla Sophia Brazão Andrade Sousa Alves

Faculdade de Ciências Exatas e de Engenharia,
Centro de Química da Madeira,
Campus Universitário da Penteada, 9000-390 Funchal, Portugal

January 2019

Declaration

I hereby declare that this thesis is the result of my own work, is original and was written by me. I also declare that its reproduction and publication by the University of Madeira will not break any third party rights and that I have not previously (in its entirety or in part) submitted it elsewhere for obtaining any qualification or degree. Furthermore, I certify that all the sources of information used in the thesis were properly cited.

Funchal, 14th January of 2019

Duarte Fernandes

Conference Contributions

Part of the results and findings of this work were presented at the following scientific meetings:

Oral Communications

Duarte Fernandes, Pedro Pires, Carla S. Alves. Preparation and Characterization of Copper-based Nanoparticles. **5th CQM Annual Meeting**, held at the University of Madeira (Portugal), O-06, page 24, 01st - 03rd of February of 2018.

Poster Communications

Duarte Fernandes, Pedro Pires, Carla S. Alves. Supported Copper-based Nanoparticles – An Ascorbic Acid Redox Approach. **Mad-Nano18: Madeira International Conference on Emerging Trends and Future of Nanomaterials for Human Health**, held in Funchal, Madeira (Portugal), PC6, page 56, from November 30th to December 02nd of 2018.

Acknowledgments

I would like to express my gratitude to all the people and institutions that have contributed in some way throughout the course of this work.

Firstly, and foremost, I want to deeply thank both my supervisor Prof. Pedro Pires and my co-supervisor Dr. Carla S. Alves for all their motivation and guidance in the various aspects and stages of this thesis.

A special thanks to Dr. Manuel Algarra for all the support provided regarding the C-Dots studies. To all the teachers of this master degree, Prof. João Rodrigues, Prof. Helena Tomás, Prof. Pedro Pires, Cláudia Camacho, Prof. José Câmara, Prof. Xiangyang Shi, Dr. Carla S. Alves, Prof. Serge Mignani and Dr. César Fernandes, I want to appreciate all the knowledge provided during the various courses. I also want to mention Prof. Paula Castilho and Prof. Carlos Mesquita for the academic discussions about concepts related with organic chemistry and electrochemistry, respectively.

Especially to Nilsa Abreu and Lydia dos Orfãos, but also to my other master colleagues Natacha Antunes, Mariana Santos, Ivo Martins and Gina Tavares, I would like to thank them for their friendship, advice, and academic discussions.

I also want to thank all other members of the Centro de Química da Madeira (CQM), who also gave me their advice, support in the lab work and words of encouragement, especially to Ana Olival, Beatriz Andrade, Carla Miguel, Cláudia Camacho, Dina Maciel, Rita Castro, Mara Gonçalves, Nádia Nunes, and Nilsa Oliveira. Also, I want to thank the laboratory technicians Paula Andrade and Paula Vieira, the SEM technicians Carla Miguel and Radenka Whiffen and the NMR technician Ana Olival for their support.

I also express my gratitude to the CQM and the University of Madeira for providing all the reagents, materials, equipment, and facilities for the development of this project.

I would like to extend my thanks to Fundação para a Ciência e a Tecnologia (FCT, Portuguese Government funds) through the CQM Strategic Project PEst-OE/QUI/UI0674/2013, to the Madeira 14-20 Program, project PROEQUIPRAM - Reforço do Investimento em Equipamentos e Infraestruturas Científicas na RAM (M1420-01-0145-FEDER-000008), and to Agência Regional para o Desenvolvimento da Investigação, Tecnologia e Inovação (ARDITI) thought the project M1420-01-0145-FEDER-000005 - Centro de Química da Madeira - CQM^{+} (Madeira 14-20 Program).

Abstract

Nanoparticles (NPs) prepared from earth-abundant metals have attracted significant consideration for their potential as viable replacements for expensive metals used in many commercial chemical processes. In this context, copper NPs are particularly appealing since copper (Cu) is vastly abundant and cheap. Cu also displays good electronic, optical, antimicrobial, and chemical properties. Yet, CuNPs are limited due to their intrinsic instability under atmospheric conditions, making them prone to oxidation. Various efforts have been made to increase the stability of CuNPs, including investigating Cu-based NPs associated with organic structures such as polymers.

This project was focused on the preparation and characterization of long-term stable Cu-based NPs using different synthesis strategies and without employing harmful reagents or solvents. Based on previously reported methods, the particles were synthesized using the environmentally friendly ascorbic acid (AA) as a reducing agent. Polyamidoamine (PAMAM) dendrimers and polyvinylpyrrolidone (PVP) were used as both templates and capping agents, and the reactions were done at room temperature and 60°C.

The samples were characterized using various techniques, including Ultraviolet-Visible Spectroscopy (UV-Vis) and Scanning Electron Microscopy (SEM) coupled with Energy-Dispersive X-ray Analysis (EDX). The results indicated the presence of Cu^0, Cu^{1+}, and Cu^{2+}-based particles with diverse shapes (e.g. polyhedral, spherical, and disk-like).

Moreover, other techniques like Photoluminescence Spectroscopy (PL), X-ray Photoelectron Spectroscopy (XPS), and Transmission Electron Microscopy (TEM) indicated the presence of Carbon-based Dots (C-Dots), which are responsible for the fluorescence properties of the solution. The formation of the C-Dots is thought to be the result of the side reaction of the reduction of the Cu ions (*i.e.*, the oxidation of AA).

Preliminary cytotoxic evaluation studies using the MTT assay showed that the particles obtained using PAMAM and PVP, as well as the C-Dots, did not present significant toxicity towards HEK 293T cells at concentrations below 500, 5, and 200µg/mL, respectively.

Keywords

Copper Nanoparticles, Polyvinylpyrrolidone (PVP), Polyamidoamine (PAMAM), Ascorbic Acid, Carbon-based Dots.

Resumo

As nanopartículas (NPs) preparadas a partir de metais relativamente abundantes têm atraído uma atenção considerável como potenciais substitutos para outros metais de elevado custo usados em muitos processos químicos comerciais. Neste contexto, as NPs de cobre (CuNPs) são particularmente apelativas, uma vez que o cobre é mais abundante e barato que outros metais. O cobre também apresenta boas propriedades eletroquímicas, óticas e antimicrobianas. No entanto, as CuNPs estão limitadas pela sua instabilidade intrínseca em condições atmosféricas, tornando-as suscetíveis à oxidação. Vários esforços têm sido realizados para aumentar a estabilidade das CuNPs, incluindo a criação de NPs com estruturas orgânicas (ex. polímeros) associadas.

Este projeto foca-se na preparação e caracterização de partículas de cobre com estabilidade a longo prazo. Além disso, pretende-se usar diferentes estratégias de síntese sem utilizar reagentes ou solventes prejudiciais para a saúde ou ambiente. Tendo por base alguns métodos descritos na literatura, vários tipos de partículas foram sintetizados usando o ácido ascórbico (AA) como agente redutor ecológico. Dendrímeros da família da poliamidoamina (PAMAM), e a polivinilpirrolidona (PVP) foram utilizados para suportar e estabilizar as partículas, permitindo controlar o tamanho e a forma das mesmas. As reações foram realizadas tanto à temperatura ambiente como a 60°C.

As amostras foram caracterizadas usando várias técnicas como a espectroscopia de ultravioleta-visível (UV-Vis) e a microscopia eletrónica de varrimento (SEM) acoplada à espectroscopia de raios X por dispersão em energia (EDX). Os resultados sugerem a presença de partículas à base de cobre metálico (zero), cobre (I) e cobre (II) com formas variadas (ex. poliédricas, esféricas e em forma de disco).

Além disso, a espectroscopia de fotoluminescência, a espectroscopia de fotoeletrões excitados por raios-X (XPS), e a microscopia eletrónica de transmissão (TEM) indicaram a presença de NPs de carbono ("*Carbon-based Dots*", C-Dots) em solução. Estes são responsáveis pelas propriedades de fluorescência observadas nas amostras. A formação dos C-Dots poderá ser o resultado de reações secundárias à redução dos iões de cobre, *i.e.*, oxidação do AA.

Uma avaliação preliminar da citotoxicidade de algumas partículas foi realizada usando células da linha celular HEK 293T. A análise indicou que as partículas obtidas usando o PAMAM e PVP, assim como os C-Dots não apresentam uma toxicidade apreciável em concentrações inferiores a 500, 5 e 200µg/mL, respetivamente.

Palavras-Chave:

Nanopartículas de Cobre, Polivinilpirrolidona (PVP), Poliamidoamina (PAMAM), Ácido Ascórbico, Nanopartículas de Carbono.

.

Contents

From Copper-based Nanoparticles to Carbon-based Dots

List of Figures

Introduction

Materials and Methods

Results and Discussion

Annexes

List of Tables

Introduction

Materials and Methods

Results and Discussion

List of Acronyms, Abbreviations, And Symbols

A

$A^{\bullet-}$	Ascorbate radical
AA	Ascorbic acid
AAeq	AA molar equivalents to Cu^{2+}
AmIP	1-Amino-2-propanol

C

C-Dots	Carbon-based dots
CDs	(Fluorescent) carbon NPs / carbon dots
CNDs	Carbon nanodots
CNT	Carbon nanotubes
CQD	Carbon quantum dots
CTAB	Cetyltrimethylammonium chloride

D

D_2O	Deuterium oxide / Deuterated water
DENPs	Dendrimer Entrapped NPs
DHA	Dehydroascorbic acid
DKG	2,3-Diketo-L-gulonic acid
DLS	Dynamic Light Scattering
DMEM	Dulbecco's Modified Eagle's Medium
DMSO	Dimethyl sulfoxide
dsDNA	Double strain DNA

E

E°	Redox potentials (E vs SHE)
EDTA	Ethylenediaminetetraacetic acid
EDX	Energy Dispersed X-ray spectroscopy
EEM	Excitation Emission Matrix
Eg	Energy band gap
EG	Ethylene glycol
ELS	Electrophoretic Light Scattering
ENDOR	Electron Nuclear Double Resonance

F

F	Faraday constant
FA	Folic acid / Folate
FBS	Fetal bovine serum
FLG	Few-layer (2-5) graphene
FTIR	Fourier-Transform Infrared spectroscopy

G

g	Standard acceleration due to gravity, $g = 9.80665\ m/s^2$
Gn	Generation n / n^{th} generation
GNR	Graphene nanoribbon
GO	Graphene oxide
GQD	Graphene quantum dot

H

H_2A	Fully reduced AA
HA^-	Deprotonated H_2A
HR-TEM	High-resolution transmission electron microscopy

I

IPA	Isopropyl alcohol

M

MLG	Multi-layer (2-10) graphene
MTT	3-4,5-dimethylthiazol-2-yl-2,5-diphenyltetrazolium bromide
MWCO	Molecular Weight Cut-Of

N

NMR	Nuclear Magnetic Resonance
NPs	Nanoparticles
NVP	N-vinylpyrrolidone (PVP monomer)
NVPeq	NVP molar equivalents to Cu^{2+}

P

PAA	Polyacrylic acid
PAMAM	Polyamidoamine
PB	Phosphate buffer
PBS	Phosphate buffer saline
PEG	Polyethylene glycol
PL	Photoluminescence
PPh_3	Triphenylphosphine / Triphenylphosphane
PPI	Polypropyleneimine
PVA	Polyvinyl alcohol
PVP	Polyvinylpyrrolidone

Q

QDs	Quantum Dots

R

rGO	Reduced graphene oxide
ROS	Reactive oxygen species
RT	Room temperature

S

SDS	Sodium dodecyl sulfate
SEM	Scanning Electron Microscopy
SFS	Sodium formaldehyde sulfoxylate
SQDs	Semiconductor-based QDs

T

TBAB	Tetra-butylamine borane
TOAB	Tetraoctylammonium bromide

U

UV-Vis	Ultraviolet-Visible spectroscopy

X

XPS	X-ray photoelectron spectra

Others

$^{em}\lambda$	Emission wavelength
$^{ex}\lambda$	Excitation wavelength
γ	Gamma
Å	Angstrom / Ångström, 1 Å = 0.1nm

1 Introduction

1.1 Copper-based nanoparticles – Background

Copper (Cu), especially in the zero-valence or metallic state (Cu^0), is a particularly appealing metal since it has unique antimicrobial, electronic, optical, and chemical properties, similar to silver (Ag) and gold (Au), but it is vastly more abundant (relative earth crust abundance is 68ppm) and cheap[1–9]. Usually, it is found as either a sulfide, oxide or carbonate in its major ores: chalcopyrite (~50% of all Cu deposits, $CuFeS_2$), chalcocite (Cu_2S), cuprite (Cu_2O) and malachite ($Cu_2CO_3(OH)_2$)[9]. Cu-based materials are associated with a diversity of reactions owing to a series of oxidation states (Cu^0, Cu^+, and Cu^{2+}) that allow Cu to react via both one and two electron pathways (**Fig. 1**)[10].

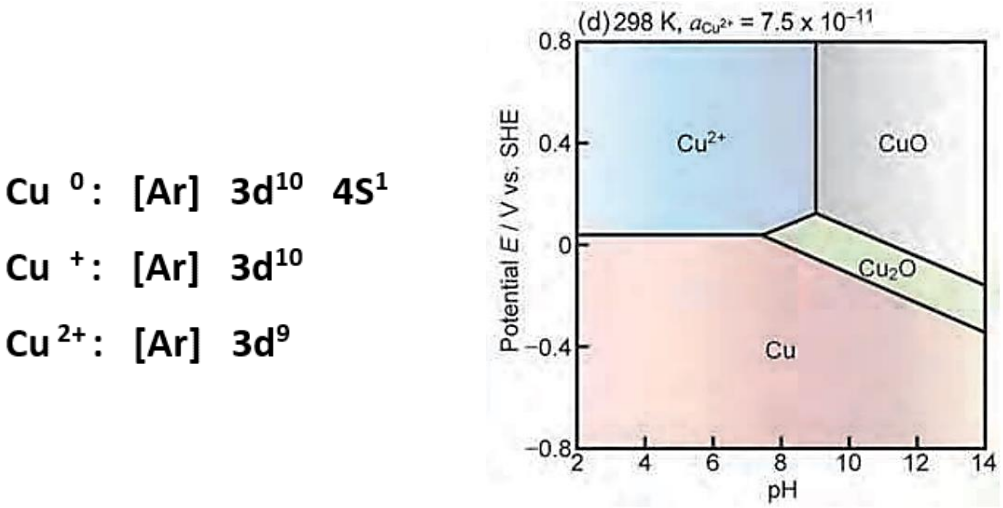

Fig. 1. (**Left**) Ground state of Cu in different oxidations states. (**Right**) Simplified potential-pH diagram (Pourbaix diagram) for the Cu^{2+}, CuO, Cu_2O and Cu^0 species at 25°C and Cu^{2+} activity of 7.5 x 10 $^{-11}$ (adapted from [11]).

Cu has a plentiful catalytic chemistry as well as a high boiling point that tolerates high temperatures and pressures. Hence it may be employed in several chemical reactions. An overview of the diverse chemical reactions in which Cu is involved can be found in **Table 1**.

Table 1. Chemical reactions involving the use of Cu-based materials as catalysts.

Field	Reaction	Example
Coupling Reactions	Click Chemistry (Huisgen 1,3-Dipolar cycloaddition)	Cu (0, I & II) NPs[12,13]
	Diels-Alder reactions	Various Cu complexes[14]
	Aryl-sulfur bond formation	Cu^0-NPs[15]
	Phosphine-Free Heck coupling	CuO Nanocomposites[16]
Redox Reactions	Oxidant-free dehydrogenation of alcohols	Cu^0-NPs[17]
	Hydrogenation of carbonyl compounds to alcohols	Cu^0-NPs[18]
	CO_2 hydrogenation to methanol	Cu-based NPs[19]
Gas-phase Catalysis	CO oxidation	Cu/CuO[20]
	NO_x reduction	Cu/Zeolite[21]
	Water–gas shift reaction	Cu/SiO_2 NPs[22]
Photocatalysis	Water splitting - Hydrogen Evolution Reaction (HER)	TiO_2@Cu-based NPs[23]
	Self-Cleaning (oxidize organics into CO_2 and H_2O)	Cu_2O microcrystals[24]
Others	Glycerol hydrogenolysis	Cu/SiO_2 NPs[25]
	Water splitting - Oxygen Evolution Reaction (OER)	Cu@($Cu(OH)_2$-CuO)[26]

Copper oxides (**Fig. 2**) are intrinsically p-type semiconductors with two stable phases, namely cubic (cuprous oxide, Cu_2O) and monoclinic (cupric oxide, CuO), as well as a metastable tetragonal (paramelaconite, Cu_4O_3) phase[27,28]. Copper (I) oxide (Cu_2O) has been shown to be used in several applications: solar energy conversion[29], energy storage (electrode materials)[30], supercapacitors[31], sensors[32], and catalysis (**Table 1**). For example, Cu_2O has been used as a photocatalyst for the decomposition of water into oxygen (O_2) and hydrogen (H_2) under visible light irradiation[10,33,34]. On the other hand, copper (II) oxide (CuO) may be related with electronics/spintronics[35], catalysis[36], energy storage (electrode materials)[30], sensors[32], and water purification[37]. The majority of binary oxides (e.g. ZnO, SnO_2, Ga_2O_3, In_2O_3) have quite wide energy band gaps (Eg) making them conveniently transparent semiconducting compounds. In the case of Cu oxides, they present band gaps in the visible region of the spectrum between 500 to 700nm (Eg_{Cu2O} = 2.1eV; Eg_{CuO} = 1.4eV)[27,28].

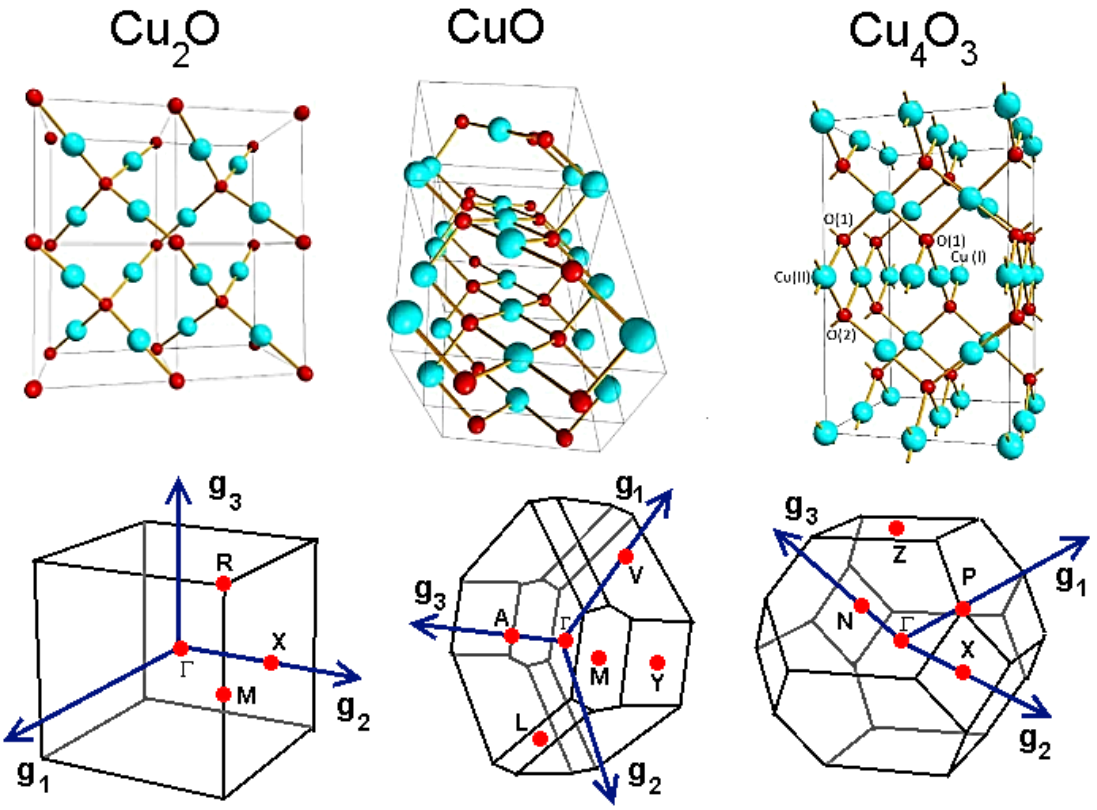

Fig. 2. From left to right, schematic crystalline structures of Cu_2O, CuO, and Cu_4O_3 (adapt.[27,28]).

Nanoparticles (NPs) prepared from cheap and earth-abundant metals have attracted significant consideration for their potential as viable replacements to the rare and expensive metals used in many conventional commercial chemical processes[38]. These metal NPs often exhibit different activity from that of their equivalent bulk materials depending on their size and shape (e.g. larger surface-to-volume ratio and quantum properties)[8,39]. Since a great number of atoms in metal NPs are on the surface, frequently as the NP size decreases there is an increase in reactivity efficiency but also a simultaneous addition of dangling bonds that promote aggregation[8,40].

Despite the applications of bulk Cu in various fields, the use of CuNPs instead of AgNPs or AuNPs is limited by their intrinsic sensitivity towards oxygen, which makes them unstable under normal atmospheric conditions[7,10,39]. The adsorption of stabilizers onto CuNPs has been shown to successfully decrease the degree of NP agglomeration by lowering the surface energy and protecting the metal from oxidation, at the same time inducing catalytic poisoning of the metal surface by inhibiting the interactions on the surface of the metal[39–41].

Cu^0-NPs have prospective applications in many fields including the manufacture of sensors[42–47], imaging probes[46–51], conductive/electronic materials (e.g. inks, nanowires)[27,52–55], antimicrobial/antifouling agents[8,56–59], and others. Small sized Cu has been used for a long time in various cultures and those practices are still used today. The Vikings knew that using strings of Cu and Ag on their ship hulls, below the water-line would prevent the growth of barnacles and algae[56]. Cu_2O NPs possess properties comparable to azurite ($Cu_3(CO_3)_2(OH)_2$), which is often used in natural Chinese medicine for its potential antitumor properties[60]. In Deruta, in the 15th and 16th centuries, people unknowingly used NPs of precious metals like Cu to manufacture glazes by applying a mixture of metal salts, vinegar, and clay onto the surface of pottery[61].

Metal NPs made of Cu, Ag, Au, and titanium (Ti) are of particular interest as they have been shown to possess antimicrobial properties against *Spirogyra, Aspergillus niger*, *Bacillus subtilis*, and *Staphylococcus aureus*, even when using low concentrations. This property holds greater appeal in cases where microbes display an increased resistance to frequently used antimicrobial agents. This means that CuNPs have prospective applications in lotions, medicine (e.g. dental), and other coatings[8,56,62]. In this regard, stand-alone[57] and polymer[58] or sepiolite[59] stabilized Cu_2O NPs have also been developed and effectively used as antimicrobial agents for waste water treatment.

1.2 Synthesis routes – Overview

Generally, the synthesis of NPs can follow two base approaches: bottom-up or top-down. The bottom-up synthesis approach however is preferable since it is easier to control the particle size homogeneity, leading to a more monodispersed final product, only by changing the synthesis conditions. Various efforts have been made to develop methods that can increase the stability of CuNPs and at the same time provide control over the cluster size and size distribution. A common practice for instance is to associate Cu-based NPs with organic molecules or ions as either (**1**) protective agents (e.g. polymers such as polyvinylpyrrolidone (PVP), polyvinyl alcohol (PVA), and polyacrylic acid (PAA), (**2**) template structures (e.g. dendrimers, microemulsions or reverse micelles using surfactants like sodium dodecyl sulfate (SDS) or (**3**) other shape-altering molecules/ions (e.g. ethylene glycol (EG), cetyltrimethylammonium chloride (CTAB), sulphate (SO_4^{2-}), ammonium (NH_4^+), nitrate (NO_3^-), and hydroxyl (OH^-). Moreover, even without extra additives, the optimization of the synthesis conditions (e.g. temperature, stirring) may be used to modify cluster nucleation, growth, and growth termination.

Electrodeposition[63–65], electroless deposition[66], gamma (γ) radiolysis[67], flame spray[51], hydrothermal[53,68], laser irradiation/ablation[69], sol-gel[70], vapor deposition[76], precipitation[71], thermal decomposition[71–73], sonoelectrochemical[70] are generally used to synthesize Cu-based NPs with various morphologies (**Table 2**), but also chemical reduction methods (**Table 3**). In some cases however these processes are time-consuming and costly, sometimes requiring specialized equipment[40,74]. Moreover, there is a tendency to work in non-aqueous media to prevent the Cu oxidation[75].

Siegfried and Choi studied the preferential adsorption of surfactants during an electrodeposition process to obtain various Cu polyhedral crystals ranging in shape from cubic to truncated octahedral. In their work, they were able to obtain a final Cu_2O crystal about 1µm in size by stabilizing different facets using different cationic and anionic ions. SDS and SO_4^{2-} were shown to lower the energy of the {111} planes, while NO_3^- stabilized the {100} planes and NH_4^+ favored the simultaneous advance of both {110} and {111} planes. Additionally, the action of SDS was observed to progressively weaken as the pH decreased from pH=3.9 to pH=3.4, leading to crystal growth in the <111> direction[64,65].

A green synthesis method was reported by Sastry, *et al.*, where inexpensive materials (e.g. lemon and tamarind juice, milk, and curd) were used as capping agents to produce Cu^0-NPs with Cu_2O shells (Cu^0@Cu_2O)[66]. Yeh *et al.* prepared Cu-based colloids from CuO powder in 2-propanol solutions. The samples were irradiated with a laser at 1064nm and at 532nm, without any precautions regarding capping agents or aerobic conditions[69]. Joshi *et al.* prepared CuNPs by irradiating copper salts with gamma rays (γ), which demonstrated significant advantages relative to the chemical reduction of metal ions. In this method, troubling impurities like Cu oxide were not present. Moreover, polymers and surfactants like PVP, PVA, CTAD, and SDS were used to protect the prepared NPs[67]. Rahimi-Nasrabadi *et al.* applied a Taguchi robust design to show the importance of some variables such as copper and sodium oxalate concentrations, and temperature on the formation of copper (II) oxalate (CuC_2O_4) nano-disks by chemical precipitation. These nano-disks, which had an approximate thickness of 60nm, were then used as a precursor for the formation of spherical CuO NPs (~55nm diameter) by thermal decomposition at 350°C[71]. Athanassiou *et al.* managed to produce CuNPs with a carbon coating of ~1nm (Cu@C). For this, a modified flame spray synthesis unit was used under highly reducing conditions to continuously produce up to 10g of particles per hour. The advantage of the carbon layer here is that the prepared CuNPs were protected from oxidation in air[52]. Haas *et al.* presented a method to obtain spherical CuNPs in a size-controlled manner by a novel sonoelectrochemical approach. The size of the NPs was shown to increase with the reaction time (10, 30, and 60min) and temperature (15, 25, and 60°C), but decrease with higher PVP concentrations (0.2, 1, and 2%)[76].

Table 2. Summary of some common methods used for the synthesis of Cu-based NPs.

Final Product	Method	Additives	Other Conditions	Ref.
Cu_2O wires or polyhedrons	Electrodeposition	PVP, EG, SDS, SO_4^{2-}, NH_4^+ NO_3^-	3.3≤pH≤4.9; 40-70°C; 0-90min	63–65
Cu^0@Cu_2O ~20-40nm	Electroless deposition (green synthesis)	Plant extracts, curd, buttermilk, and milk	pH~4; ~40°C; 15min	66
Cu_2O wires or 5-20nm polyhedrons	Hydrothermal	2,5- dimethoxyaniline, pyrrole, o-anisidine, or EDTA	pH 8 or 11; 120-180°C for 8-20h or 250°C for 5h	53,68
Cu^0@Cu_2O ~56nm	Laser irradiation or laser ablation	None	Not applicable (N/A)	69
Cu^0 ~20–80 nm	γ-radiolysis	PVA, PVP, CTAB, and SDS	2≤pH≤9, RT, and inert atmosphere	67
CuO ~20nm	Sol-gel	NaOH and acetic acid	pH=7; 100°C	70
CuC_2O_4-disks and CuO-NPs	Precipitation and thermal decomposition	Oxalate	0-60°C and 350°C for 4H	71
Cu^0-NPs ~7.5-30nm	Thermal decomposition	Oleate	Up to 300°C and 4h	72,73
Cu@C NPs 10-20nm	Flame spray	N/A	N/A	52
Cu^0@Cu_2O 20–45 nm	Vapor deposition	None	Freeze–thaw-pump cycles (vacuum, 77K)	77
Cu^0-NPs 10-65nm	Sonoelectrochemical	PVP	15-50°C; 10-60min	76

1.2.1 The redox method

The redox method is most commonly used to prepare CuNPs, probably because it involves a relatively inexpensive and simple approach. Strong reducing agents such as sodium borohydride ($NaBH_4$) and hydrazine (N_2H_4) are generally used to prepare CuNPs, but these reagents create pollution associated with manufacturing and the production of harmful by-products[40]. Examples of alternative reducing agents include ascorbic acid (AA), isopropyl alcohol (IPA), glucose, and sodium formaldehyde sulfoxylate (SFS).

Table 3 summarizes some studies that report the use of the redox method to fabricate Cu-based NPs at different oxidation states.

Chen and Wu used CTAB and N_2H_4 for the synthesis of very small Cu^0-NPs (5.1nm), which they reported to be stable for months in solution[78]. Ben Aissa *et al.* prepared low dispersity CuNPs by reducing a phosphine organometallic precursor, [$CuCl(PPh_3)_3$], using terta-butylamine borane (TBAB) in the presence of dodecylamine or oleylamine as capping agents. Moreover, the addition of oleic acid under nitrogen (N_2) atmosphere allowed for the stabilization of the prepared CuNPs for a few months. The exchange between triphenylphosphine (PPh_3) and oleic acid was evidenced without coalescence[79]. Murphy *et al.* prepared monodispersed nanocubes from the reduction of Cu^{2+} by AA using poly(ethylene) glycol (PEG, Mw=600) as a capping agent. Here, different NP sizes were obtained depending on the polymer concentration[80].

Table 3. Examples of redox methods for the synthesis of Cu-based particles.

Final Product	Reducing Agents	Additives	Other Conditions	Ref.
Cu^0_n clusters (~3 < n <1000)	$NaBH_4$	SO_4^{2-}, SDS, isopentanol	N_2(g)	81
Cu^0-NPs (40–80 nm)	$NaBH_4$	Starch, NH_4^+	pH=7; 30min; RT	82
Cu^0-NPs (~5nm, oxides impurities)	$NaBH_4$	1-Decyne	Ice or RT; N_2(g); 3h	83
Cu_n clusters (n≤8)	$NaBH_4$	Tetraoctylammonium bromide (TOAB), MPP, NO_3^-, OH^-	Ice and 80°C; 13h30min	84
Cu^0-NPs (<100nm)	$NaBH_4$	Acetonitrile, NO_3^-	Argon(g)	85
Spherical Cu^0 (~3-5 nm)	$NaBH_4$	1-Dodecanethiol, 1-octanethiol, 1-decanethiol, NO_3^-	RT; 2h; N_2(g)	86
Cu^0-NPs (~2 or ~6)	$NaBH_4$	SO_4^{2-}, CTAB, decanethiol	2h; RT	87
Cu^0-NPs (~5nm)	N_2H_4	CTAB, NH_4^+, Cl^-	2h; 25°C; pH=10	78
Cu^0-NPs (3.5 ± 1.0 nm)	N_2H_4	1-Amino-2-propanol (AmIP), EG	RT; 24h	55
Cu^0@Ag^0-NPs (~34nm)	N_2H_4	PAA, Ag, NO_3^-	N/A	88
Cu^0-NPs	N_2H_4 or SFS	Cl^-, PVA, Sodium citrate or myristic acid	30min at RT or 1.5h at 60°C	89
Cu^0-NPs (mostly pure)	N_2H_4	Sodium succinate, PVA	1h20m; RT, ~75°C or 120°C	90
Cu^0-NPs (Cu_2O impurities)	SFS	Sodium succinate, Cl^-	1h20m; ~75°C	90
Cu^0-NPs (2-20nm)	IPA	CTAB, NO_3^-	N/A	91
Cu^0-NPs (3.5-11nm)	TBAB	PPh_3, or oleic acid, and dodecylamine or oleylamine	50-100°C; N_2; 1 or 2h	79
Cu^0-NPs (~15nm)	Benzil-diethylenetriamine	NO_3^-	~2h (reflux ~55°C)	92
Cu^x-NPs (16, 23, 37nm)	IPA	CTAB, NO_3^-	RT	75
Cu^x-NPs (4-7nm)	$NaBH_4$	Carbon-based dots	2h, RT	93
Cu^x-NPs	AA	dsDNA	25, 37, and 70°C; ~1h	94
Cu_2O nanocubes (25, 50, 80nm)	AA	PEG, OH^-, SO_4^{2-}	36min; RT	80
Cu_2O MPS (150-250nm)	AA	Pluronic P123, NH_4^+, Cl^-	RT; 3h40min	95
Octahedral Cu_2O (130-150nm)	N_2H_4	OH^-, NH_4^+, Cl^-	20min	96
Spherical or octahedral Cu_2O	N_2H_4	OH^-, SO_4^{2-}, NO_3^-, Cl^-, or acetate	2-3h	97
Cu^0 or CuO-NPs (30-85nm)	N_2H_4 or $NaBH_4$	PAA or no PAA; and acetate, dodecyl ammonium	2h; water and heptane	98
CuO or Cu_2O multiple shapes	Glucose	Acetate, OH^-	70°C; >30min	99
Cu_2O polyhedrons (various)	Glucose	Oleic acid, SO_4^{2-}	1h; 100°C	100

1.2.2 The role of polymers

Polymers can be classified into different types according to their branching level, which may range from linear to cross-linked, branched, and dendritic (**Fig. 3**). In the case of dendritic architectures, they may further be classified as random hyperbranched, dendrons, dendrigrafts, and dendrimers. In this work, a dendrimer and a linear polymer were used to assist in the formation of CuNPs.

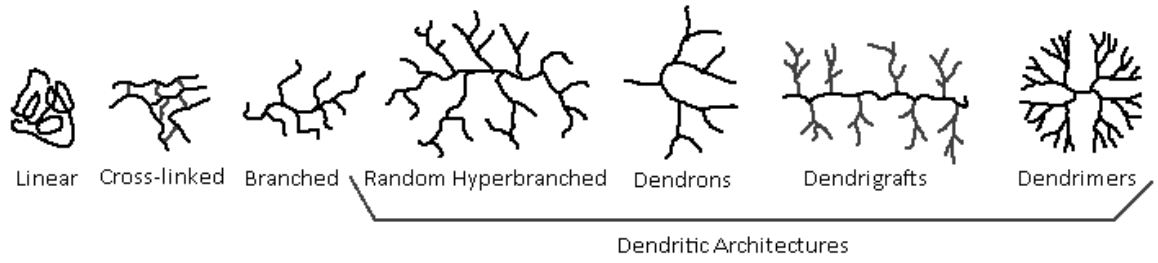

Fig. 3. Types of polymeric structures (adapt.[101]).

PVP is a chain made up of N-vinylpyrrolidone (NVP) monomeric units and as seen in **Table 2** and **Table 4**, it is often employed in the synthesis of CuNPs and is described as an effective capping agent, preventing the agglomeration and precipitation of NPs during the synthesis process[40,54]. Also, the formation of a PVP layer leads to a diffusion barrier that inhibits the growth (higher PVP concentrations will most likely lead to NPs with reduced size) and improves the stability (protects from the oxidation, perhaps even in the absence of inert atmosphere) of the NPs[40,54,63,102–104]. An obvious side-effect of this barrier is that it would decrease the catalytic activity of the metal surface[104].

The first step in using PVP in the synthesis of NPs involves the recognized capability of this polymer to coordinate Cu ions[63,76,102]. It has been proposed that the stabilization mechanism involved in this process is based on the structural features of PVP. The polyvinyl skeleton structure with nitrogen and oxygen-containing polar groups can donate lone-pair electrons, allowing for the formation of hybrid orbitals with Cu ions leading to the coordinative bond (**Fig. 4**)[40,76,102].

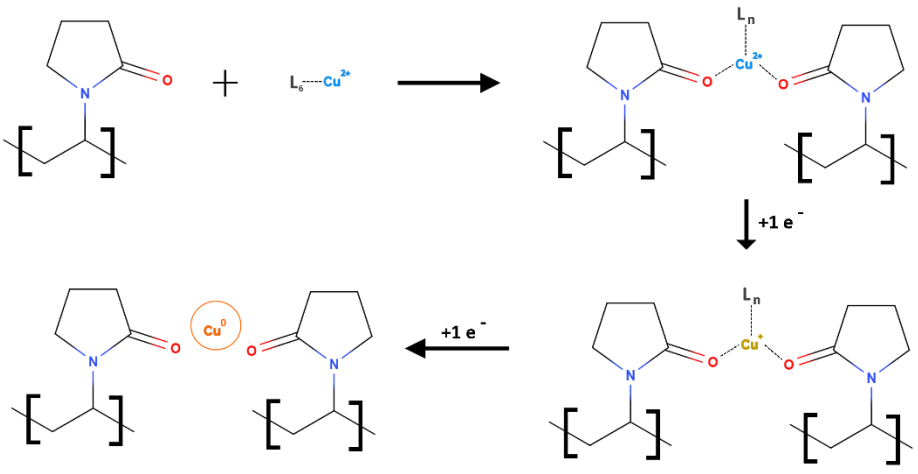

Fig. 4. Proposed schematic of Cu complexation and reduction when PVP is present (adapt.[76]).

PVP, which has been broadly employed as a non-ionic surfactant, can be used to control the morphology of NPs during synthesis by changing the amount of polymer added (**Table 4**). The polarized C=O group of PVP has a negatively charged O atom that would strongly interact with the exposed, positively charged Cu atoms[105,106].

Table 4. Different redox methods for the synthesis of CuNPs using PVP as capping agent.

Final Product	Additives	Reducing Agent	NVPeq*	Other Conditions	Ref.
Cu^{2+}-based needles (~2/0.5µm), Polyhedral Cu^0 (~1.5µm), Spherical Cu_2O (~300nm)	$CuSO_4$ (34mM), OH^- (for pH)	AA (2.5, 5, 10, or 15eq)	0, 4, 8, 12, or 16	pH 2, 4, or 7; RT for 7D or 60°C for 4h	here
Quasi-spherical Cu^0-NPs (~3nm)	$CuSO_4$ (0.9mM)	AA (10eq)	450	pH 6; RT; 6 days	107
Cu^0 nanobuds (~7nm)	$CuSO_4$ (≤3mM), OH^- (for pH)	AA (~3.4eq) and isoniazid	9	65°C; pH=7	40
Spherical Cu_2O (~500nm)	$CuAc_2$ (50mM)	AA (~1.1eq)	~11	RT, 1min	108
Nanoporous Cu_2O NPs (~45nm)	$CuSO_4$ (~0.1mM), OH^- (3mmol)	AA (200eq)	5000	N/A	104
Cu_2O cubes (800nm) and Cu_2O truncated octahedra (~400 or ~700nm)	$CuSO_4$ (34mM), Citrate (37mM), CO_3^{2-} (60mM)	Glucose (~2eq)	4, 12, 20, or 36	0.5, 4, 8, or 12h; 80°C	74
Cu_2O@Ag polyhedrons (6 different shapes)	$CuSO_4$ (30mM), Citrate (62mM), CO_3^{2-} (100mM)	Glucose (~2eq)	0, 3, 9, 15, 21, or 45	80°C; ~1h	105
Cu@Au@C-NPs (1.4nm by TEM, 3.5nm by SEM, 8.5nm by AFM)	$CuSO_4$ (3mM), $HAuCl_4$ (0.8mM), Carbon black	$NaBH_4$ (~177eq)	19	50°C; Ar (g); ~3h	109
Cu_2O cubes (~120nm) Cu_2O spheres (~1µm), Flower-like Cu_2O (25/800nm)	$CuAcac_2$ (100mM), $CuAc_2$ (100mM), $Cu(OH)_2$ (100mM)	DEG (105eq)	1.8	170°C; 20, 30 or 60min	31
Non-spherical Cu^0-NPs (100-250nm)	$CuSO_4$ (<10mM), OH^- (for pH), SDS (1 to 5eq)	N_2H_4 (20eq)	90	40°C; ~1.5h; pH=10	103
Cu_2O or Cu^0-NPs (time/pH dependent)	$CuSO_4$ (~143mM), SO_4^{2-} or OH^- (for pH)	AA (2eq)	15	pH 3, 5 or 7; Ar(g); 60°C 10min or 4h	110
Cu^0-NPs (~2-10nm)	$CuSO_4$ (0.2mM) EG (none or solvent)	AA (8 or 20eq)	540 or 900	80°C; 1 or 8h	102
Cu_2O nanoboxes (100nm), cubes (200nm), spheres (750nm)	$CuSO_4$ (50mM)	EG (~358, solvent)	0, 270, or 540	180°C (reflux); 30min;	111
Cu^0-NPs (~45nm)	$CuSO_4$ DEG (solvent)	$NaPO_2H_2{\cdot}H_2O$	N/A	140°C; 1h	54

*NVPeq stands for molar equivalents of N-vinylpyrrolidone (i.e. PVP monomers) per Cu^{2+} ion.

It is well-known that the surface energy of the crystallographic facets of Cu_2O crystals grow in the following order: {100} <{111} <{110}[105]. The distribution of the exposed facets will shape the final crystals by the selective growth in certain crystallographic directions[74,105,106]. The {111} facet, which ends with unsaturated Cu, is the easiest to interact with PVP since the {100} plane ends with an oxygen and the {110} plane ends with a saturated Cu[106].

Given the absorption of PVP on the {111} plane, the growth rate in the <111> direction is inhibited. A positive correlation can be found between the ratio of the surface area of {111}

to that of {100} and the amount of PVP. That is, the growth rate ratio (R) in the <100> direction to that of the <111> direction can be tuned by varying the amount of PVP added (**Fig. 5**)[105]. If no PVP is used (R < 0.7), the plane with the lowest energy exposed is the {100} and so, the crystal would adopt a cubic or an eight petal flower shape[74,105]. Upon addition of PVP, the surface energy on the {111} facet would decrease and the {100} facet would be maintained, thus leading to the formation of a truncated cubic morphology [106]. The increased capping effect attained by adding greater amounts of PVP would prevent the atoms from stacking on the {111} facets, helping the growth on the {100} facets and allowing for the formation of truncated octahedral and octahedral forms[74,105]. Other Cu_2O crystals have also been reported in the presence of PVP including nanospheres, star-shaped (low supersaturation), and porous nanocrystals (both {100} and {111} planes present)[74,104].

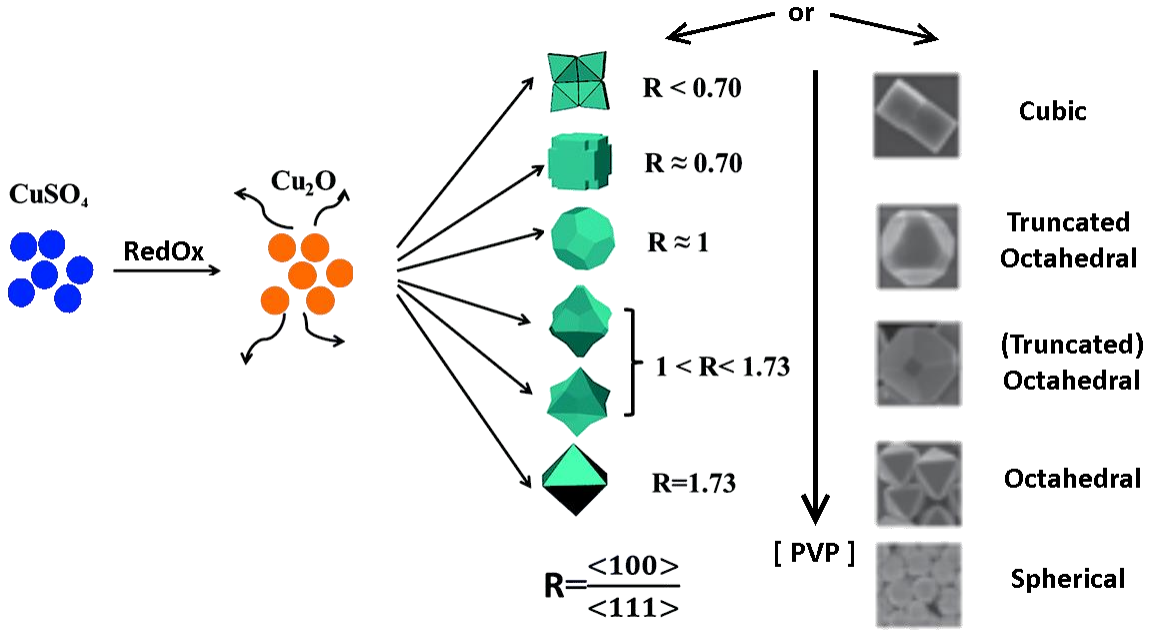

Fig. 5. Schematic of the effect of PVP on the final morphology of the Cu_2O particles (adapt.[74,105]).

Metallic or bimetallic dendrimer complexes are based on dendrimers either conjugated with metal-containing moieties or complexed with metal ions in the dendrimer via surface amines and interior amide. Metal-dendrimer complexes containing Cu, Ag, Au, Pd, Pt, Fe or Ru metals can either undergo further reduction to form metallic NPs or metal displacement may be employed in order to obtain bimetallic NPs[41,112–117]. First synthetized by the research groups of Vögtle[118] and Tomalia[119], dendrimers are tree-like molecules formed by three structural domains: a core, repetitive branch units (n^{th} generation, Gn), and terminal functional groups (end-groups). These three components, as well as size, greatly influence the properties of dendrimers (**Fig. 6**). Frequently, the synthesis of dendrimers may follow a divergent or a convergent approach, originally described by Tomalia *et al.*[120] and Frechet *et al.*[121], respectively (see review by Zeng and Zimmerman[122]). Overall, the exceptional physical and chemical properties of the dendritic architecture hold vast potential when compared to traditional linear polymers[41,101,123].

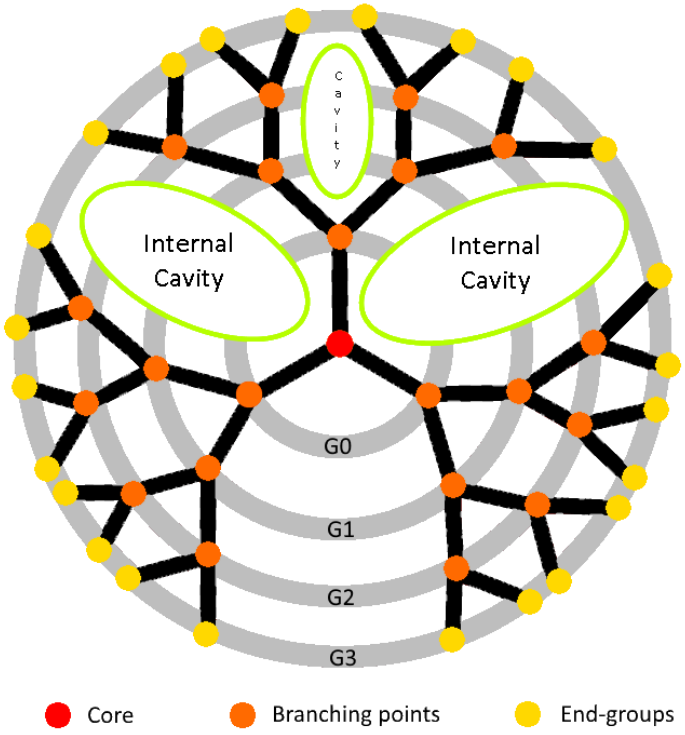

Fig. 6. Schematic representation of the typical architectural and structural features found in dendrimers.

Especially at lower generations, the well-defined molecular structure of dendrimers gives rise to a high monodispersity not found in other polymers having typical broad molecular weight distributions[101,124]. Consequently, dendrimers have a uniform and well-defined size and shape, which is of great interest in biomedical applications given their similarity with biological structures[125]. Combined, these properties influence the ability of dendrimers to cross cell membranes and lessens their early clearance from the body[101,126]. Dendrimer size increases steadily with the generation number (up to tens of nanometers)[127], where lower generations usually have open and amorphous structures and higher generations have a globular conformation capable of incorporating other molecules or metal NPs. A consequence of these features is the passive targeting throughout the body's circulatory system[101,124,126] and in the case of solid tumors, the enhanced permeation and retention effect[124].

The nature of the end groups usually located at the dendrimer surface has a major impact on cell toxicity. Generally, amine-terminated dendrimers display concentration-dependent toxicity and hemolysis, more than anionic or neutral group terminated dendrimers[125,128,129]. It is well-known that the interactions between the positively charged dendrimer surface and the negatively charged cell membrane lead to cell membrane damage and consequent cell lysis[129]. These cytotoxicity issues may be overcome by a complete or partial modification of the end-groups, for instance by PEGylation[126]. Although cell toxicity is also expected to increase with generation size, as seen with the cationic poly(amidoamine) (PAMAM) dendrimer family, other dendrimer families display unpredictable behavior as in the case of the cationic poly(propylene imine) (PPI) dendrimers[128]. Independent of these toxicity issues, dendrimers have been shown to serve as effective delivery systems capable of crossing

biological barriers and targeting specific structures, having sufficient blood circulation time in order for the medical effect to take place. Moreover, further modification of dendrimers may help to overshadow their toxicity issues, as well as add diagnostic or imaging features, and allow for the solubilization of drugs. This possibility is feasible since dendrimers not only have a high payload in their interior but their end-groups can also be easily modified[101,125,126].

Numerous dendrimer families have been described in the literature, grouped according to their structure linkage or chemical moieties: peptide dendrimers, Janus dendrimers, metallodendrimers, glycodendrimers, phosphorus dendrimers, and others[125,127]. PPI and PAMAM dendrimers (**Fig. 7**) are two of the most well-known, with the latter first being described by Tomalia *et al.*[119].

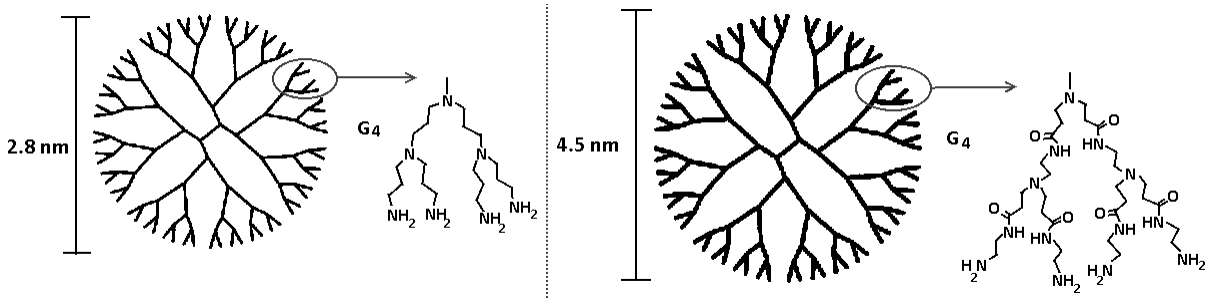

Fig. 7. Comparison between G4 dendrimers: (**left**) PPI and (**right**) PAMAM (adapt.[41]).

Half-generation, COOH-terminated PAMAM dendrimers along with full generation, NH_2-terminated PAMAM dendrimers can directly bind metal ions to their surfaces via coordination to the acid or amine groups (**Fig. 8**)[41,130]. In this work, we are interested in encapsulating Cu ions solely within the interior of commercially available PAMAM dendrimers since such composites hold the desired structural properties of free dendrimers. Moreover, dendrimers functionalized with exterior metal ions cannot be further functionalized. Additionally, compounds prepared from metal ion terminated dendrimers may precipitate from solution because of metal-ion-induced dendrimer crosslinking[41].

Notably, the inner void spaces in dendrimers are large enough to accommodate guests such as metal clusters. In such cases, the NPs within dendrimers are stabilized by the architectural framework. The dendrimer not only acts as a molecular template to synthesize uniform metal NPs but also as a stabilizer to avoid agglomeration. The driving force for guest trapping can be electrostatic interactions, complexation reactions, steric confinement, and distinct types of weaker forces (e.g. van der Waals, hydrogen bonding, hydrophobic forces, etc.)[39,41]. Specifically, the interior of PAMAM dendrimers possess secondary and tertiary amines, both of which are ligands for Cu. The complexation of Cu^{2+} to the interior of NH_2-terminated PAMAM dendrimers can be achieved either by functionalization with non-complexing terminal groups or by the selective protonation of the primary amines where a narrow pH window exists. In the case of hydroxyl-terminated PAMAM dendrimers (**Fig. 8**), the dendrimer negative surface charge would be an impairment for some biological applications including transfection[131]. This however can be easily counteracted through functionalization of the dendrimer surface.

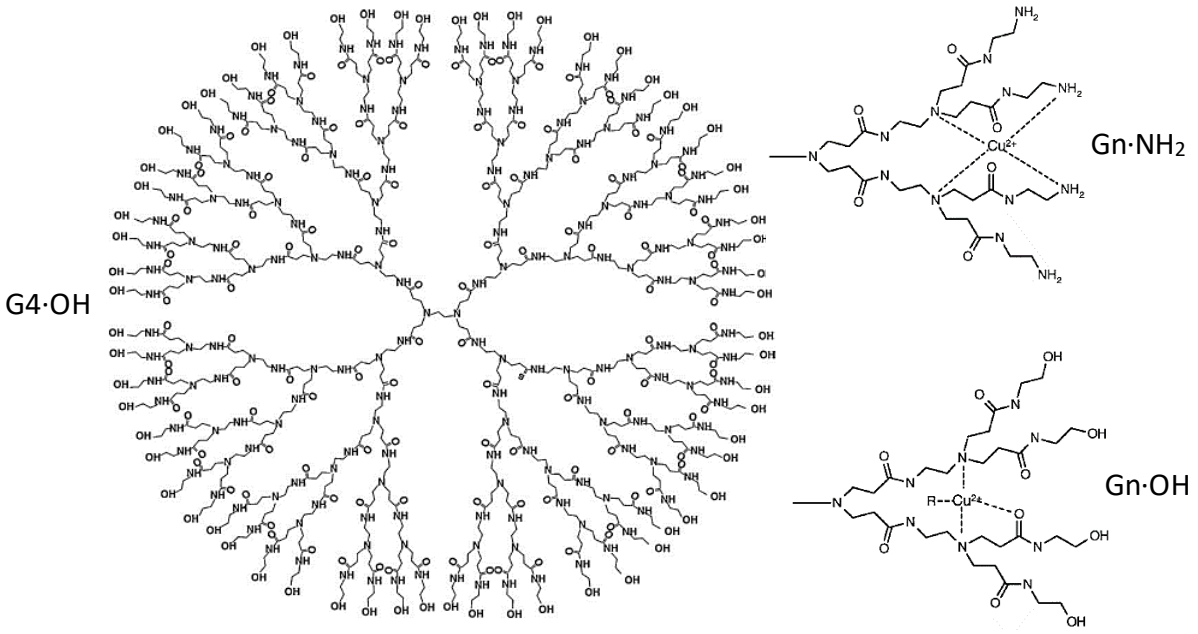

Fig. 8. Illustration of (**Left**) the G4·OH PAMAM chemical structure[131], and (**Right**) the Cu^{2+} ion binding sites in PAMAM Gn·NH_2 and Gn·OH based on empirical data[41].

Several studies have focused on the complexation of Cu^{2+} to the interior of G4·OH PAMAM dendrimers. These dendrimers have 64 hydroxyl surface groups (neutral at pH 7.4), a molecular weight of 14.2kDa (defect-free structure) and a diameter of 4.5nm[41,131]. Since G4·OH has 62 interior tertiary amines and Cu^{2+} is tetravalent, it is inviting to say that each ion is coordinated to about 4 amine groups. However, Electron Paramagnetic Resonance and Electron Nuclear Double Resonance (ENDOR) data indicate that most of the Cu^{2+} ions bind to the 16 outermost pairs of tertiary amines, and space-filling models indicate that the dendrimer structure is not well organized for complexation between the innermost amines and the Cu^{2+} ions. Thus, on average, each ion is coordinated to 2 amines, and the remaining positions are presumably weaker binding ligands such as amide groups or water (**Fig. 8**)[39,41].

1.2.3 Ascorbic acid chemistry

L-ascorbic acid, also known as vitamin C, is a recognized antioxidant in food and biological systems. Therefore, most studies are done for *in vivo* purposes under physiological conditions, at pH=7.4, which is maintained using phosphate buffer or its saline variant (PB and PBS, respectively)[132–136]. AA can be used as a reducing agent in the preparation of CuNPs, but it also has a crucial role to avoid the oxidation of NPs throughout the synthesis and storage process. The capacity to scavenge free radicals and reactive oxygen species (ROS) is what is behind the antioxidant properties of AA[40,102,136]. In order to study the mechanisms of the reaction, heavy isotopes are sometimes used as part of the reaction solvent (e.g. deuterium oxide, D_2O) thus allowing the reaction to be followed by Nuclear Magnetic Resonance (NMR)[132–135]. However, there are physical and chemical differences between normal and heavy water, namely the C-H and O-H bonds are weaker than their "heavy" counterparts[137]. This may introduce unfamiliar interferences in various reactions. For instance, the oxidation of hexoses and pentoses is strongly favored in heavy water[138].

The overall irreversible 2-electron oxidation of reduced AA (*i.e.* H_2A) to dehydroascorbic acid (DHA) can be observed by voltammetry {$H_2A \rightarrow DHA + 2e^- + 2H^+$}, although it frequently acts as a 1-electron reducing agent (**Fig. 9**)[139–141]. The DHA structure is usually represented as the energetically unstable DHA_1, only detected in aprotic solvents, yet the main stable form found in aqueous solutions is the bicyclic hydrated DHA_4[134,142–144].

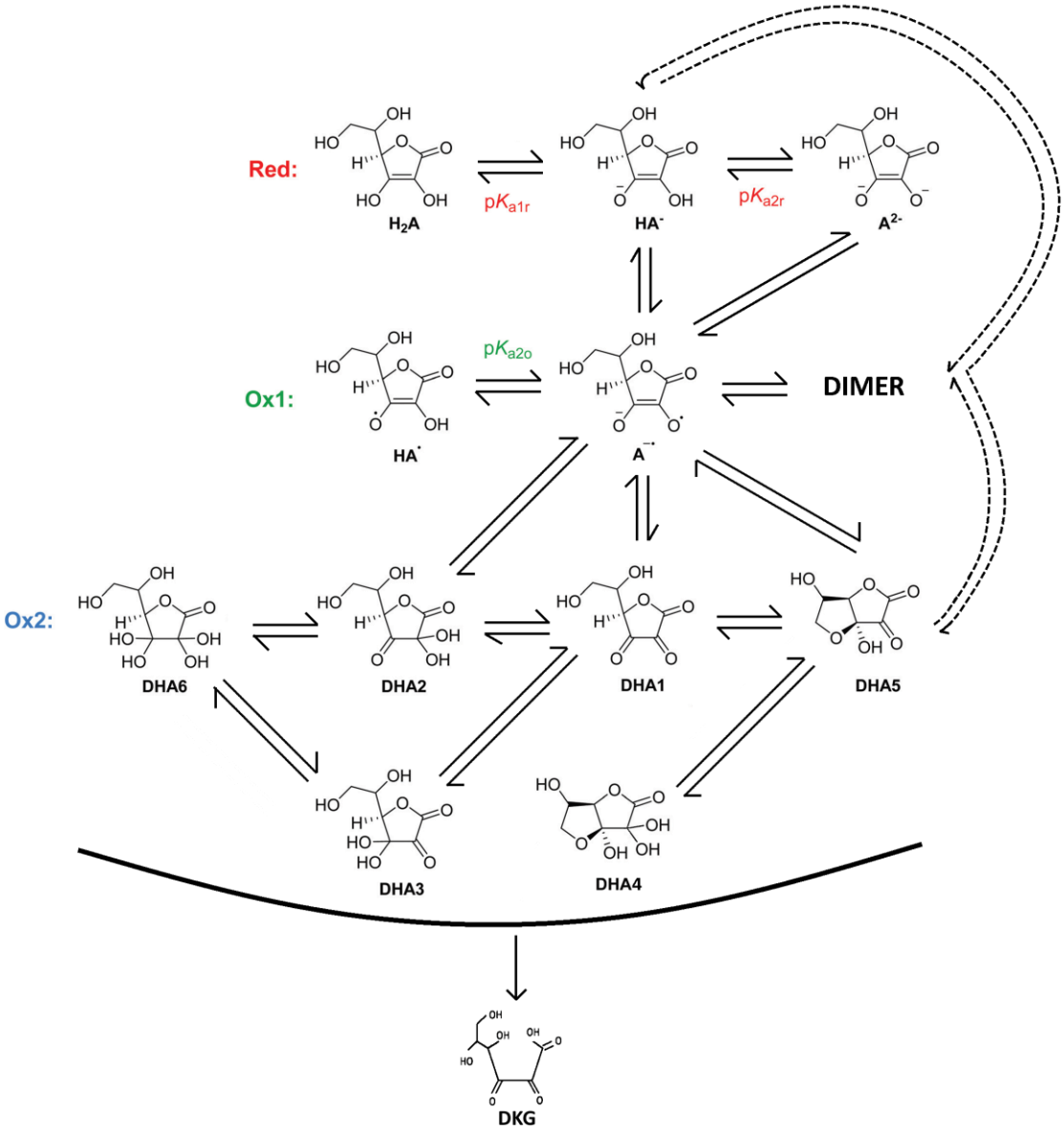

Fig. 9. Electrochemical equilibria and structures of AA and its derivatives in water (adapt.[132,134,145]).

The ascorbate radical, $A^{\bullet-}$, is the product of the 1-electron oxidation of AA. It is able to favorably react with itself or other radicals and is rather unreactive with non-radical molecules. As seen in **Fig. 10A**, if there is no applied potential, the disproportionation of two $A^{\bullet-}$ into AA and DHA is thermodynamically favorable {$2A^{\bullet-} + H^+ \leftrightarrow HA^- + DHA$, ΔG = −11.3kcal/mol at pH=6.4}[145]. This process has been proposed to occur through a dimerization process (**Fig. 10B** and annex **I**)[141,145]. In the presence of protons, two $A^{\bullet-}$ can react with each other yielding a dimer, followed by deprotonation to a fully-regenerated AA (*i.e.* HA^-) and a fully-oxidized DHA_4 avoiding the DHA_1 high-energy intermediate[139–141].

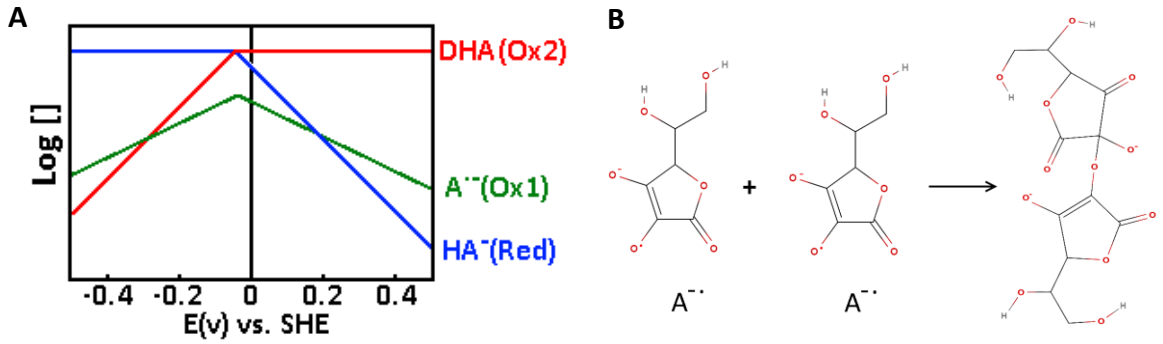

Fig. 10. (**A**) Logarithm of the concentration of AA at different redox stages (at pH=7) varying the applied potential. (**B**) Suggested schematic for the formation of the dimer (See annex I for more details). Adapt.[145].

Both the kinetics and thermodynamics of AA oxidation have been the target of many theoretical[134,136,146,147] and experimental[134,141,148–150] studies. However, a comprehensive understanding of this complex chemistry process has yet to be accomplished. This can be verified by the dispersed range of measured reduction potentials in aqueous media (around +0.06V to +0.4V)[140,144]. As can be seen in **Table 5**, at physiological pH, HA^- is the predominant fully reduced species and $A^{\bullet-}$ is the most stable radical form. This is corroborated with electron paramagnetic resonance results that imply that the unpaired electron of the ascorbate radical is delocalized over the three carbonyl groups[148].

Table 5. Determined pKa values and redox potentials (E°, E vs SHE) of several reactions illustrated in **Fig. 9**.

Condition	Reaction	Parameter	Value	Slope*	Source
$pH < pKa_{2o}$	$HA^\bullet + H^+ + e^- \rightarrow H_2A$	$E°(H_2A/HA^\bullet)$	pH-dependent	−0.059V/pH	*
	$DHA + H^+ + e^- \rightarrow HA^\bullet$	$E°(HA^\bullet/DHA)$	pH-dependent	−0.059V/pH	*
$pH = pKa_{2o}$	$A^{\bullet-} + H^+ \leftrightarrow HA^\bullet$	pKa_{2o}	−0.45	∞ V/pH	Exp. [148]
$pH > pKa_{2o}$	$DHA + e^- \rightarrow A^{\bullet-}$	$E°(A^{\bullet-}/DHA)$ $E°(A^{\bullet-}/DHA_1)$ $E°(A^{\bullet-}/DHA_4)$	-0.174V 0.23V -0.18V	0 V/pH	Exp. [149] Exp. [151] Calc. [145]
$pKa_{2o} < pH < pKa_{1r}$	$A^{\bullet-} + 2H^+ + e^- \rightarrow H_2A$	$E°(H_2A/A^{\bullet-})$	pH-dependent	−0.118V/pH	*
	$HA^\bullet + e^- \rightarrow HA^-$	$E°(HA^-/HA^\bullet)$	0.72V	0 V/pH	Exp. [149]
$pH = pKa_{1r}$	$HA^- + H^+ \leftrightarrow H_2A$	pKa_{1r}	4.04	∞ V/pH	Exp. [149]
$pKa_{1r} < pH < pKa_{2r}$	$A^{\bullet-} + H^+ + e^- \rightarrow HA^-$	$E°(HA^-/A^{\bullet-})$	pH-dependent	−0.059V/pH	*
$pH = pKa_{2r}$	$A^{2-} + H^+ \leftrightarrow HA^-$	pKa_{2r}	11.43	∞ V/pH	Exp. [149]
$pH > pKa_{2r}$	$A^{\bullet-} + e^- \rightarrow A^{2-}$	$E°(A^{2-}/A^{\bullet-})$	0.015V	0 V/pH	Exp.[150]

*from Nernst equation: $E = E° - R \times T/(z \times F) \times Log_e Q$, where T – temperature (Kelvin); z – number of transferred electrons; R – ideal gas constant ($J\,K^{-1}\,mol^{-1}$); F – Faraday constant ($C\,mol^{-1}$); Q – reaction quotient

The hydrolysis of DHA into 2,3-diketo-L-gulonic acid (DKG) is a mostly irreversible process favored by high temperatures and pH values (equilibrium in acidic pH). The degradation of DKG is a complicated process and not fully understood, but it has been reported to yield several by-products in neutral or alkaline pH. Typically, the process involves the loss of oxalic acid and/or carbon dioxide, but the main final product depends on the media conditions[133–135,143,152,153]. For example, under similar conditions (i.e. neutral pH and room temperature) but changing the media from PBS (10% D_2O) to PB (100% D_2O), L-erythrulose or L-threosone were reported to be the major compounds found in a non-oxidative environment, and L-threonic acid (PBS, 10% D_2O) in an oxidative environment[132,133].

1.3 Fluorescent Carbon-based Dots – Properties, Applications, and Synthesis

Typically, the term quantum dots (QDs) is associated with semiconductor nanocrystals having a diameter between 1 and 10nm composed of elements from groups II–VI or groups III–V of the periodic table (**Fig. 11A**). Given the quasi-zero dimensionality of QDs, the mobility of internal electrons is restricted within the nanoscale dimension in all directions, conferring them promising properties specifically as fluorescence labels. These semiconductor QDs (SQDs) have a major drawback related to toxicity concerns associated with their heavy metal composition[154,155]. Although this has been overcome by the substitution of the heavy metals for other elements (e.g. ZnS, ZnSe, ZnO), more recently carbon-based dots (C-Dots) have gained much more attention[154–158]. One of the reasons may be that C-Dots satisfy two significant criteria of relevance for application *in vivo*, namely, they can be excreted by the body and they have low or no cytotoxicity at the concentration needed for cell imaging[154,155].

Throughout the literature, there has been some confusion and inconsistency regarding the terminology used to define C-Dots. Carbon quantum dots (CQD), graphene quantum dots (GQD), carbon nanoclusters, polymer dots, carbon nanodots (CNDs), (fluorescent) carbon NPs and carbon dots (CDs) are some of the most frequently employed terms that every so often get used interchangeably[154,159,160]. Hence, C-Dots and related terminology suggested by Cayuela *et al.* group[154] is used in this work and it serves as a complement to the reader.

C-Dots are based on structures made up mostly of carbon, arranged such that the type of hybridization of the carbon-carbon bonds condition their physicochemical and biological properties. One of the most common examples is graphite, which can be viewed structurally as "stacked graphene layers" held together by van der Waals forces (**Fig. 11B**). Graphene is characterized by sp^2 carbon atoms arranged in a hexagonal honeycomb-like lattice. In turn, graphene layers can stack either with no defined positional relation between atomic positions in one plane and in other planes ("turbostratic" also known as ''rotationally faulted'') or with a 3D order (graphitic, **Fig. 11B**)[157,159,160].

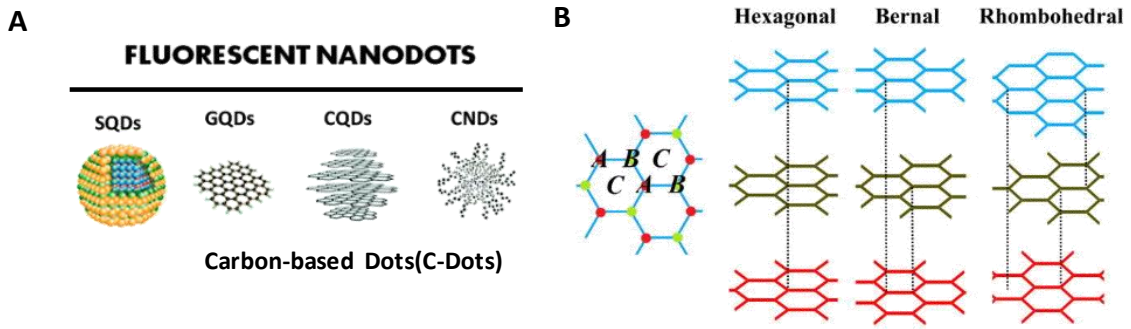

Fig. 11. Different types of (**A**) fluorescent nanodots and (**B**) graphitic arrangements (AAA, ABA and ABC). Adapt.[161].

A few concepts that should be useful to better understand this thesis are listed in **Table 6**. As an important note, in the case of the graphene materials the prefix "nano" should be reserved only if the length or width dimension is at the nanoscale (<100nm), thus disregarding their thickness. Still, a threshold of about 10 layers is significant since it is when the electronic structure of the "stacked graphene layers" becomes indistinguishable from graphite[159,162].

Table 6. Definitions and characteristics of carbon-based materials according to [159,160].

Characteristic Features			Example
Graphenic materials (hexagonal arranged sp^2 carbons) *	Graphene-based Materials	Number of layers	Graphene sheet (monolayer), Few-layer (2-5) graphene (FLG), Multi-layer (2-10) graphene (MLG).
		Shape or structure	Flake, coating, shell, ribbon, fullerene, carbon nanotubes, or film (discontinuous/fragmented layers).
		Chemical composition	Graphene oxide (GO), Reduced graphene oxide (rGO), Doped (e.g. N, S, P)
	3D structures	Graphene layer as the conceptual structural unit	Activated carbons, carbon fibers, and bulk graphite
(tetrahedral arranged sp^3 carbons)			Diamond, amorphous

*may also contain some sp^3 carbon atoms at defect sites or edges.

The key features that can be used to distinguish the different C-Dots are the presence of quantum confinement and crystalline structure. These features are not associated with the amorphous quasi-spherical CNDs but are related to the quasi-spherical CQDs (1-10nm) and the single or few-layer graphene nanosheet GQDs (2-20nm). Remarkably, the latter two C-Dots are typically associated with the different types of precursors used to prepare them. The GQDs are generally synthesized using mainly graphene-based materials, while CQDs make use of either other carbon nanomaterials with crystalline structure or by employing organic molecules.

Moreover, the fundamental part of the QDs can be characterized as (**i**) well-defined spherical nanocrystals of metallic atoms, (**ii**) well-defined nanosheets of sp^2 carbons, (**iii**) crystalline core based on a mixture of sp^2 (main) and sp^3 (minor) carbons, and (**iv**) a mixture of mostly sp^3 carbons in a disordered structural core. These QDs correspond to SQDs, GQDs, CQDs and CNDs, respectively (**Fig. 11**)[154,156,159,160,162,163]. An overview of the general characteristics of the fluorescent dots and the differences between them can be found in **Table 7**.

QDs have unique optical properties that rival standard dyes in many potential applications (e.g. biosensing and bioimaging). They display good fluorescence stability, as well as wide, strong, and tunable spectra. These properties Yet, conventional SQDs are made from metals like cadmium and selenium and are synthesized in organic-phase systems that leads to limitations in terms of high cost and toxicity. Moreover, heavy metals are very toxic even at fairly low concentrations, thus limiting their use in any clinical applications [155,156].

In turn, C-Dots are less expensive, easier to synthesize, have great solubility in water, outstanding biocompatibility with negligible cytotoxicity and good cell permeability, excellent optical properties (e.g. resistance to photobleaching), and possess chemical inertness with the possibility to be easily functionalized[155–158,162–164].

Table 7. Properties of different types of fluorescent nanodots (adapt.[154])

	SQDs	GQDs	CQDs	CNDs
Discovery	1981	2006	2004	
Composition	Inorganic Elements	Carbon Materials	Carbon Materials / Oxygen (5-50%)	
Structure	Crystalline	Mono or few-layer graphene	Predominantly sp^2 core	Amorphous Core
Shape	Spherical	Disk-like	Quasi-spherical	
Quantum Confinement	Yes			No
Solubility	Hydrophobic or hydrophilic	Hydrophilic		
Toxicity	Heavy metals high otherwise low	Low		
Light Absorption	UV-Vis region absorption (broad band)	Prominent ~230nm (π-π*) Shoulder at ~300 (σ-π*) (very broad band)	UV-Vis region (260-350nm) Shift upon passivation (350-550nm) (very broad band)	
Fluorescence Type (Phosphorescence)	Down-conversion (yes)	Up and Down-conversion (yes)	Up and Down-conversion (no)	
PL lifetime	Long (up to ms)	Medium		Short
PL band	Narrow	Broad		Very Broad
PL Scheme	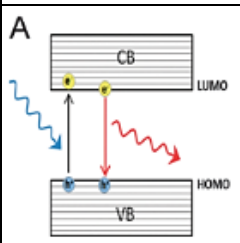	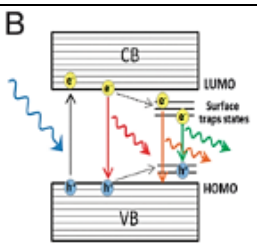		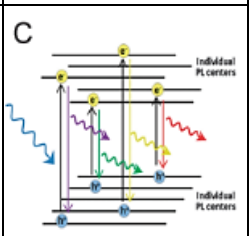
Size Dependent PL	Yes	Yes (not clear)		No
PL Emission	Excitation-independent	Excitation-dependent intensity and wavelength		
Photoblinking	Yes	No		
Common	Opto-electronic properties, large surface area, resistance to photobleaching, good photostability			

GQDs possess a more "molecule-like" character as opposed to colloidal, thus facilitating their functionalization, optoelectronic tunability, and photoluminescence (PL) activity[162]. Additionally, the sp^2 hybridized carbon grid confers these materials with other physical and chemical properties including electrical conductivity and mechanical robustness. "Big" graphene nanosheets have a zero bandgap that limits their usefulness in optoelectronic applications. Their QD counterparts, CQDs, on the other hand have non-zero bandgaps due to the edge site effects that result in the opening of the electronic bandgap. The quantum confinement effect is also crucial to discriminate the quantum material from its corresponding microscale graphene nanosheet and bulk graphite[157,160,163,165]. Thus, C-Dots have been studied for tunable optoelectronic, photonic and electronic devices, energy conversion and storage, catalysis, sensors, bioimaging, among others[155–157,162,166,167].

The relatively strong photoluminescence, in which the emission wavelength depends on the excitation wavelength, is the most important and distinctive property of C-Dots. Great efforts have been made to understand the origin of the PL emission of C-Dots[155,157,168,169] and some hypotheses have been proposed: (**i**) bandgap transitions caused by conjugated π-domains in which the π-connections between the sp^2 "islands" would lead to interisland

quenching and (**ii**) surface-related defective sites (*i.e.* usually any site that has non-perfect sp^2 domains like sp^3 carbons), heteroatoms that result in surface energy traps and carbonyl-related localized electronic states.

Radovic and Bockrath[170] established a structural model for graphene sheets. They proposed that the free zigzag sites are carbene-like with a triplet ground state being most common and the free armchair sites are carbyne-like with a singlet ground state being most common (**Fig. 12**). The defects behave like individual molecules that are incorporated into solid hosts, displaying multicolor emissions from the presence of different defects with associated PL properties. Surface passivation or functionalization stabilizes the defects, enhancing their emissivity and facilitating the radiative recombination of surface-confined electron-hole pairs[156,160,165,171,172].

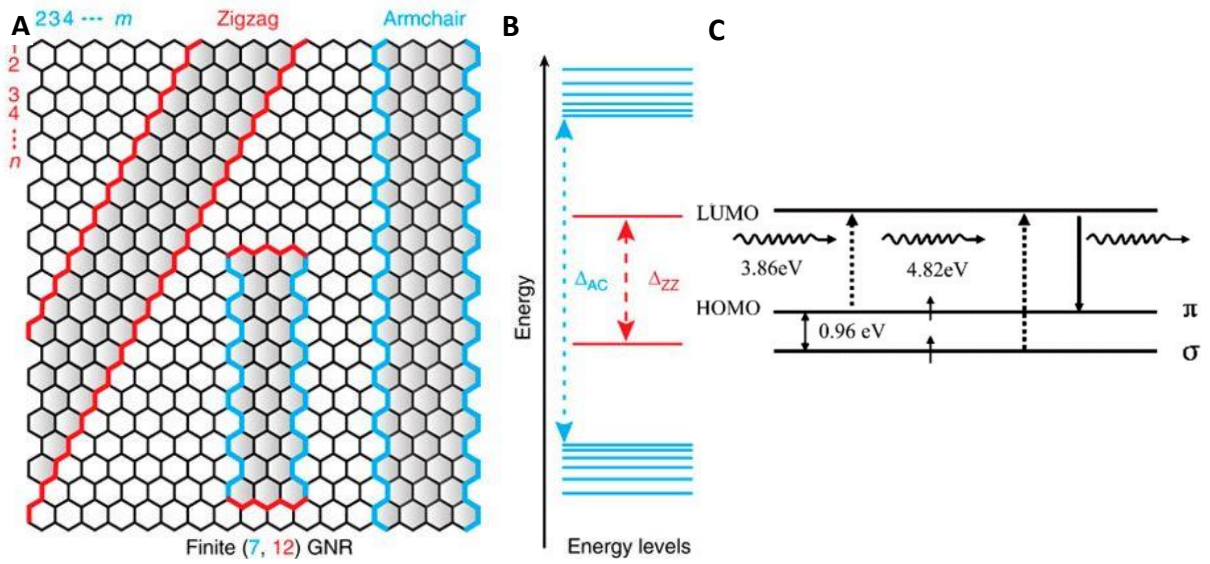

Fig. 12. (**A**) Cutting graphene into nanoribbons with different edge topologies. Indices (m, n) are used to denote the dimensions of a graphene nanoribbon (GNR) along the zigzag (m) and armchair direction (n), respectively. (**B**) Sketch of energy levels for a finite (7, 12) GNR, with Δ_{ZZ} and Δ_{AC} indicating the bulk band gap and the splitting of the localized states. (**C**) Example of the electronic transitions of triple carbenes at zigzag sites observed in the optical spectra. Adapt.[173,174].

The first appearance of C-Dots in the literature was in 2004, where they were accidentally discovered upon the purification of carbon nanotubes fabricated using the arc-discharge method[175]. The synthesis of C-Dots can be divided into two branches[157,162,163,169]. The top-down approaches are based on the fragmentation or exfoliation of carbon sources (such as graphite[176], graphene, GO or rGO[157,174], and carbon black[177]) by chemical[163,177,178], electrochemical[176], and physical[174] procedures. Bottom-up methods on the other hand rely on the controlled growth of GQDs using molecular precursors in a step-by-step chemical reaction, namely via the polymerization and carbonization of some carbon-rich precursors (e.g. organic acids[179–182], carbohydrates[164,183], aromatic compounds[158,184,185]) through thermal or hydrothermal[179,181,182,184–186] microwave-assisted[180,183,187], or sonication treatments[188].

Typically, top-down approaches, particularly chemical oxidation methods, can have the advantage of mass production. Bottom-up approaches on the other hand have the advantage of a more precise control over the size and morphology of the final product (*i.e.* batch-to-

batch reproducibility). A lot of the reported precursors used here however are either expensive or difficult to obtain, or they are unsuitable for large-scale production. These factors combined with the purification, characterization, and ability to control key properties like PL and biocompatibility are important to consider if the C-Dots are intended to be used for clinical or industrial applications[164,184,185].

The hydrothermal method is one of the most common processes used to synthesize C-Dots. It relies on an organic precursor that is heated in water at relatively high temperatures and long reaction times. This method is commonly used as it can lead to a large amount of end-product by consuming cheap materials without the need for toxic solvents. Additionally, the intrinsic properties of the C-Dots may be tailored using this method either by chemical doping with heteroatoms (P, B, N, and S have been reported) or by surface passivation. The use of glucose, AA, and folic acid (FA) as precursors, avoiding the use of harmful chemicals and passivating or doping agents, have proven to favor the formation of biocompatible nanostructures that might be suitable for biomedical applications. FA has the advantage of contributing with nitrogen atoms that enhance the PL properties without any additives or passivation agents (quantum yield up to 94.5%). Moreover, the presence of some precursor moieties not only improves the biocompatibility but also the prospect of intrinsic targeting (e.g. FA-receptors overexpressed in cancer cells)[158,163,164,183]. An example of co-doped C-Dots was made by microwave-assisted thermolysis of N-phosphonomethyl aminodiacetic acid and ethylenediamine. The resultant nitrogen and phosphorus co-doped C-Dots displayed a quantum yield of 17.5%[187].

1.4 Scope and Objectives of this Work

This thesis sought to explore different approaches for the fabrication of Cu-based NPs, and through the optimization of the synthesis conditions, obtain particles that could be suitable for either conductive ink or antiviral applications. For these reasons, a chemical reduction approach using AA as a reducing agent was selected since it is a fairly environmentally friendly and easy method.

Firstly, PVP was used as a stabilizer to prevent the oxidation, aggregation, and growth of the Cu^0-NPs. Preparation of CuNPs in this manner is of interest since small particles of metallic Cu are required to be mixed in with an often polymeric matrix in the process of making a conductive ink. Secondly, Cu Dendrimer Entrapped NPs (Cu-DENPs) were synthesized taking advantage of the functionality, biocompatibility, and protective nature of PAMAM dendrimers without impairing the inherent antiviral properties of Cu. The complexation of Cu^{2+} to the interior of NH_2-terminated PAMAM dendrimers usually requires the selective protonation of the primary amines. Since a narrow pH window exists, this work was focused on the OH-terminated G4 PAMAM dendrimer. Other research groups have reported similar studies where they use different generations, terminal groups and Cu to PAMAM dendrimer ratios [112,123,189]. However, the most significant and distinct difference here lies in the reducing agent used, where $NaBH_4$ was replaced with AA.

Techniques like Ultraviolet-Visible spectroscopy (UV-Vis) and Scanning Electron Microscopy (SEM) coupled with Energy Dispersed X-ray spectroscopy (EDX) were used and found to be of great importance to characterize these particles. Other complementary techniques were also used to characterize the particles, for instance, Fourier-Transform Infrared spectroscopy (FTIR) and Nuclear Magnetic Resonance (NMR).

Preliminary assessment of the *in vitro* cytotoxicity of the prepared particles was done using the 3-(4,5-dimethylthiazol-2-yl)-2,5-diphenyltetrazolium bromide (MTT) cell proliferation assay on the human embryonic kidney cell line, HEK 293T.

2 Materials and Methods

2.1 Materials

Ultrapure water was purified by a Millipore Water Purification System (≥ 18.2 MΩ/cm). A VWR® benchtop meter (SB21 sympHony™) was used for the pH measurements. The chemicals needed for this work are readily available from commercial sources. G4·OH PAMAM, 8.88% (w/w) in water, was acquired from Dendritech®, Inc. (MI, USA). Dimethyl sulfoxide (DMSO, for cell culture) was obtained from PanReac (Portugal). The dialysis membranes were obtained from Spectrum Laboratories (TX, USA).

Petri dishes for cell culture (10cm^2), potassium bromide (KBr, spectroscopy grade) and DMSO (analytical grade) were purchased from Thermo Fisher Scientific (MA, USA). From Gibco™ by Life Technologies, trypsin-ethylenediaminetetraacetic acid (trypsin-EDTA, 0.25%), fetal bovine serum (FBS), antibiotic/antimycotic (100X), and collagen (collagen I rat protein, tail) were acquired.

Copper sulfate ($CuSO_4$) pentahydrate, PVP (40kDa), AA, $NaBH_4$, sodium hydroxide (NaOH), D_2O (99.99%), MTT, sulfuric acid (H_2SO_4, 95-97%), Dulbecco's phosphorus buffer saline (PBS, without calcium), Dulbecco's Modified Eagle's Medium (DMEM), and the centrifugal filter units (Ultra-15 Ultracell Amicon® by Merck Millipore) were bought from Merck (Germany).

A stock $CuSO_4$ solution (1M, 250mg/mL) was made by dissolving the pentahydrate solid in ultrapure water. This solution was used for all the syntheses, diluting when needed to the appropriate concentration with ultrapure water. The required acid (H_2SO_4) and alkaline (NaOH) solutions for the pH-adjusting were also prepared in advance at 3M, 1M and 0.5M.

2.2 Synthesis of Cu-based particles assisted with PVP

2.2.1 Effect of temperature and pH

An aqueous PVP stock solution (111mg/mL) was prepared to be used for all the tested conditions. The amounts of each component are indicated in **Table 8**. The AA solution (176mg/mL) was always prepared fresh, just prior to addition. Different procedures were studied, namely, one in which particle growth would be favored (first PVP and $CuSO_4$ solutions were added, then the AA solution) and another that would favor nucleation (first PVP and AA solutions were added, then the $CuSO_4$ solution).

The synthesis started by adding the first two solutions together at different pH values using up to 1.9mL of acid/alkaline solutions. Ultrapure water was then added to make the solutions up to a final volume. The tested pH values were pH=7, pH=4, and pH~2 (where no pH adjustment was made). Then, the third solution at the same corresponding pH was added into the previously prepared mixture. Each synthesis procedure was tested at two different temperatures, resulting in an overall total of 9 different conditions. Since the reaction would be slower at room temperature (RT) conditions, it was left stirring for a 7-day period. This compared to the 4 hours used for the 60°C temperature condition.

Table 8. Summary of the reagent quantities and concentrations used for the synthesis of Cu-based crystals with PVP as a capping agent (**i**).

	Molecular Weight	Molar Ratio	Initial Concentration	Added Volume	Final Concentration	
	MW (Da)	(mol : Cu^{2+})	C_i (M)	Vol. (ml)	C_f (mM)	c_f (g/L)
$CuSO_4$	249.69	1	0.1	3.375	33.7	8.425
PVP	40 000	~0.01	~0.003	1.350	0.375	15.000
NVPeq	111.14	4	1		135	
Solvent*	N/A			1.900	N/A	
AA	176.12	10	1	3.375	337	59.424

*maximum volume to adjust the pH using H_2SO_4 or NaOH, followed by the addition of ultrapure water to a final synthesis volume of 10mL.

2.2.2 Effect of the PVP and AA to Cu^{2+} ratios

A PVP stock solution (445mg/mL) was used for the set of conditions here. The procedure followed the same steps as described in section **2.2.1**, but it was only done for the growth-favored route and at 60°C. The new values for each component are described in **Table 9**. While the complexation process was running under continuous stirring for 1 hour, a fresh AA solution (264mg/mL) was prepared at either pH=4 or pH=7 and was then diluted with ultrapure water. Each experiment was designed by fixing the PVP ratio (0 to 16 NVPeq) and then, in parallel, varying the AA initial concentration (0.25 to 1.5M).

Table 9. Summary of the reagent quantities and concentrations used for the synthesis of Cu-based crystals with PVP as a capping agent (**ii**).

	Ratio (molar)	C_i (mM)	Vol. (ml)	C_f (mM)	c_f (mg/mL)	Solvent* (mL)
$CuSO_4$	1 eq	1000	0.506	34	8	N/A
PVP Stock	0 NVPeq	0.000	0.000	0.000	0.00	9.432
	4 NVPeq	2.779	0.506	0.375	15.00	8.926
	8 NVPeq	5.557	1.012	0.750	30.01	8.420
	12 NVPeq	8.336	1.519	1.125	45.01	7.913
	16 NVPeq	11.11	2.025	1.500	60.02	7.407
AA Solutions	2.5 AAeq	250	5.062	84.37	14.86	N/A
	5 AAeq	500		168.7	29.72	
	10 AAeq	1000		337.5	59.44	
	15 AAeq	1500		506.2	89.16	

*maximum volume to adjust the pH using H_2SO_4 or NaOH and making up to the final volume of 15mL with ultrapure water.

2.3 Synthesis of Cu-DENPs

2.3.1 Spectrophotometric titration

The Cu^{2+} complexation process was followed by spectrophotometric titration at 605nm as described by Feng *et al.*[123]. First, the pH of a dendrimer solution (10µM) was adjusted to ~5.75 to simulate the synthesis conditions. A 3mL volume of this solution was placed into a cuvette (blank). Then, before each measurement, a 5.0 µL aliquot of an 18.0 mM $CuSO_4$ solution was added to the cuvette while a small magnetic bar stirred the solution vigorously. Different time steps (10, 20, and 40s) were tested to provide sufficient time for Cu^{2+} to bind to the dendrimer before the absorbance measurements were acquired. Moreover, since there

was a low signal-to-noise ratio, other experiments were performed with the aim to improve this condition. This was achieved by doubling the dendrimer concentration, *i.e.* 20µM. The stability of the complex was evaluated by UV-Vis measurements at different time intervals.

2.3.2 $NaBH_4$ reduction chemistry approach

The first synthesis protocol for the Cu-DENPs was based on previously established procedures[39,117,123] where CuNPs are synthesized by complexing Cu^{2+} ions to the interior amine groups of G4·OH PAMAM dendrimers, followed by chemical reduction of the complexed cations using $NaBH_4$ to form the encapsulated Cu^0-DENPs (**Fig. 13** and **Fig. 14A**).

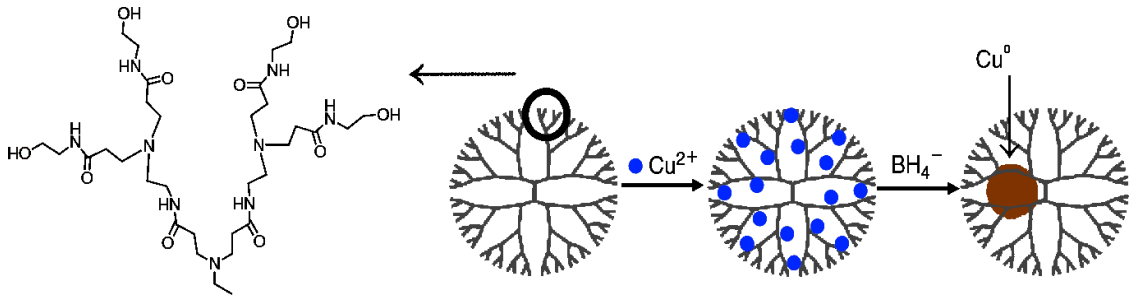

Fig. 13. Dendrimer template-assisted synthesis of Cu-DENPs (adapt.[123]).

Firstly (**Fig. 14A**), 3.569mg of G4·OH PAMAM (0.25µmol) was diluted in 25mL of ultrapure water and the pH was adjusted to ~5.75 after the addition of 40µL of a $CuSO_4$ solution (0.10M; 16 molar ratio). Since the pH of the dendrimer, and the Cu^{2+} and PAMAM solution was found to be in the range of 6.0-6.5, and the complexation of the Cu^{2+} ions is inhibited at lower pH values (the amines suffer protonation at pH<3.5)[41], a synthesis procedure was performed without this pH adjustment step (**Fig. 14B**). The solution was then left to stir for 15min to allow the complexation to be completed. In order to improve the results, a complexation time of 1h was used in future attempts, as seen in the work of *Nemanashi et al.*[112]. Next, we proceeded with the reduction of the Cu^{2+} ions by the dropwise addition of 800µL of a freshly prepared $NaBH_4$ solution (0.10M, 20 molar ratio to Cu^{2+}) and stirred for 45min. A UV-Vis spectrum was done before and after adjusting the pH to 8, and the stability over time was evaluated. Only in the very first study was this last pH adjustment performed (as recommended), since the measured pH was already alkaline (pH>9), thus already ensuring the stability of the NPs that would otherwise be lost by the addition of acid. Additionally, the process was done in air and later under inert conditions in order to prevent the oxidation of the CuNPs[7].

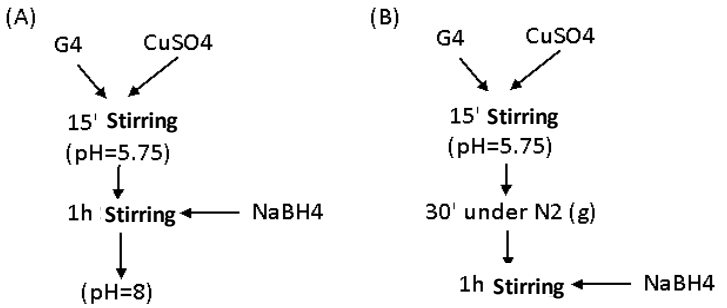

Fig. 14. Schematic procedure for the synthesis of Cu-DENPs using $NaBH_4$ as a reducing agent: (**A**) as in the literature and (**B**) modified to improve the stability.

2.3.3 AA reduction chemistry approach

Since previous attempts to reproduce the established procedures from the literature[39,117,123] were unsuccessful, the synthesis protocol was further adapted. In an initial test, AA was used as a reducing agent for the Cu^{2+} ions instead of $NaBH_4$ as described in **Fig. 15A**.

Firstly, 100mL of a 25µM PAMAM solution was transferred into a 250mL round-bottom flask. Then, 40µL of a 1M $CuSO_4$ solution was added dropwise to the PAMAM solution (16 molar ratio) under magnetic stirring, and the pH was adjusted to 7. The solution then underwent a 30min degassing procedure using N_2[7,39,110,117,123].

Next, the pH of an AA solution (0.8M, 5ml) was adjusted to be the same as that of the solution in the round-bottom flask. Finally, the AA solution was added dropwise and under magnetic agitation to the complex solution and was left to react for 4h at 60°C. After cooling to RT, the solution was purified using a centrifugal filtration unit (see section **2.4**). The adjustment of the pH of the AA solution was necessary since the reaction would otherwise not have occurred. Failure of the reaction to occur would be confirmed by the indigo color of the solution being lost. This can be explained by the protonation of the interior amines caused by the drastic pH drop introduced by the acidity of AA.

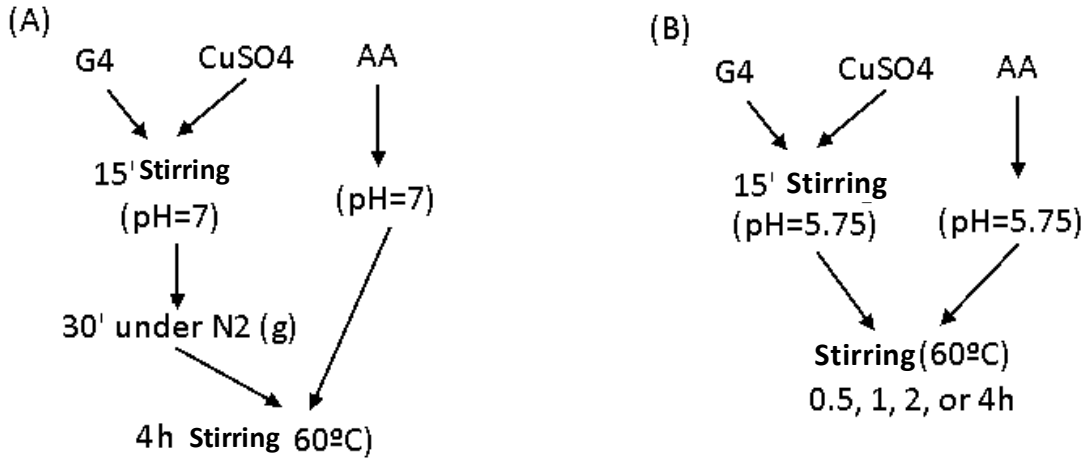

Fig. 15. Schematic of the procedure for the synthesis of Cu-DENPs using AA as a reducing agent: (**A**) initial test, and (**B**) optimization process.

After confirming that the procedure worked, an attempt was made to simplify the experimental synthesis process (**Fig. 15B**). Henceforth, the pH of the complex was maintained at the original 5.75 instead of increasing it to 7 as done by Liu *et al.*[110]. Consequently, the AA solution was also adjusted to pH=5.75. Also, since the AA would help prevent the oxidation of the CuNPs, the degasification step was disregarded. In addition, the ratio of the AA to Cu was decreased from 100:1 to 10:1 to reduce the cost of reagents. Given these adjustments made in this new procedure, the effect of reaction time was also tested (30min, 1h, 2h, and 4h).

2.4 Storage and Purification

All the working and final solutions were stored at 4°C and protected from light. To obtain the solid-phase from the PVP route, the samples were centrifuged at 4000xg for 10-15min (Sigma, model 3-30K). The liquid was then removed, the precipitate was washed with ultrapure water, and then lyophilized. The purification and concentration process of the liquid phase from the PAMAM route was done by a filter system in conjunction with an applied centrifugal force in centrifugal filter units (MWCO of either 3KDa or 10kDa), as specified by the supplier instructions. The samples sent for HR-TEM and XPS analysis were previously centrifuged for 4h at 20 000x*g* and 1mL was carefully withdrawn from the top of the solution.

A freeze-dry process was required when utilizing some techniques for sample characterization, namely when solid state samples were required or when there was the need to change the solvent (e.g. with D_2O). This was achieved by pipetting aliquots with known volumes to previously weighed out empty Eppendorfs and then freezing the solution at -20°C. The samples were then placed in the lyophilizer (Labconco FreeZone® 4.5 Liter Freeze Dry Systmes) for 3 days to promote the sublimation of the water. Doing as indicated allowed us to estimate the solution concentration (mass/volume) after the process was completed.

2.5 Spectroscopic and Spectrometric characterization

2.5.1 Ultraviolet-Visible spectroscopy

All UV-Vis spectra were obtained using a quartz cuvette and the absorbance measured using a Perkin Elmer Lambda 25 spectrophotometer. The acquisitions were done in the Perkin Elmer UV WinLab Software (version 5.2.0.0646). Most measurements were done with the as-prepared solutions with no regard to concentration, unless specifically indicated. Ultrapure water was used as a solvent for the cases where sample dissolving or diluting was needed.

2.5.2 Nuclear Magnetic Resonance spectroscopy

A Bruker NMR Spectrometer (UltraShield™ 400MHz Plus ULTRA LONG HOLD, Avance II+) was used for the ^1H NMR characterization with the probe temperature at 25°C. All lyophilized samples were dissolved in D_2O. The chemical shifts (δ) were calibrated based on the residual solvent peak and presented in ppm units. The data acquisition and treatment were done with the TOPSPIN Software (version 3.5.7).

2.5.3 Photoluminescence - Fluorescence spectroscopy

All the PL spectra were obtained using a quartz cuvette that was placed into a Perkin Elmer LS 55 Fluorescence Spectrometer (Perkin Elmer FL WinLab Software, version 4.00.03). Most measurements were done with the as-prepared solutions with no regard to concentration, unless indicated. Ultrapure water was used as a solvent for the cases where sample dissolving or diluting was needed.

2.5.4 Fourier-Transform Infrared Spectroscopy

The FTIR spectra were obtain using KBr pellets or with an ATR accessory on a Perkin Elmer Spectrum Two Spectrometer. The spectra were acquired with the Spectrum Software at the $4cm^{-1}$ resolution with 32 scans and along the 4000 to 400 cm^{-1} range.

2.5.5 X-ray Photoelectron Spectroscopy

X-ray photoelectron spectra (XPS) were obtained as a service from the Central Service to Support Research Building (SCAI) at the University of Málaga (Spain) using a Physical Electronics PHI 5700 spectrometer with a non-monochromatic AlK_{α} radiation (53W, 15kV, hv=29.35eV) as the excitation source. Spectra were recorded at 45° take-off angles by a concentric hemispherical analyzer operating in the constant pass energy mode at 25.9eV, using a 200mm diameter analysis area. Under these conditions the Au $4f_{7/2}$ line was recorded with 1.16eV full width at half maximum at a binding energy of 84.0eV. The spectrometer energy scale was calibrated using Cu $2p_{3/2}$, Ag $3d_{5/2}$ and Au $4f_{7/2}$ photoelectron lines at 932.7, 368.3 and 84.0eV, respectively.

Charge referencing was done against adventitious carbon (C 1s 284.8eV). Powdered solids were mounted onto a sample holder without adhesive tape and were kept overnight under high vacuum in the preparation chamber before they were transferred to the analysis chamber of the spectrometer. Each region was scanned with several sweeps until a good signal to noise ratio was observed. The pressure in the analysis chamber was maintained lower than 10^{-9} Torr. A PHI ACCESS ESCA-V6.0 F software was used for acquisition and data analysis. A Shirley-type background was subtracted from the signals. Recorded spectra were always fitted using Gauss–Lorentz curves to determine more accurately the binding energy of the different element core levels. The accuracy of the binding energy values was within 0.8eV for the survey and 0.125eV for the other measurements.

2.6 Electron Microscopy characterization

2.6.1 Scanning Electronic Microscopy

The morphological characterization of the Cu-based NPs was performed on a Bench Scanning Electron Microscope (SEM Phenom - Pro X) using the ProSuite image acquisition, processing, and analysis Software. The images were taken at different voltages (5, 10, and 15kV) depending on the sample stability under the beam, but the EDX analysis was always done at the recommended 15kV.

2.6.2 Transmission Electronic Microscopy

The morphology of the C-Dots was analyzed under a FEI Talos F200X high-resolution transmission electron microscope (HR-TEM). The analysis was done as a service from the Central Service to Support Research Building (SCAI) at the University of Málaga (Spain).

2.7 Dynamic Light Scattering and Electrophoretic Light Scattering

The Zetasizer Nano ZS equipment (Malvern Instruments Ltd., UK) was used for the Dynamic Light Scattering (DLS) and Electrophoretic Light Scattering (ELS) characterization. The studies were performed at 25°C in standard polystyrene cuvettes for the DLS measurements and in folded capillary polystyrene cuvettes for ELS measurements. Sample analysis was performed in triplicate. Most measurements were done with the as-prepared solutions. Ultrapure water was used as a solvent for the cases where dissolving or diluting was needed. The Zetasizer Software (version 7.12) was used for data analysis.

2.8 Assessment of the cell metabolic activity

2.8.1 Cell culture

The cell studies were done using the human embryonic kidney cell line (HEK 293T; ATCC® CRL-3216™). The cells were cultured with complete medium on petri dishes. The complete medium contained 89% DMEM, 1% antibiotic/antimycotic and 10% FBS. The cells were grown in an incubator at 37°C with 5% atmospheric CO_2 until attaining a sufficient number of cells necessary for the cell viability assays, without getting to 100% confluence. As such, sub-cultures were performed every 2-4 days to maintain the cells. For this, the culture dishes were first washed with 2mL PBS to remove the calcium from the media that is known to inhibit the enzymatic activity of trypsin. To promote the detachment process, 1mL trypsin was added to the culture dishes and then they were placed into the incubator for ~10min. Cell detachment was finally halted by the further addition of 2mL complete medium.

2.8.2 MTT assay

Three lyophilized samples were selected to be preliminarily evaluated for their cytotoxicity properties. This study relies on the MTT reduction assay[190,191]. This test provides an indirect measurement of the cellular metabolic activity, which transforms the MTT dye into the purple colored formazan. This reaction is reliant on of the NAD(P)H-dependent cellular oxidoreductase enzymes from the active cells. Thus, a greater number of cells will be translated to an increased signal. This way a correlation can be made between the cell viability and the absorbance measured in a microplate reader (Victor^3 1420, by Perkin Elmer).

Briefly, the assay started by growing HEK 293T cells in a 96-well plate using 5 000 cells/well. This was done after pretreatment of each well with collagen (50µg/mL) dissolved in 20mM acetic acid to improve the cell adherence. On the next day, the cells were exposed to the different compounds. Here, a 10% test sample volume was added to a 90% volume of fresh media, with the final sample concentrations in each well lying in the range of 0 to 500µg/mL. After 48h sample exposure, the culture medium was replaced for 20% (v/v) MTT in completed culture medium and incubated for 4h. Finally, the media was removed, and the formazan crystals were dissolved in 200µL DMSO before reading the absorbance at λ=550nm.

The data were represented as the average of the normalized values as shown in **Eq.1**, where Abs, Abs_{blank} and Abs_0 are respectively the measured absorbance of each sample, of the blank (solution containing only DMSO), and at concentration zero (sample from the cells exposed only to the solvent).

$$Metabolic\ activity\ (\%) = \frac{Abs - Abs_{blank}}{Abs_{[zero]}} \times 100 \qquad (\boldsymbol{Eq.1})$$

2.9 Data treatment

Aside from the software already provided with the analytic equipment, other third-party programs were used to treat, process and represent the data. A list of the software used is summarized in **Table 10**.

Table 10. Summary of the used third-party software

Software	Usage	Data
Microsoft Excel 365, Version 1812	Processing, minor statistics and calculations, spectral fitting and alignment, and plots	UV-Vis, PL, FTIR, DLS
Spectragryph[192], Version 1.2.9	Processing, spectral smoothing, and Excitation Emission Matrix (EEM) counter plots	PL, UV-Vis, FTIR
Fiji [193], "Fiji is just ImageJ [194,195]", with DiameterJ [196] plugin	Metrics: particles size and fringe spacing measurements	TEM, SEM

3 Results and Discussion

3.1 Synthesis and characterization of PVP assisted particles

During a pre-optimization stage, the stability of the individual components and mixtures of pairs of reagents was evaluated twice a week for a 3 week period. The absorption spectra of the freshly prepared solutions and the same solutions at the end of the third week are shown in **Fig. 16**. The $CuSO_4$ blue solution presents its characteristic broad absorption band at 810nm, correspondent to the d-d transitions for Cu^{2+} in a tetragonal distortion of the octahedral ligand field, in this case, the hexaaquacopper (II) ion ($[Cu(H_2O)_6]^{2+}$)[39].

As can be seen in **Fig. 16**, the PVP-containing solutions did show a small band around 320nm that most likely corresponds to the presence of some PVP monomers having the carbonyl (n-π*) transition. Moreover, for the samples prepared only in water, the intensity of this band decreases over time. Possibly, this means that the amide bond hydrolyzes. When adding the copper ions to the PVP solution, a new absorption band was detected in the 400-500nm region suggesting the formation of a complex.

The appearance of the absorption band at 350nm in the fresh AA solution (AA 0W in **Fig. 16**) comes from the various products of the oxidative degradation of DHA (e.g. L-threosone)[132,197]. As expected, after 3 weeks the AA solution shows a considerable redshift as a result of the rising concentration of further oxidation by-products. Because of this fact, all AA solutions were prepared fresh prior to use and were protected from the light.

When mixing the $CuSO_4$ and AA solutions together, a distinct band appears at 680-700nm that is maintained at a lower band intensity after 3 weeks (AA+Cu^{2+} in **Fig. 16**). This band is likely to be the result of a change in the metal oxidation state or the coordinated ligands. However, this wavelength has not been found in the literature associated with Cu complexes. Theoretically, some clusters in solution could also be responsible for the absorption since the formation of Cu_2O is anticipated as a product of the redox reaction. Also, an orange deposit was formed after some time.

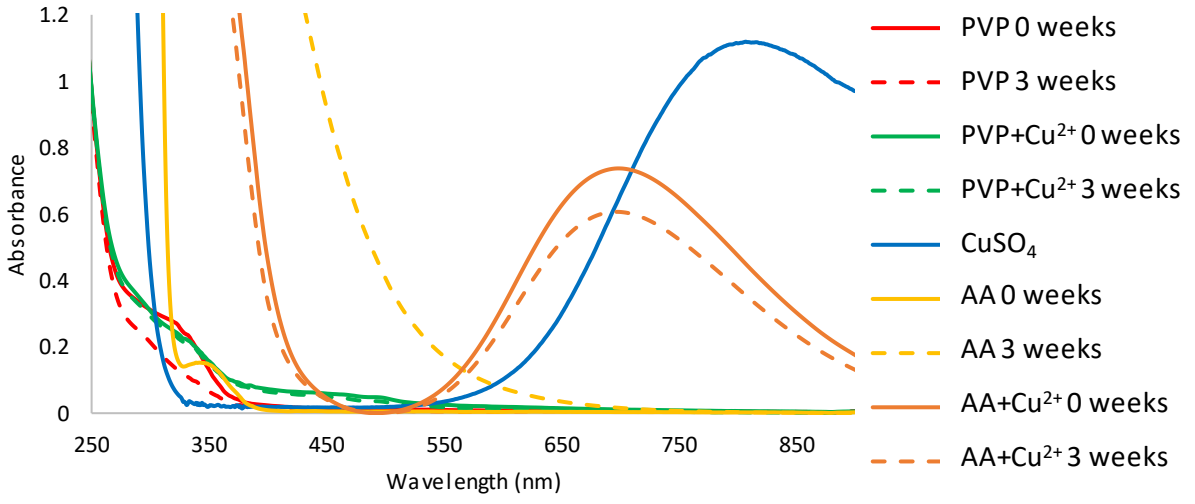

Fig. 16 Stability of the control solutions, prepared fresh (——) and after 3 weeks (- - -). (**Red**) PVP solution; (**Green**) Copper-PVP complex solution; (**Yellow**) AA solution; (**Orange**) $CuSO_4$ and AA solution; (**Blue**) $CuSO_4$ solution.

3.1.1 Influence of pH and temperature on the formation of the Cu-based particles

The evaluated pH and temperature effect on the formation of Cu crystals is outlined in **Table 11**. Using the color of the powder and the information obtained by the semi-quantitative EDX data, an estimated composition of the particles was made. This should only be considered as a preliminary analysis since other more reliable techniques must be used to give more accurate values (e.g. XPS or flame atomic absorption). The copper to oxygen ratio can give an indication of the oxidation state of the metal. This prediction was done assuming that most of the unused PVP, AA and AA by-products stayed in solution. Thus, all carbon and nitrogen present, as well the stoichiometric amount of oxygen, should belong to the PVP capping the Cu crystals.

The availability of PVP complexing groups plays an important role in the control of the shape of the Cu particles since they have a selective interaction with the {111} facets, as reported in the literature.[74] The pH of the system may disrupt the ability of the PVP to complex with Cu since the PVP amides will have more affinity for the protons than for the Cu. In addition, the equilibria of the redox reactions and side reactions of AA will also be influenced by the pH.

It was noticed that by decreasing the acidity of the synthesis solutions up to a neutral pH, the particle size decreased (**Table 11**). For instance, for the globular copper crystals, the size dropped by roughly half when changing the pH of 2 to a pH of 4. The size halved again when a pH change from 4 to 7 was tested. Since the amide groups of the PVP are protonated at low pH values, as we decreased the proton concentration, more and more groups became available to interact with the Cu, leading to a better control of the size of the crystals. This may be evidenced at higher pH values by smaller and more monodispersed particles. The influence of the PVP on the shape of the crystals is clearly more relevant at a pH of 4 at 60°C where the formation of cut faces is observed (see **Table 11**). At a pH of 7, there is a higher ratio of free complexing sites for Cu^{2+}, enhancing the formation of nuclei and thus preventing the degree of growth seen for the particles at lower pH values.

On the other hand, temperature will constrain Cu particle synthesis driving it to be more kinetically controlled. This means that at a lower temperature, the reaction will be slower, pushing the formation of more thermodynamically stable compounds such as CuO instead of the more attractive Cu_2O and Cu^0. An increase in temperature will also favor bigger and more monodispersed particles at the cost of smaller particles, leading to the so-called Ostwald ripening effect. Under RT conditions, where synthesis reactions were left under constant stirring for one week, the existence of carbon dioxide either as a by-product of AA oxidation or from the atmosphere (reaction vessels were left unsealed) may have led to the formation of carbonate ions. More specifically, the formation of Cu carbonate impurities ($Cu_3\{CO_3\}_2\{OH\}_2$ or $Cu_2CO_3\{OH\}_2$) may explain the extra carbon content and the unexpected blue or green dust of the synthesized Cu-based particles, as seen in **Table 11**. The green color of the powders in particular is mostly associated with Cu chloride or Cu acetate. Sulfuric acid was knowingly used

instead of hydrochloric acid to avoid the formation of Cu chloride, even if only as small impurities. Also, chloride ions are known to be reactive with metals.

As for the reactions prepared using a pH of 2 and a temperature of 60°C, the initial deposit was reddish in color. But after drying, a green layer formed on the surface due to the exposure to air. It is assumed that Cu^0 was originally formed and subsequently oxidized. The green color would again be associated with the carbonate.

The conditions that may be considered as more interesting to continue working with correspond to the synthesis reactions performed at 60°C and at either pH 4 or pH 7 since they yielded Cu particles with a more preferable oxidation state. Moreover, the polyhedral and spherical crystal shapes are more appealing to work with relative to the needle-shaped crystals that may have a negative effect on cells.

The order of addition of the PVP, AA and $CuSO_4$ components was investigated, namely the growth-favoring versus the nucleation-favoring experimental procedures. However, no significant difference was observed between the two approaches used. The growth-favoring approach was chosen for the next experiment because it seemed that the nucleation-favoring approach led to crystal aggregation at 60°C and pH=4.

Table 11. SEM images of the synthesized particles using the growth-favoring approach, after centrifugation and lyophilization to remove the liquid phase. In each case, the image color is a post-modification of the original picture and mimics the powder sample.

	RT	Observations*	60°C	Observations*
pH=7	N/A		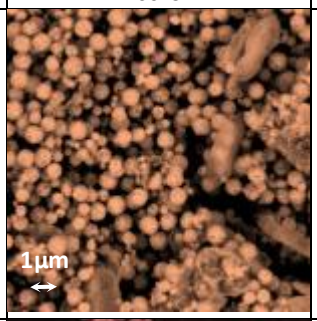	Spheres 59%Cu 32%O 8%C 1%N Cu_2O
pH=4	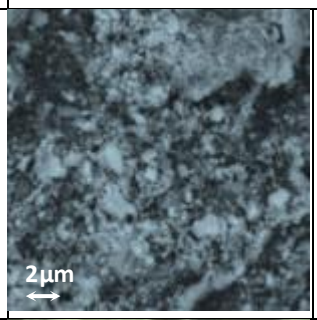	Amorphous 17%Cu 70%O 12%C 1%N Mostly CuO	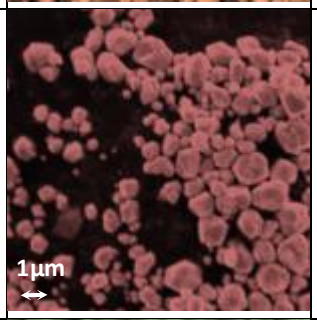	Polyhedral 93% Cu 4%O 3%C 0%N Cu^0
pH=2	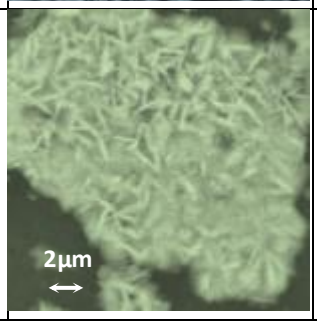	Needles& Amorphous 58%Cu 27%O 14%C 1%N Mostly CuO	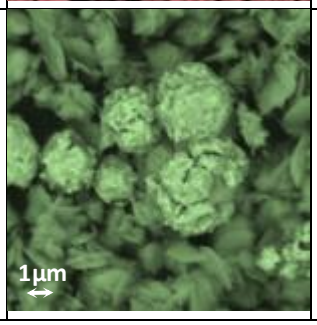	Globular 56%Cu 39%O 5%C 0%N Cu^0 / CuO Mixture Disks 30%Cu 63%O 6%C 1%N Mostly CuO

*The observations state the shape, molar composition determined by EDX and proposed Cu species, respectively.

3.1.2 Effect of the concentration of PVP and AA on the formation of the Cu-based particles

The study of the effect of the concentration of the starting materials was done by fixing the Cu^{2+} molar quantity to one and varying the molar quantities of AA and PVP. The mol equivalents of the PVP monomer, NVP, (henceforth referred to as NVPeq) was used to give a more direct physical meaning to the ratios used. For instance, 4 NVPeq means that for each copper ion there should be four amide groups available for complexation. A similar reasoning was applied to the AA mol equivalents (AAeq), where for each Cu^{2+} there was a corresponding amount of AA molecules capable of reducing the metal.

The SEM images in **Table 12** show that all the prepared Cu-based particles had a spherical shape and a seemingly good size distribution. While no statistical size measurements were done at this stage, some individual measurements indicated an average particle size of about 390nm. EDX data suggests that all the tested samples prepared using a pH of 7 were mostly Cu_2O, with the atomic ratio of Cu and oxygen being approximately 2:1. Since Cu_2O is typically reported as being red, the orange hue of the precipitate may be explained by impurities in the main lattice.

The effect of the addition of AA on the Cu-based particle formation (2 left columns of **Table 12**) may be considered a balance between two factors: (**i**) an increase in concentration of the reducing agent that reduces the particle size and (**ii**) the availability of the reducing agent that is able to reduce more ions thus increasing the particle size. After reaching the reaction stoichiometry, the addition of more reducing agent should only decrease the overall particle size by favoring the nucleation process. In the case of the NVPeq being fixed to 4:1, there is a small decrease in size from the lowest to the next sample, but then the particles more or less maintain their size up to 15 AAeq.

In contrast, if the AAeq is fixed at 10:1 (2 right columns of **Table 12**), the Cu particles maintain their apparent size when adding more PVP at lower NVPeq. They then increase slightly in size before noticeably decreasing in size in the last sample. This behavior is counterintuitive since the more capping agent that is added, the more the particles should be "protected" and so it is difficult to understand what is contributing to the particle growth.

UV-Vis analysis of the liquid-phase solutions (*i.e.* after centrifugation) from the synthesis performed at pH=7 is presented in **Fig. 17.** A band found around 690nm is more prominent at lower AAeq, whereas at higher equivalents the band is almost inexistent (**Fig. 17A**). Assuming that the band is from the Cu ions, this means that a 10 AAeq is needed to ensure that all the Cu is reduced to yield particles. Besides, the shift from 810nm to 690nm may be a result of a ligand replacement with hydroxyl groups. In **Fig. 17B**, the increase in PVP content in the reaction mixture has an increasing effect on the absorption intensity. Here, it is more likely that this band corresponds to particles in suspension. This is the case, since it appears that there is a redshift accompanied by an increase in absorption intensity. These statements suggest that PVP favors the formation of bigger particles.

Table 12 Study of the effect of the AAeq and NVPeq in the formation of the Cu-based particles at pH=7, after centrifugation and lyophilization to remove the liquid phase. Notes: The condition 4NVPeq + 10AAeq was repeated twice. In each case, the image color is a post-modification of the original image and mimics the real powder sample.

10 000x Amplification	20 000x Amplification		10 000x Amplification
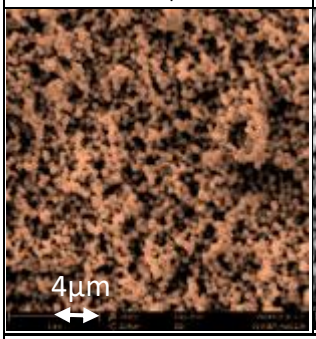	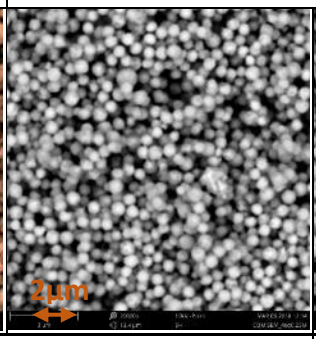	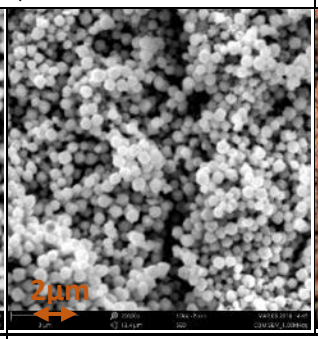	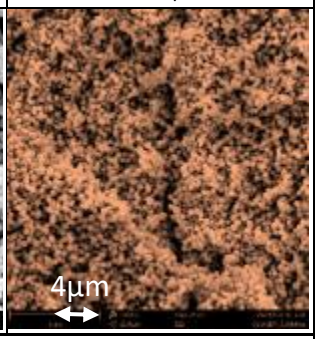
4NVPeq + 2.5AAeq		4NVPeq + 10AAeq	
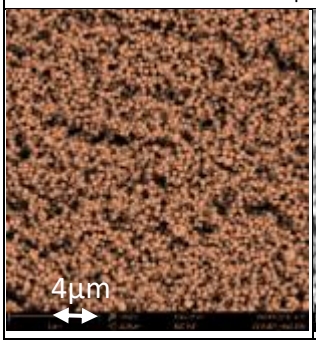	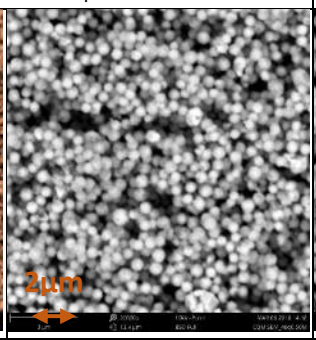	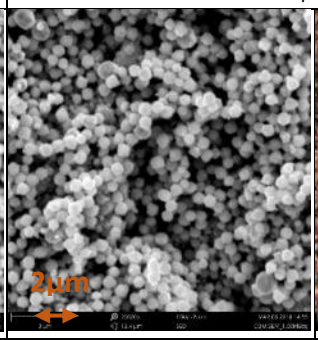	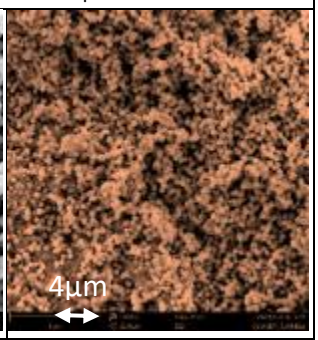
4NVPeq + 5AAeq		8NVPeq + 10AAeq	
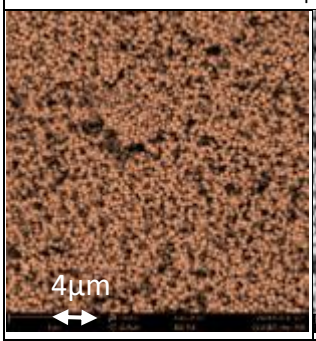	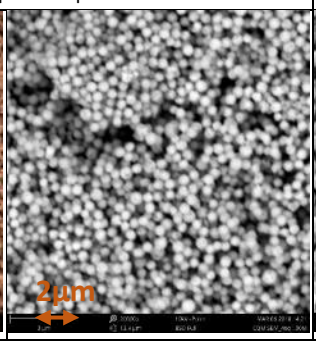	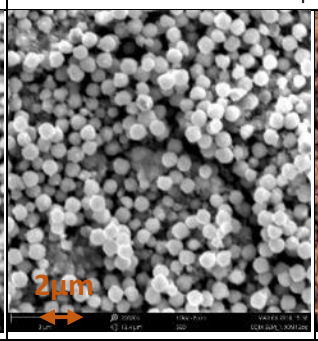	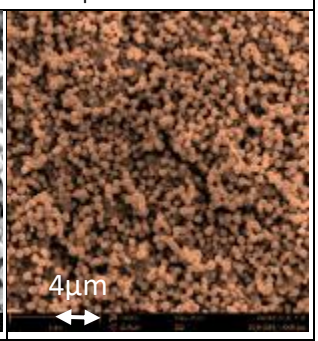
4NVPeq + 10 AAeq		12NVPeq + 10AAeq	
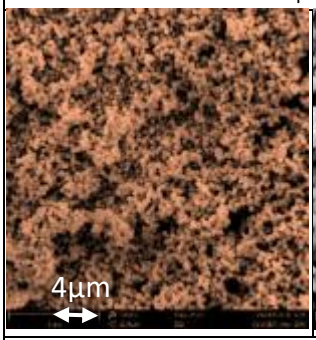	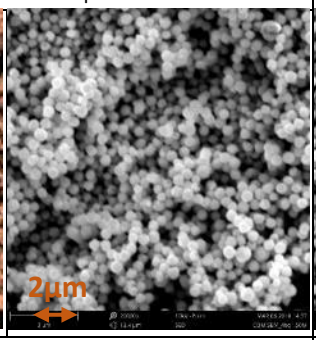	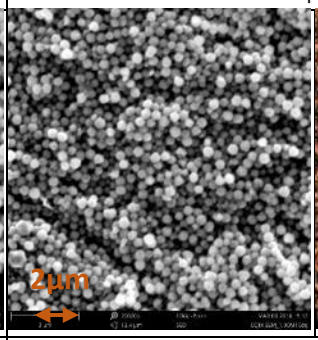	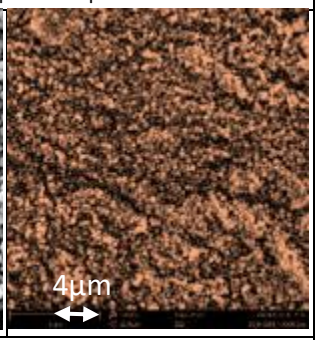
4NVPeq +15AAeq		16NVPeq + 10AAeq	

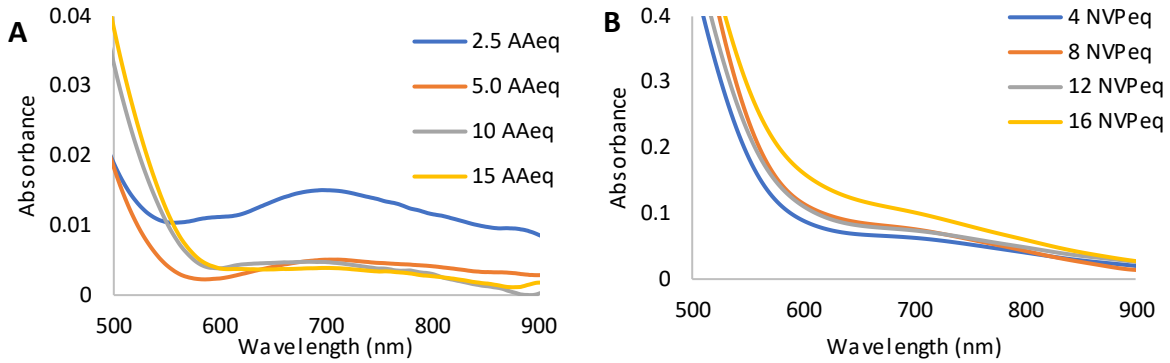

Fig. 17. UV-Vis spectra of the liquid-phase solutions of the synthesis performed at pH=7 with **(A)** fixed 4 NVPeq (1:10 in water) and **(B)** fixed 10 AAeq. The 10AAeq and 4NVPeq are replicas (from different batches).

Table 13 shows the effect of varying the AA and PVP concentrations, always using a pH of 4, on the formation of the Cu particles. EDX data combined with the dark red color of the powder indicate that the particles were mostly Cu^0, with carbon being the only other element detected (Cu >98%, Carbon <2%). On this basis, it is clear that no PVP was associated with the particles as no nitrogen was detected. Since SEM is not an appropriate technique for surface characterization, a layer of oxide, even if thin, could and most likely exists around the particles since they were exposed to air. XPS would be a more appropriate technique for this analysis.

In terms of shape, most of the Cu crystals have the same primary structure. More specifically, small but polydisperse polyhedral structures approximately 200-400nm in size, aggregated together to form spheres with more or less the same size at higher AAeq and also to a lesser extent for NVPeq (600-800nm). Some big polyhedral structures appear, more frequently at lower AAeq and to a lesser extent in NVPeq. This was especially noticeable for the different AAeq. This was to be expected since the more concentrated the reducing agent, the smaller and more homogeneous the size of the particles would be.

Moreover, with a low concentration of capping agent, the particles will not be fully protected from aggregation thereby promoting polycrystallinity. The tendency for the formation of smaller and more monodisperse crystals was verified as both the AAeq and PVPeq were increased. However, the optimum cost-benefit equivalents beyond which there was no more significant improvement in crystal formation was at 8 NVPeq and 10 AAeq.

At least two types of mechanisms may be contributing to particle growth under these conditions. The first being the formation of small polyhedrons and aggregation and the second being the formation of a seed followed by the outward growth of multicrystals. Probably the observed agglomerates are a combination of the two mechanisms. But then, the mechanism would only be verified by exposing the crystal interior. Some fragments were also found with a hollow inside, probably derived from the first mechanism. In the image obtained for the 0 NVPeq and 15 AAeq conditions, a clear example of the second mechanism is illustrated.

Table 13 Study of the effect of the AAeq and NVPeq on the formation of the Cu-based particles at pH=4, after centrifugation and lyophilization to remove the liquid phase. Notes: 20 000x amplification. In each case, the image color is a post-modification of the original image and mimics the real powder sample.

	2.5 AAeq	5 AAeq	10 AAeq	15 AAeq
0 NPVeq	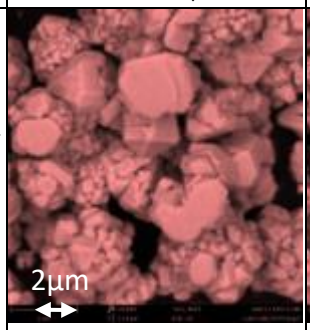	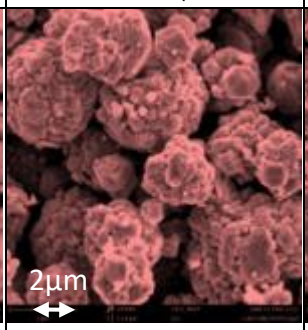	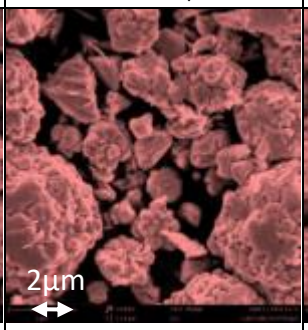	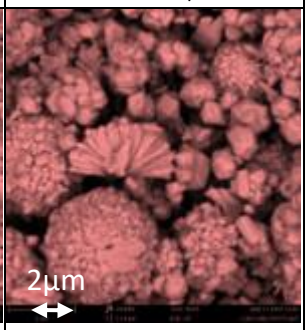
4 NVPeq	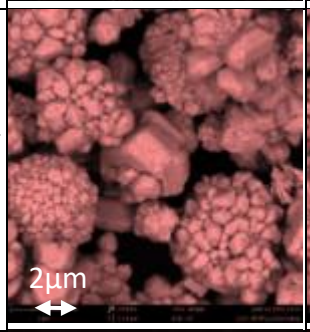	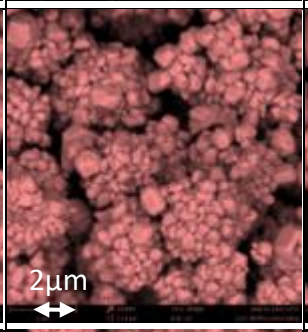	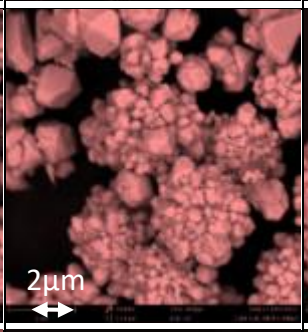	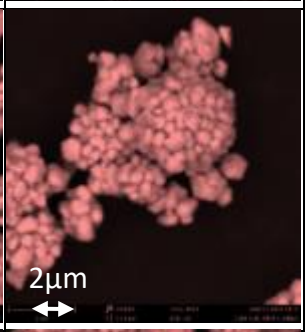
8 NVPeq	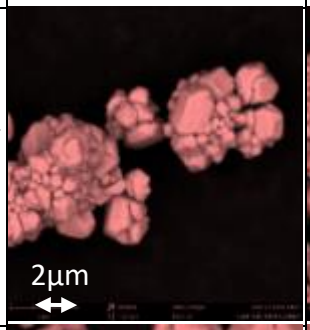	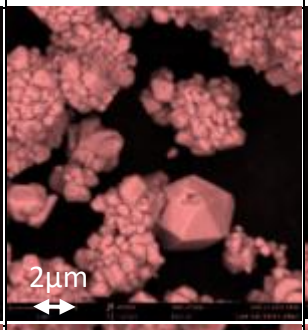	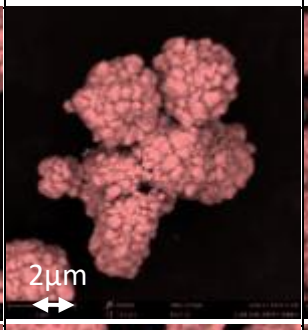	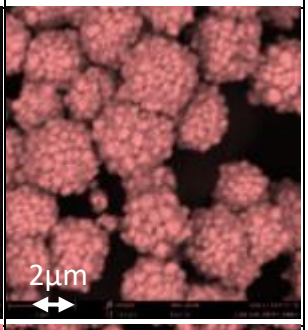
12 NVPeq	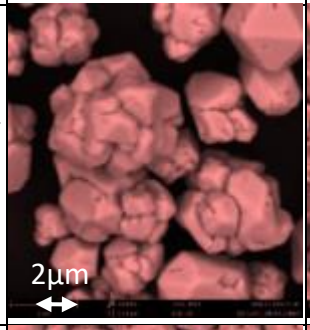	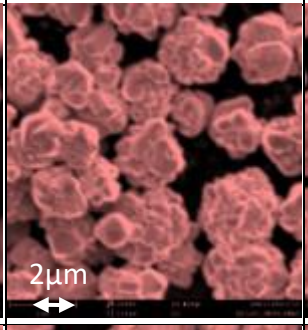	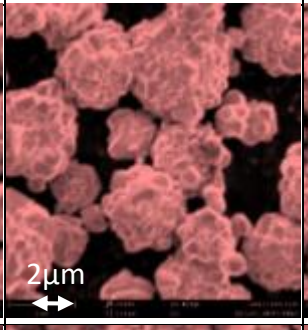	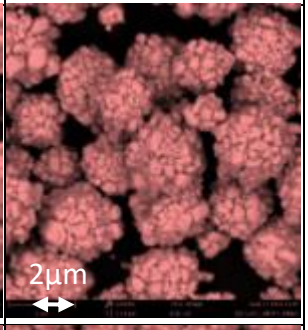
16 NVPeq	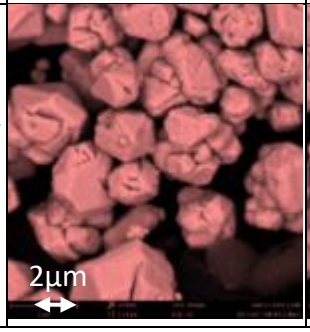	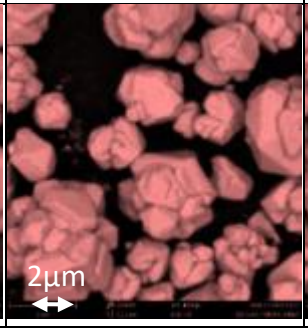	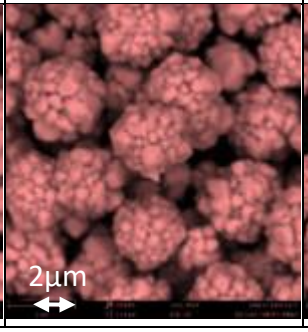	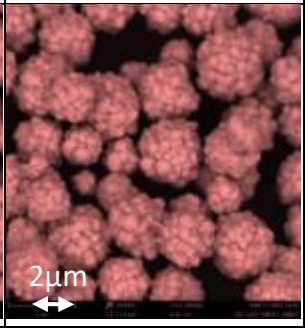

The analyses of the UV-Vis spectra of the liquid-phase of the synthesis performed at pH=4 can be found in **Fig. 18**. Assuming that the band at around 790nm corresponds to Cu ions, a 10 AAeq or higher is needed to ensure that there are no free Cu ions in solution. Also, it seems that the PVP is either aiding the redox reaction or the complexation of more Cu ions, as the band loses its intensity. Although the latter seems more plausible, this does not mean that either Cu^0, Cu_2O or CuO will be obtained. Strangely, the 16NVPeq gave a result more similar to the synthesis where no PVP was added. Since these reactions were not repeated, it is unclear if this is an error. The fact that the other NVPeq are essentially indistinguishable agrees with this theory.

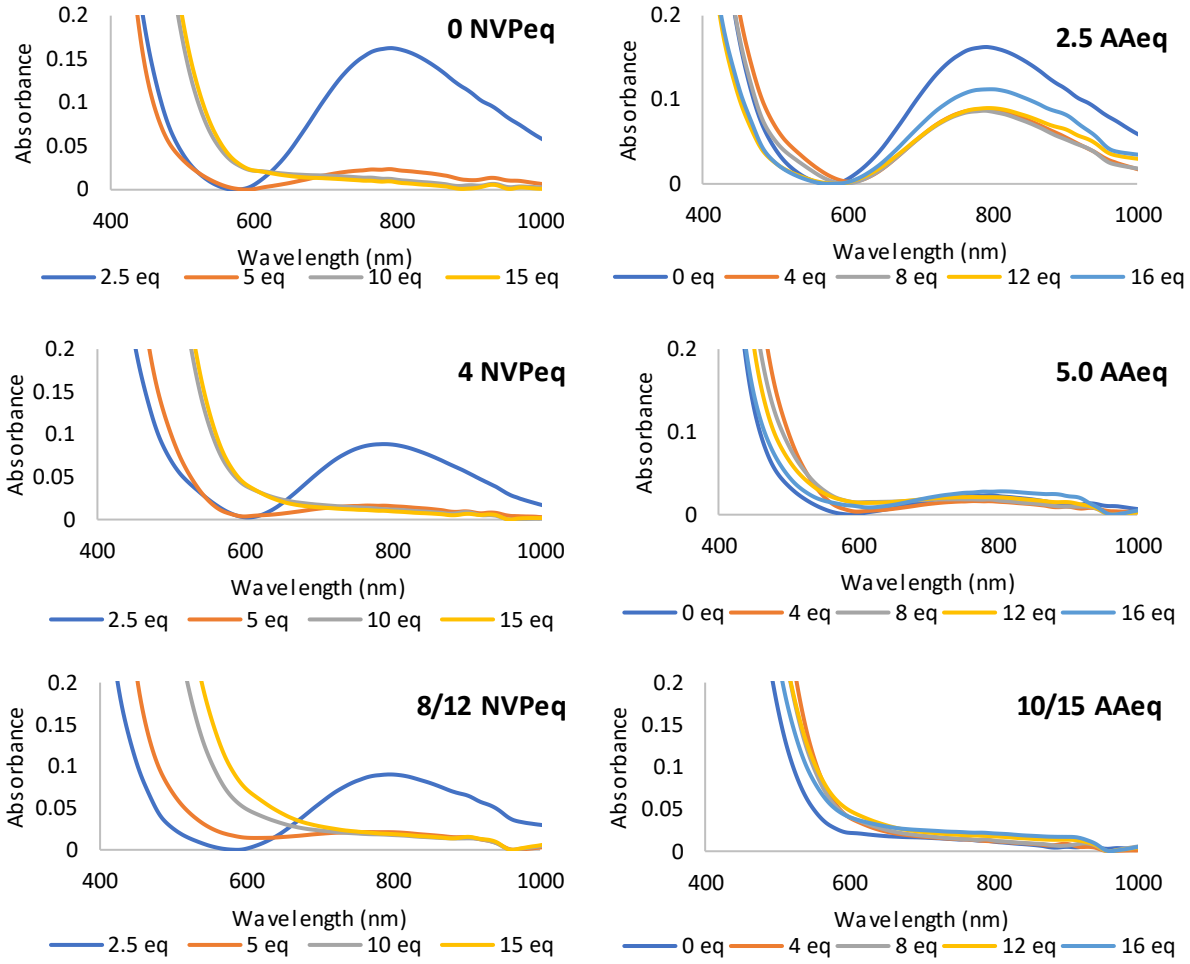

Fig. 18 UV-Vis spectra of the liquid-phase of the synthesis involving the PVP route performed at pH=4. **(Left)** Stacked spectra with the same NVPeq and varying the AAeq. **(Right)** Stacked spectra with the same AAeq using different NVPeq.

3.1.3 Complementary characterization

Interestingly, at least in the first minutes after the synthesis of the Cu-based particles prepared using the PVP polymer, some samples occasionally had a light blue (pH=4) or pink (pH=7) scatter that could be seen when the sample was directly between a white light source and the viewer's field of vision (*i.e.* at 180°). The light dispersion may be from the small particles that formed before they started to aggregate.

Resuspending the particles yielded a colloid, yet seconds later they were observed to deposit. As such, UV-Vis, PL, DLS and ELS measurements were difficult to perform and mostly disregarded altogether. Various attempts were made to keep the particles in solution: ultra-sonication, increasing the ionic strength with sodium chloride, adding more polymer to the solution, and changing the solvent (e.g. 5% DMSO in water) but with no success. The PVP may not be enough to make the Cu-based particles hydrophilic since the PVP hydrophobic alkyl chain could be facing outwards. In this case, maybe an additional surfactant such as SDS could help.

Other solvents were not tested to dissolve the Cu-based particles since the prepared samples may be of interest for medical applications and as such a biocompatible solvent would be necessary. As for the other initially proposed applications, such as the preparation of a conductive ink or particle incorporation into fibers, the solvent typically needs to be a "volatile" polymer solution. However, in this work only the biomedical application of the prepared materials was tested (section **3.4** below). Moreover, the characterization of the fluorescence properties of the liquid phase will be discussed in a separate section (section **3.3** below) since the findings are out of the scope of the original goal involving Cu-based particles and are more related with C-Dots.

3.2 PAMAM Route - Synthesis and characterization of the Cu-DENPs

Both the G4·OH PAMAM dendrimer and $CuSO_4$ starting compounds and some Cu^{2+}-G4·OH complexes prepared using different molar ratios were characterized by UV-Vis spectroscopy (**Fig. 19**). The data underwent a baseline correction by shifting the absorbance values such that at 480nm all spectra have zero absorbance (this bears in mind that 480nm is a common minimum and that there are no bands that would affect the absorbance at that wavelength). As mentioned previously, the blue Cu^{2+} solution presented a broad band with a maximum around 810nm corresponding to the $[Cu(H_2O)_6]^{2+}$ (see **Fig. 19**). In a solution containing the G4·OH PAMAM dendrimer, as the Cu^{2+} concentration increased, an increase in the absorbance at ~605nm was observed (d-d transition). The presence of a shoulder was detected at higher wavelengths when using higher Cu^{2+} to G4·OH molar ratios. The shoulder here may be a consequence of free Cu^{2+} ions in solution, since the dendrimer may be saturated and no more complexation sites are available. Furthermore, a new strong band at around 300nm appeared matching the ligand-to-metal-charge-transfer (LMCT) transition[39] (data not presented here since absorbance values higher than 1 were obtained at these concentrations; refer to Annex 3). A higher dendrimer concentration compared with that reported in the literature[123] (2 times higher) was used to improve the low signal-to-noise ratio in subsequent experiments.

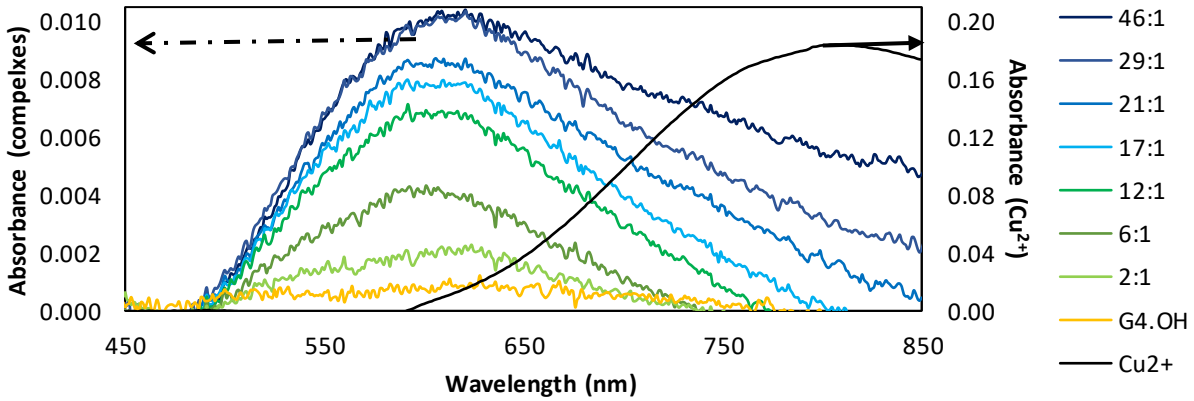

Fig. 19. Preliminary characterization of the dendrimer (_) and copper (_) starting solutions, and the Cu^{2+}-G4·OH complexes at selected molar ratios. UV-Vis spectra of the Cu^{2+} to G4·OH molar ratios of **2:1** (_), **6:1** (_), **12:1** (_), **17:1** (_), **21:1** (_), **29:1** (_) **46:1** (_).

Prior to preparing the Cu-DENPs, titration studies involving the incremental addition of Cu^{2+} ions to G4·OH were performed in order to determine the number of Cu^{2+} molar equivalents that coordinated with the maximum number of amine sites in the dendrimer interior. To get the titration endpoint, the point where the curve steepness changes must be found. Usually, in the literature, two lines are made with the experimental data (one using the first few titration points and the other line using the last points) and the endpoint is calculated at their interception[39,123]. However, there is no established way by which to determine where the linear fitting should start or finish. Moreover, the data do not present a linear correlation most of the time, especially after the titration endpoint, as can be evidenced in **Fig. 20A**.

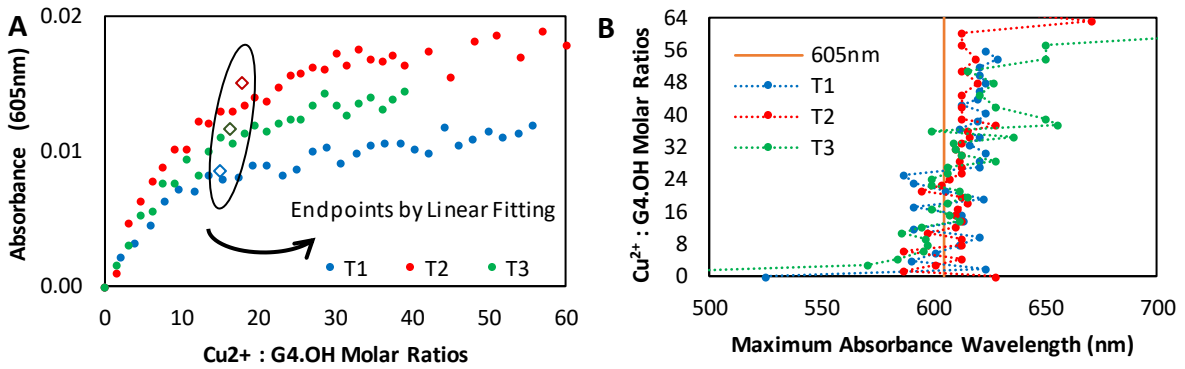

Fig. 20. The three best titration curves were obtained using a stirring time of 40s. Titration curves $\mathbf{T_1}$ using 10 µM G4·OH (●), $\mathbf{T_2}$ using 20 µM G4·OH (●) and $\mathbf{T_3}$ using 20 µM G4·OH (●). **(A)** The titration endpoints were obtained by linear fitting interception (typically used in the literature[39,123]) indicated for $\mathbf{T_1}$, $\mathbf{T_2}$ and $\mathbf{T_3}$ by (◇), (◇), (◇) respectively. **(B)** Maximum absorbance wavelength versus the Cu^{2+} to G4·OH molar ratio.

As seen in **Fig. 20**, the absorbance intensity at 605nm increased as more Cu^{2+} was added to the G4·OH solution. This was more noticeable at lower molar ratios relative to the higher molar ratios. Even though the maximum should be at 605nm, a variation of ±10nm was recorded for the different Cu^{2+} to G4·OH molar ratios (**Fig. 20B**). This deviation was even greater when using higher molar ratios. This may be because more time was required to allow for complexation to occur, which was difficult given the theoretical maximum 62 amines available for complexation[41]. The Cu^{2+}-G4·OH solution was allowed to react at different stirring times (10, 20 and 40s) and different dendrimer concentrations (10 and 20µM). The best

experiments, in terms of the Gaussian shape of the UV-Vis spectra, were found to be those performed using a stirring time of 40s and a PAMAM concentration of either 10µM (titration 1, T_1) or 20µM (titration 2, T_2 and titration 3, T_3). The latter had a slightly higher signal-to-noise ratio owing to the more concentrated PAMAM solution and as such a higher concentration of the complex.

A summary of the titration endpoint determination is presented in **Table 14**, showing that on average the Linear Fitting gives a close approximation to the expected 16:1 molar ratio[39,114,123]. Yet, this result may have occurred only by chance because if different data points had been used to make the lines, the ratio would be entirely different. A variation to a lower than expected value may be explained since dendrimers do not have a quite perfect regular shape due to manufacturing branching defects[198]. As such, some complexing groups may be missing and may thus give the impression that less copper would be required. Furthermore, the defects can provide more flexibility to the branches allowing for the formation of several more stable tetra-coordinated Cu^{2+} instead of di-coordinated ions in the crowded environment, reducing further the available amine groups.

Table 14. The titration endpoint ratios from 3 different titration experiments ("r" is the correlation index).

	Linear Fitting Interception		
	Endpoint	r_a^2	r_b^2
T1	15.0	0.887	0.750
T2	18.0	0.894	0.612
T3	16.3	0.926	0.655

3.2.1 Standard procedure for the synthesis of Cu-DENPs – the $NaBH_4$ approach

The first Cu-DENP synthesis attempt using the G4·OH PAMAM dendrimer was based on a well-established chemical reduction process in which $NaBH_4$ was added to the Cu^{2+}-G4·OH solution[39,123]. An immediate color change to orange in the Cu^{2+}-G4·OH solution following the addition of the reducing agent indicated the formation of reduced Cu (**Fig. 21A** and **Fig. 21B**). However, the solution lost its color about 15-20 minutes after taking it off the magnetic stirrer, indicating that the reaction had reverted. This was later confirmed by UV-Vis as illustrated in **Fig. 21C**. The reaction was repeated on several occasions, always getting the same result. These observations were not present in previous related works[39,114,117,123], and as such further investigation was required. One possibility may be that the Cu^0-NPs are too small and thus too unstable. In this case, a weaker reductant like AA would allow more time for the NPs to grow. This strategy was explored and is described below in sections **3.2.2**, **3.2.3** and **3.2.4**. Another possibility is that the NPs may not be properly protected given the branching defects in the PAMAM dendrimer structure. A similar result was reported by *Jin et al.*[189], where the color was maintained only for 1h while keeping the solution exposed to air (note that G3.NH_2 PAMAM dendrimers with a trimesyl core were used here instead). Crooks *et al.*[114] also reported that the Cu reverted to Cu^{2+}, but after a longer time period (*i.e.*, overnight) than was observed here.

Various efforts were made to overcome the observed results without changing the reagents, namely pH adjustment, RT versus 4°C storage temperature, and air versus inert atmosphere. The UV-Vis spectra obtained under the different synthesis conditions are

presented in **Fig. 21C** and **Fig. 21D**. In each case, the results confirmed the initial success in the formation of the Cu-DENPs, since there was a color change of the solution (**Fig. 21A** and **Fig. 21B**) and the spectra exhibited a quasi-exponential increase in absorbance to lower wavelengths[39,123]. After the recommended pH adjustment to pH 8 at the end of the reaction, a shoulder was noticed that in turn gave rise to the band corresponding to the Cu^{2+}-G4·OH complex over time (**Fig. 21C**). Tests without decreasing the pH from an initial value of ~9 were also performed, since lowering the pH increases the probability of re-oxidizing the Cu. Although this recommended pH adjustment step was removed the NPs remained unstable (e.g. in **Fig. 21D**). Under the same synthesis conditions, the storage of the solutions at 4°C versus RT was also tested in the hope that the lower temperatures would slow down the oxidation process. The result was the same for both storage conditions. Upon reviewing the literature[114,189], the Cu-DENP synthesis procedure was modified and studies were then performed under an inert atmosphere by purging the dissolved O_2 from the solutions with N_2. Once again, the UV-Vis spectra showed that after 2.5 hours the Cu reverted back to Cu^{2+} (**Fig. 21D**). Since Cu^{2+} ions were obtained after oxidation, the question arose as to whether Cu^0 was ever obtained. Perhaps Cu^+ was formed in its place. CuO would make more sense as the final product of the Cu^0 oxidation, since Cu^+ reverting back to Cu^{2+} should be easier than from Cu^0.

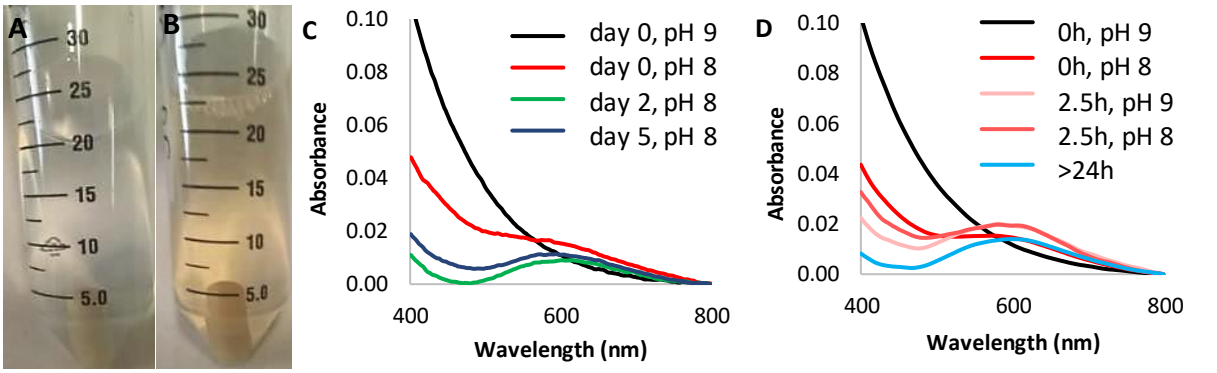

Fig. 21. Images of the synthesis solutions before **(A)** and after **(B)** the addition of $NaBH_4$. The UV-Vis spectra acquired when following the stability of the Cu-DENPs under different conditions: **(C)** reproduction of the literature[123] (solution stored at RT), and **(D)** repetition of the synthesis procedure under inert conditions when studying the effect of the last pH adjustment (solutions stored at 4C).

3.2.2 Modified procedure for the synthesis of Cu-DENPs – initial test using the AA approach

In an attempt to obtain stable and zero-valence Cu clusters, the Cu-DENP synthesis procedure was adapted such that $NaBH_4$ was replaced with AA as a reducing agent. Similar methods using AA to reduce metal ions have been reported with other supporting or surfactant materials (see **Table 3** in section **1.2.1**). This may however be the first time where AA has been used as a reducing agent to prepare Cu-DENPs.

In an initial experiment, an excessive AA to Cu^{2+} ratio was chosen (100:1). The color and turbidity of the prepared solution was followed as the reaction progressed (**Fig. 22**). The final result here was found to be visually similar to that obtained when using the $NaBH_4$ method, with the exception of this reaction appearing more concentrated (*i.e.* a stronger color was observed, **Fig. 22**). In the early stages of the reaction, the solution turned a turbid yellow. This may be attributed to an extensive nucleation period. Afterwards, as the small nuclei fuse

together, the solution slowly became clearer again. Additionally, and as anticipated from typical tests to determine reducing sugars (e.g. Benedict's, Fehling's, and Barfoed's tests), the color changed from a bright yellow (associated with Cu^{+}) to orange. This color could mean that Cu is in the zero-oxidation state or it may indicate the formation of Cu_2O (red) particles with CuO (black) impurities.

To purify the prepared sample, dialysis was first performed. However, since the synthesized sample was found to adhere to the dialysis tube (MWCO = 6-8kDa), another method was used instead. The alternative process involved a centrifugation-assisted filtration process (MWCO = 3kDa). In the last image making up **Fig. 22**, it is evident that the filtrate fraction had a yellow hue, while the concentrated fraction retained the same color after resuspending it. It should be noted that this purification step may have undesirable consequences since less AA will be present to protect the Cu from oxidizing. Moreover, the yield could be lower than expected due to the NPs being stacked in the pores of the filtration unit. Initially, the filtrate fraction color was simply believed to be a consequence of the normal oxidation of AA. However, in light of other discoveries detailed in section **3.3** it is highly likely that the color observed may be attributed to the formation of C-Dots.

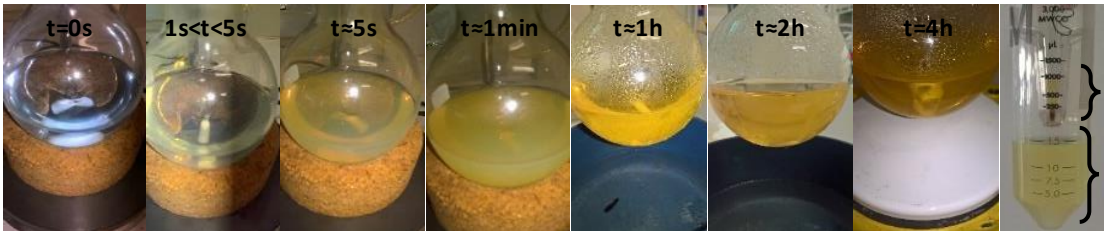

Fig. 22. Images of the progression of the Cu-DENP synthesis (initial test), where a Cu^{2+}-G4·OH solution underwent the addition of AA followed by heating. The last image to the right depicts a tube after the centrifugation-based filtration step indicating (**top**) the concentrate and (**bottom**) the filtrate fractions.

^{1}H NMR spectra of the lyophilized solutions coming from the purification process are presented in **Fig. 23**. This preliminary characterization showed that this process favored the purification of our compound of interest (*i.e.* Cu-DENPs), which did not pass through the filter and was thus retained in the concentrate fraction. This was evidenced by the absence of PAMAM signals and the presence of AA in the filtrate fraction (see **Fig. 23C**). Residual glycerin (reported at 3.65ppm; 3.8ppm) left over from the filter manufacturing process, as well as other unknown impurities, may be seen around 3.6-3.95, 4.1-4.45, and 4.6-4.65ppm (red box in **Fig. 23**). Even though the presence of C-Dots was not confirmed, if they were in solution, they could be responsible for the other unknown signals. The ^{13}C NMR would be helpful in this regard but this analysis was not performed for lack of opportunity. Moreover, the fact that these signals are present in both the concentrate and filtrate fractions may indicate that the C-Dots are attached to the dendrimer. Since the PAMAM and the C-Dots are both rich in electron donors and acceptors, they could be attached to each other with hydrogen-bonds.

The G4·OH PAMAM signals are assigned to the region from 2.4 to 3.7ppm (green box in **Fig. 23**). From **Fig. 23B**, it is clear that some AA is still present in the concentrate fraction as can be evidenced by the AA-related signals (yellow box in **Fig. 23**). Additionally, the typical signals of the PAMAM dendrimer are shifted, suggesting that the presence of Cu or the other

potential species had an effect on the overall structure of the dendrimer. In this sense, if the PAMAM dendrimer is associated with the C-Dots, then their influence on the PAMAM NMR signals would be expected.

The chemical shifts around 3.73, 4.03, 4.5, and 4.95ppm are related to AA and its by-products (yellow box in **Fig. 23**). As expected, DKG could be identified by ^{1}H NMR in a solution of AA that was left stored for months and as such degraded over time. The change in the vicinity of the hydrogens from an ester in the AA to a ketone in the DKG is the major reason for the shifts from 3.75, 4.05, and 4.95ppm to 3.7, 4, and 4.5ppm, respectively. This affects more the hydrogen labeled as "a" (AA and DKG structures inset in **Fig. 23**) since it is the hydrogen closer to the changed groups.

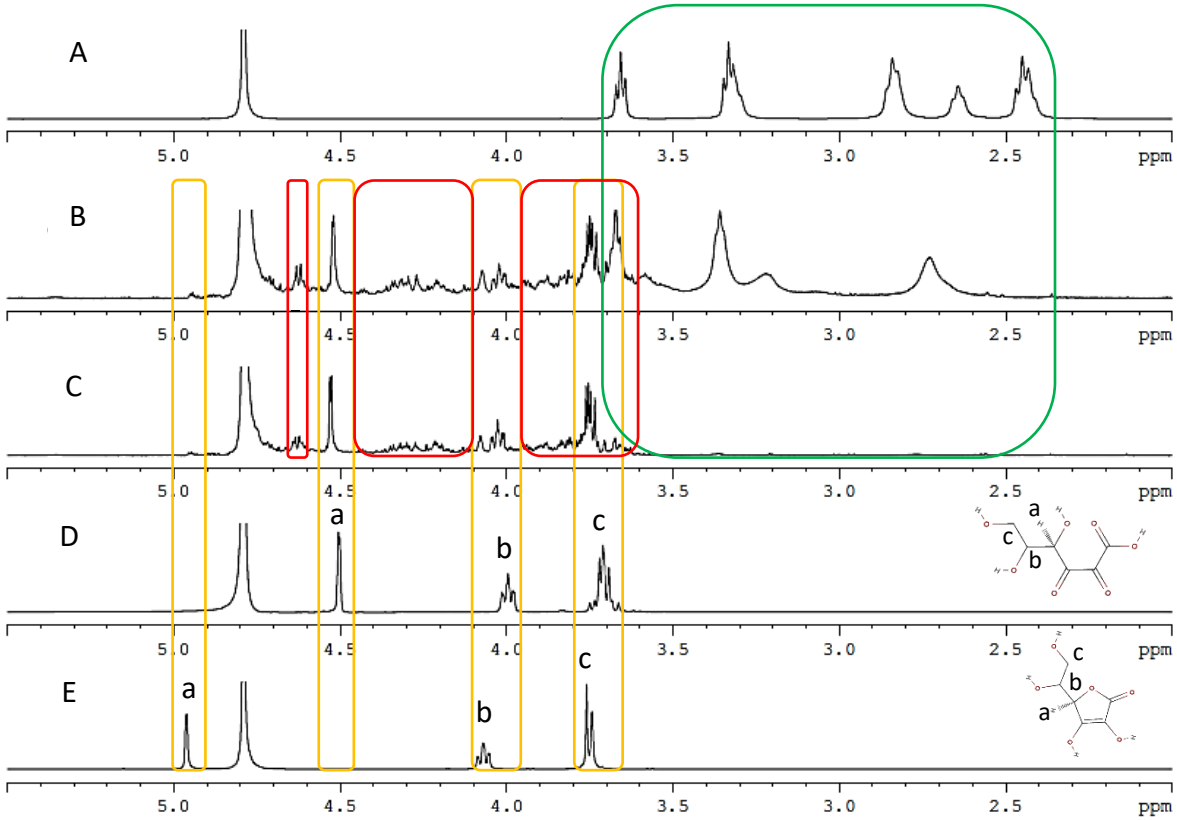

Fig. 23. ^{1}H NMR characterization of (**A**) the G4·OH PAMAM, (**B**) the concentrate and (**C**) the filtrate fraction from the Cu-DENP synthesis (initial test), as well as two solutions of AA: (**E**) one freshly prepared and the other (**D**) after several months in storage. All samples were prepared in D_2O (residual H_2O at 4.79ppm).

An absorption spectrum was done for both the concentrate and filtrate fractions and their stability were evaluated for the period of one week (**Fig. 24**). Overall, no significant difference in the spectra obtained for the two samples was evident other than the higher absorbance in the concentrate fraction. The typical quasi-exponential absorption to shorter wavelengths may be indicative of the presence of NPs in solution. The absence of the plasmon band around ~565nm suggests that if there are Cu clusters in suspension, then they must be less than ~4nm in size[7,81,123]. As was also observed previously in section **3.1**, there is a band at $^{abs}\lambda_{max}$ = 350nm, which may be related to the DHA oxidation by-products. Its intensity decreases over time, which may be associated with further degradation of the DHA into DKG, which in itself is easily degradable.

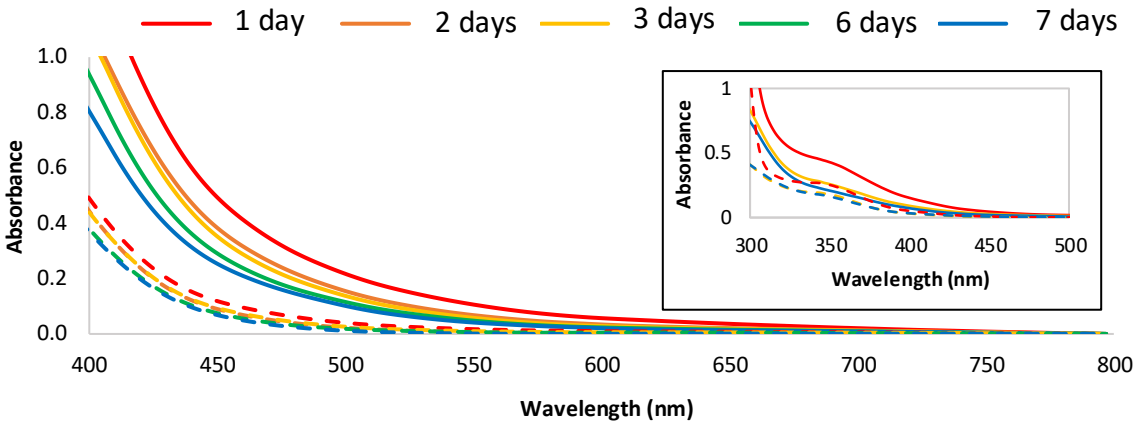

Fig. 24. UV-Vis spectra of the concentrate (**Solid line**) and the filtrate (**Dashed line**) fractions from the initial Cu-DENP synthesis procedure where AA was used. Analyses were performed up to 7 days after synthesis. (Inset: the same solutions with a 1:10 dilution in water).

In **Fig. 25,** the FTIR of the lyophilized solutions from the synthesis of the Cu-DENPs via the AA route (initial test) before and after purification were compared. Additionally, for comparison, a spectrum for the concentrate fraction from the synthesis of Cu-DENPs via the $NaBH_4$ route under similar conditions was added. Generally, all samples may be considered to be equivalent. The band at 1680cm^{-1} from the amide carboxyl group is narrower in the sample prepared using the $NaBH_4$ route when compared to the other conditions. This is expected since AA and its derivatives contribute with different carbonyl-containing groups that would all have vibrations in that region. It is implied that some AA and its by-products are still present in the final compound since the band around 1730cm^{-1} (possibly from a carbonyl group) appears in all the AA-containing samples. The signals above 3000cm^{-1} and around 2350cm^{-1} are assigned to the atmospheric water and CO_2 respectively.

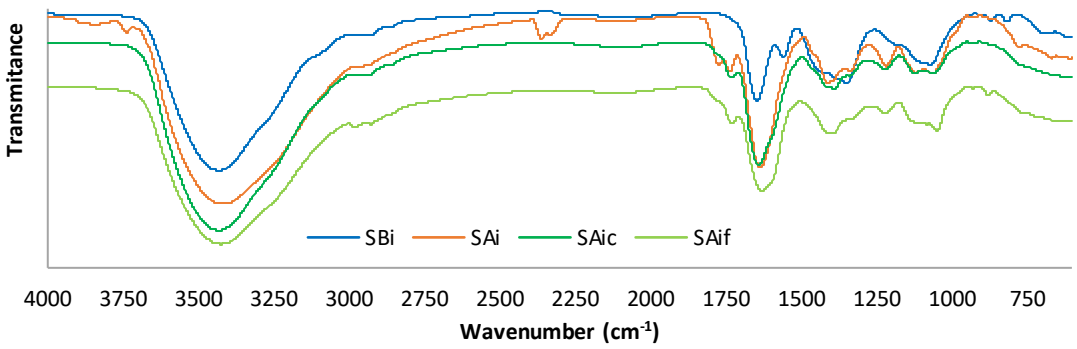

Fig. 25. FTIR spectra of the synthesized particles from the reduction using AA (initial test) before (SAi) and after purification (**c**oncentrate and **f**iltrate) compared with the synthesis route involving $NaBH_4$ under similar conditions. All samples were analyzed using KBr pellets.

On the other hand, in **Fig. 26**, the FTIR of the individual G4·OH PAMAM dendrimer and the AA components are overlaid with the concentrate fraction from the AA route (initial test). All vibrational bands from the individual components are present in the final compound, with additional bands in the 1000-1500cm^{-1} region. These new signals are usually related with either C-O and C-N stretching or with other C-H vibrations. Except for the C-N stretching from the dendrimer, any of these vibrations could arise from either the starting compounds or the AA by-products thus making the spectra very difficult to interpret.

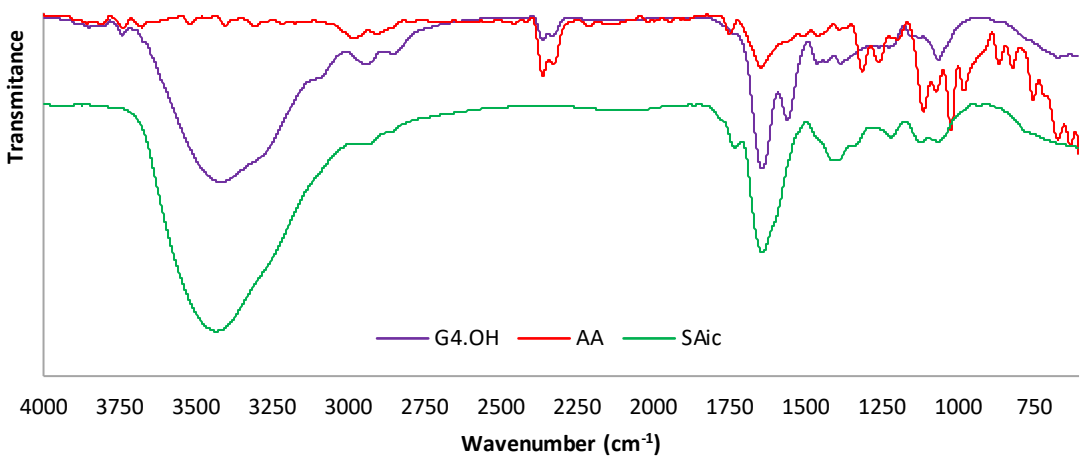

Fig. 26. FTIR spectra of the individual G4·OH PAMAM dendrimer and AA, as well as the concentrate fraction from the initial test via the AA reduction process. AA was analyzed using ATR, while all the other samples were analyzed using KBr pellets.

Some preliminary DLS measurements were made for the concentrate fraction from the synthesis of the Cu-DENPs via the AA route (initial test) and analyzed 1 day after the day of synthesis and 1 week thereafter (see **Fig. 27**). Distribution analysis puts the size of the NPs between 2-3.5nm with the presence of aggregates (data not shown). Adding this fact to the information provided by the software report that this data does not meet the quality criteria (polydispersity and high fit error) indicates that the data from this study is not reliable.

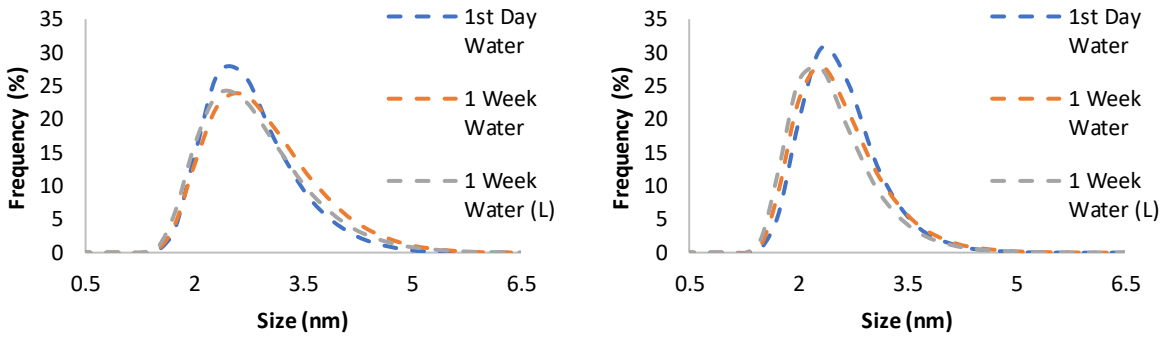

Fig. 27. Distribution analysis (**Left**) by Volume and (**Right**) by Number. Concentrate fraction from the synthesis of the Cu-DENPs at a 1:10 dilution using Milli-Q water. (**L**) indicates that a 2ml volume of the solution was lyophilized and then re-dissolved in 2ml of solvent. (Data represented as a mean of 5 measurements).

3.2.3 Modified procedure for the synthesis of Cu-DENPs – optimization process of the AA approach

Based on the physico-chemical characterization of the prepared Cu-DENPs via both routes ($NaBH_4$ reduction in section **3.2.1** and AA reduction (initial test) in section **3.2.2**), it is clear that the AA approach demonstrated more positive results. Nonetheless, the synthesis process would require optimization, namely using milder conditions. Here, as a first step to reduce the cost associated with the synthesis, the AA to Cu^{2+} ratio of 100:1 was changed to 10:1 since the AA would be still in excess relative to the stoichiometry of the Cu reduction reaction.

A typical UV-Vis absorption spectrum for the unpurified solution (crude), the concentrate and the filtrate fractions from this optimization process are represented in **Fig. 28**. According to Feng *et al.*[123], the seemingly exponential absorption to lower wavelengths indicates the formation of the CuNPs. As in section **3.1** for the Cu-based particles prepared using PVP at the same temperature of 60°C but using a pH of 7, a similar band around ~690nm is also evident here. This band however did not appear in section **3.2.2**, where the initial test to synthesize Cu-DENPs was done. Here, the purification process of the crude solutions seems to enhance this band and may probably be from something either (**i**) attached to the dendrimer or (**ii**) large enough to be unfiltered (MWCO = 10kDa).

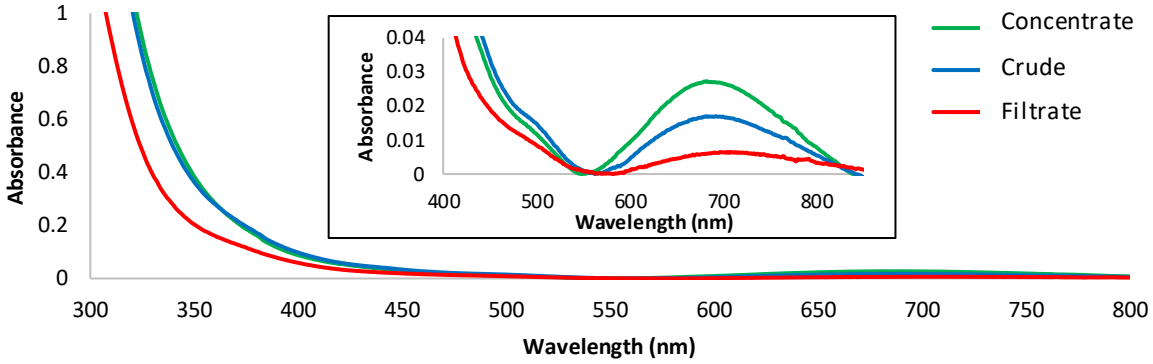

Fig. 28. Typical UV-Vis spectra of the crude, concentrate, and filtrate fraction. Inset: amplification of the small absorption band at longer wavelengths. All spectra were aligned to zero at the wavelength correspondent to the minimum of absorbance between 500 and 600nm.

The reduction in the amount of AA used during synthesis led to a substantial decrease in the interference of the NMR signal associated with AA and its by-products (**Fig. 29**). This can be verified by the absence of the signals at 3.95-4.1ppm, 4.5ppm, and 4.95ppm. Additionally, there is also a decrease in the signals at chemical shifts from 4.1 to 4.4ppm and 3.8 to 3.9ppm. These may be associated with other AA by-products other than the DKG, with C-Dots being one possibility.

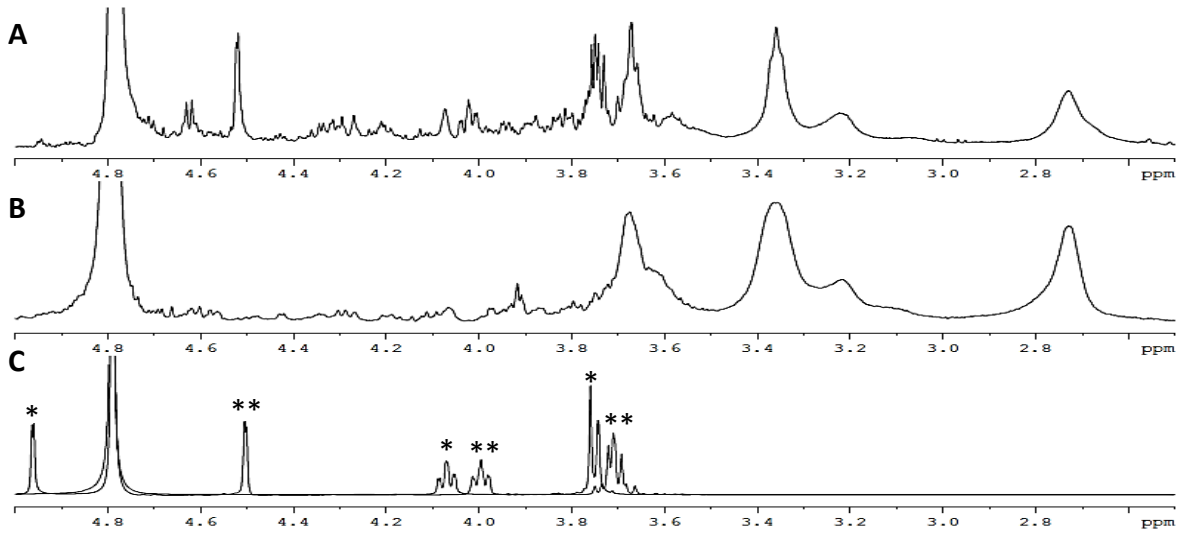

Fig. 29. Comparison of the ^{1}H NMR spectra of the concentrate fractions obtained from the synthesis of the Cu-DENPs via AA reduction, where (**A**) is the initial test, (**B**) is the optimization process, and (**C**) is an overlay of both the (*) "fresh" and (**) "old" AA solutions.

In the synthesis of the Cu-DENPs here, the original pH of 5.75 for the Cu^{2+}-PAMAM solution prior to the addition of the reducing agent in the case of the $NaBH_4$ approach was maintained instead of the newer pH adjustment of 7 in the AA approach (initial test). The reasoning for this change has been related to (**i**) the complexation of the Cu^{2+} ions to the interior tertiary amines of the G4·OH PAMAM dendrimer is inhibited at lower pH values (below pH 3.5)[41], and (**ii**) the possibility of $Cu(OH)_2$ forming is likely at higher pH values. The former possibility was confirmed by the decline of the absorption band at 605nm and the shift to 810nm (**Fig. 30**), while the latter possibility was confirmed experimentally by the formation of a precipitate. A study showing the complex stability over time was also performed and the data can be found in Annex 3.

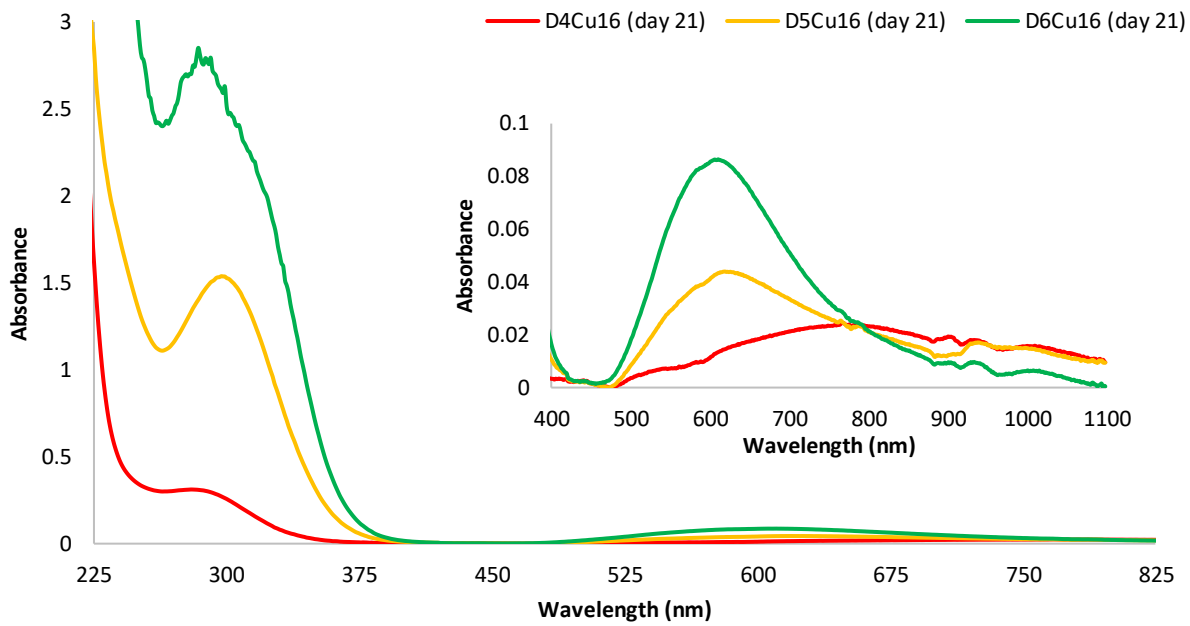

Fig. 30. Stability study of the Cu^{2+}-PAMAM complex (16 Cu^{+2} ions per dendrimer) at different pH values (pH 4 – red line, pH 5 – yellow line, and pH 6 – green line). UV-Vis spectra were acquired 21 days after the synthesis. These solutions were heated for 2h at 60°C to simulate the synthesis conditions. Inset: Amplification of the small absorption band at longer wavelengths. All UV-Vis spectra were aligned to zero at the wavelength correspondent to the minimum of absorbance between 400 and 500nm.

The effect of the duration of the heating process on the synthesis of the Cu-DENPs was optimized by following the process at different reaction time intervals (2h versus 4h in **Fig. 31** and 1h versus 2h in **Fig. 32** and **Fig. 33**). It should be noted that a synthesis procedure involving a 0.5h reaction time yielded a greenish solution overnight, after originally being yellow/orange. As such, this sample was not further characterized.

The effect of the fast or slow addition of AA was also studied over the various reaction time intervals (see **Fig. 31**). From both the ^{1}H NMR and UV-Vis spectra, it is clear that no differences occur when using a reaction time of 2h and 4h. The same result was evident for the reactions involving the fast versus the slow addition of AA.

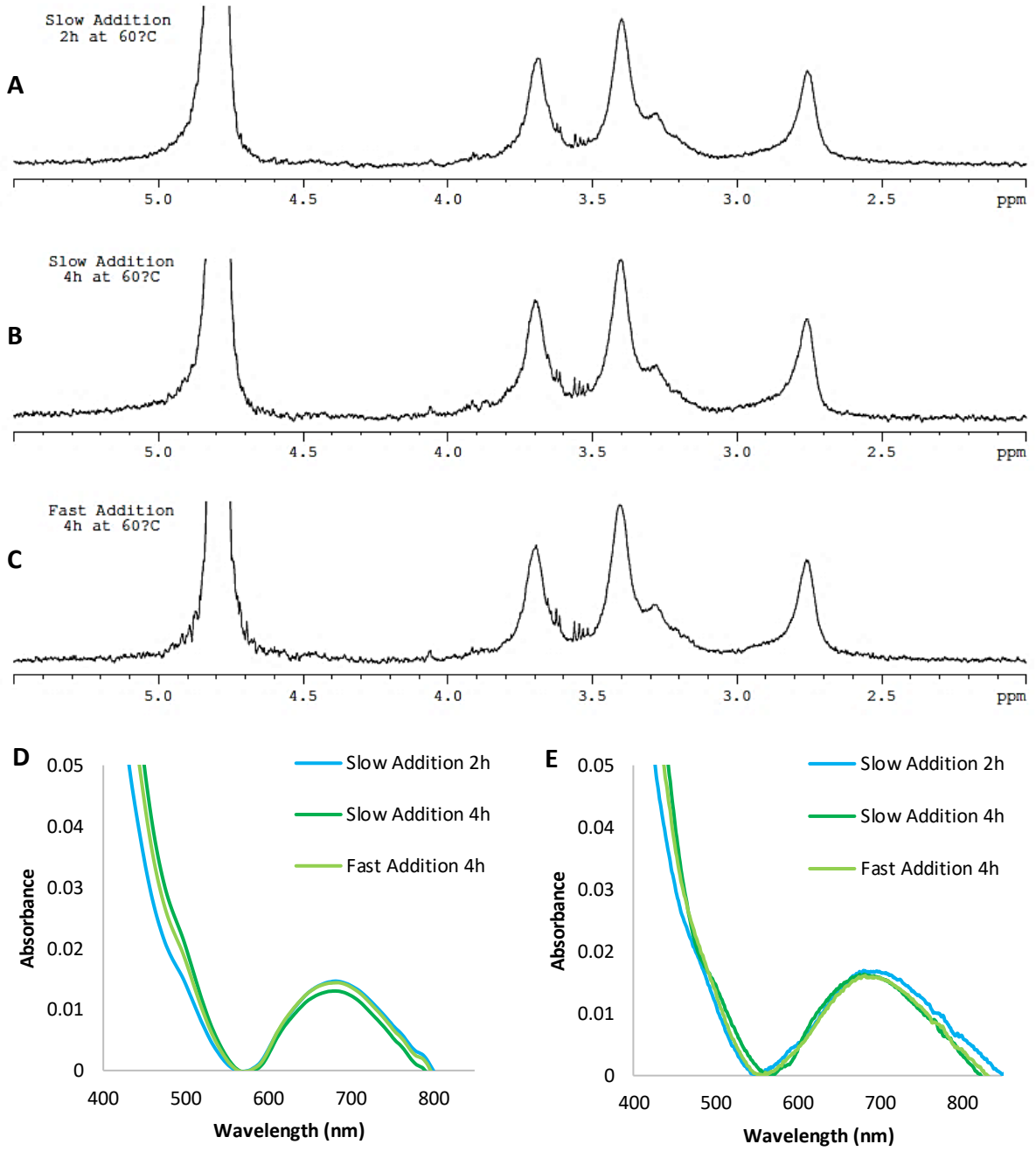

Fig. 31. Comparison using ^{1}H NMR between the (**A** and **B**) slow and (**C**) fast addition of AA in the synthesis of the Cu-DENPs. Also, in the same spectra, the effect of the reaction time intervals was studied at (**A**)2h and (**B** and **C**) 4h. UV-Vis analyses of these same samples were recorded (**D**) after 2 days of sample storage, and (**E**) after 3 weeks of sample storage. All UV-Vis spectra were aligned to zero at the wavelength correspondent to the minimum of absorbance between 500 and 600nm.

Other conditions were also tested during this optimization phase of the Cu-DENP synthesis procedure: (**i**) dividing the addition of AA into equal parts over time, and (**ii**) using half of the volume of AA or half of the reaction time.

The UV-Vis spectra from **Fig. 32A** and **Fig. 32B** show that equivalent results were obtained for the various conditions related to all crude solutions (*i.e.* prior to the purification process). For instance, adding half of the AA volume at the beginning of the reaction and the remaining half at the middle of the time interval, was the same as adding the full volume of AA at the beginning of the process. Similar results were also evidenced in **Fig. 32B** for the respective concentrate fractions, except for the condition with a reaction time of 1h. Thus, the former conditions, *i.e.* (**i**), were discarded as they added an extra step and a simpler procedure was preferred. Regarding the latter conditions, *i.e.* (**ii**), the synthesis done with half the amount of AA gave comparable results to the synthesis where a regular amount of AA was used. Although using half the amount of AA would appear to be suitable for all future work/studies, it was not adopted as a molar excess of AA relative to Cu would be preferable.

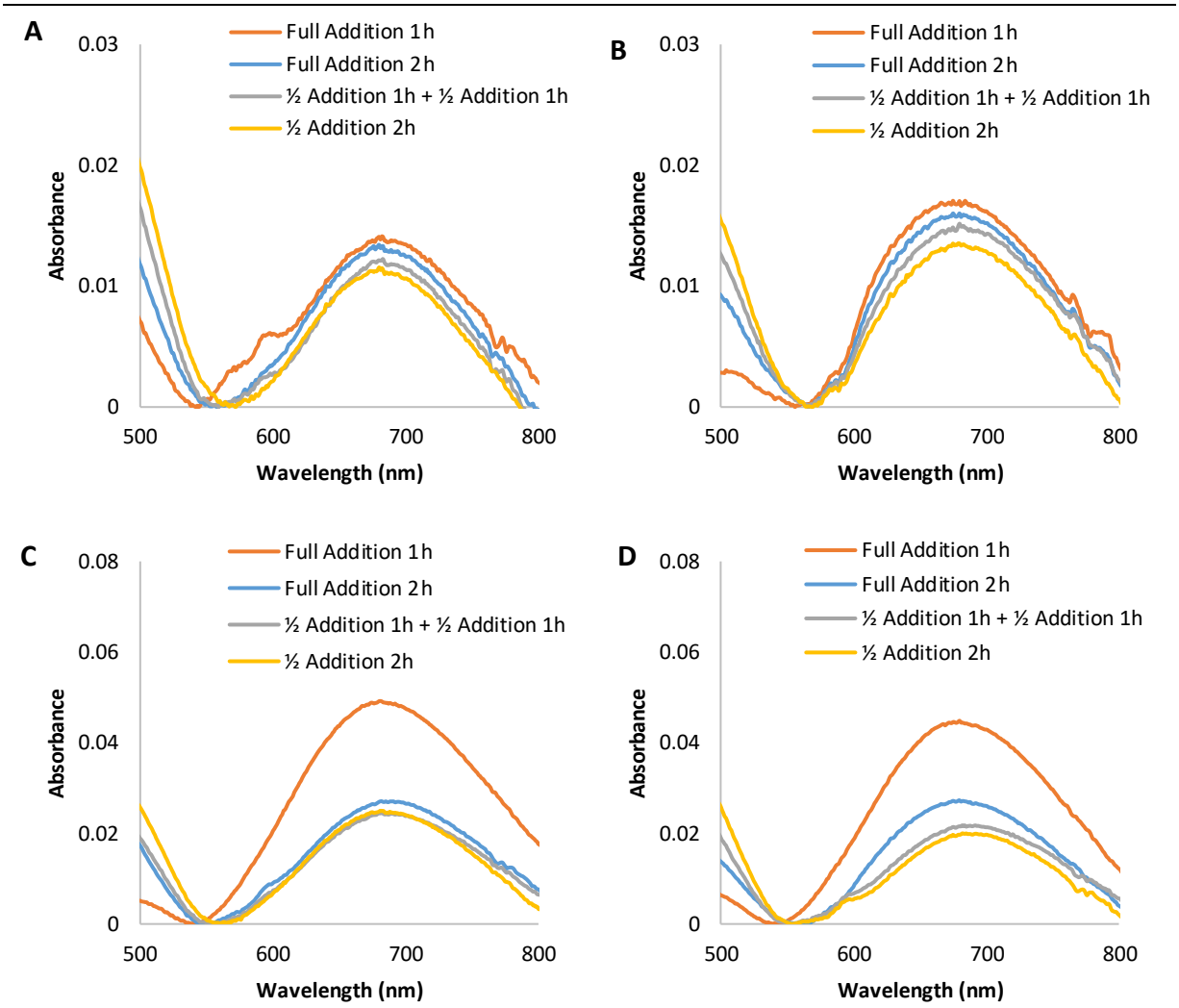

Fig. 32. UV-Vis spectra of the synthetized Cu-DENPs obtained under different AA addition conditions, which are related with (**A** and **B**) the crude solutions, and (**C** and **D**) the concentrate fractions. Additionally, counting from the day of the synthesis, the spectra were acquired (**A** and **C**) after the first couple of days, or (**B** and **D**) after one week. All spectra were aligned to zero at the wavelength correspondent to the minimum of absorbance between 500 and 600nm.

On the other hand, as can be seen in the ^{1}H NMR spectra in **Fig. 33**, longer reaction time intervals led to a shift of the signals to lower fields when compared with the condition set for 1h. Interestingly, adding a lesser amount of AA and the effect of storage time for the duration of 1 month, also contributed to equivalent peak shifts. This is particularly evident in the signal initially at ~2.65ppm but to a lesser extent on the overall spectrum.

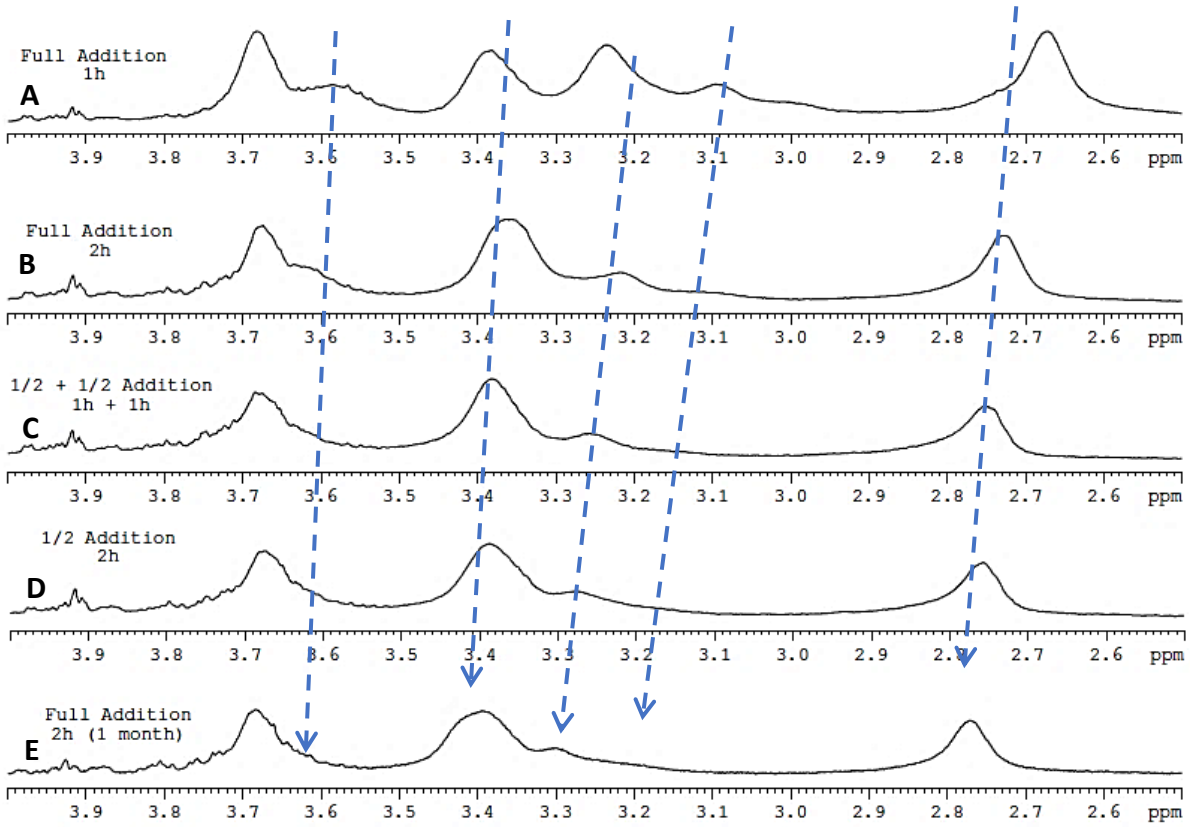

Fig. 33. Comparison of the ^{1}H NMR spectra of the Cu-DENP synthesis using the slow addition of AA under various conditions: (**A**) addition of the total amount of AA at a 1h reaction interval, (**B**) addition of the total amount of AA at a 2h reaction interval, (**C**) addition of half the amount of AA, followed by the addition of the remaining amount at the middle of the time interval, (**D**) addition of half the amount of AA at a 2h reaction interval, and (**E**) addition of the total amount of AA at a 2h reaction interval 1 month after the first measurement.

When comparing the ^{1}H NMR spectra of the Cu-DENPs and the G4·OH PAMAM dendrimer (**Fig. 34**), a clear difference in the signals was observed. While difficult to identify, this means that some phenomenon is affecting both the core, branching units, and end groups of the dendrimer. Indeed, it was anticipated that encapsulation of Cu in the G4·OH PAMAM cavities would cause significant chemical shift changes in the signal of the protons neighboring the amides.

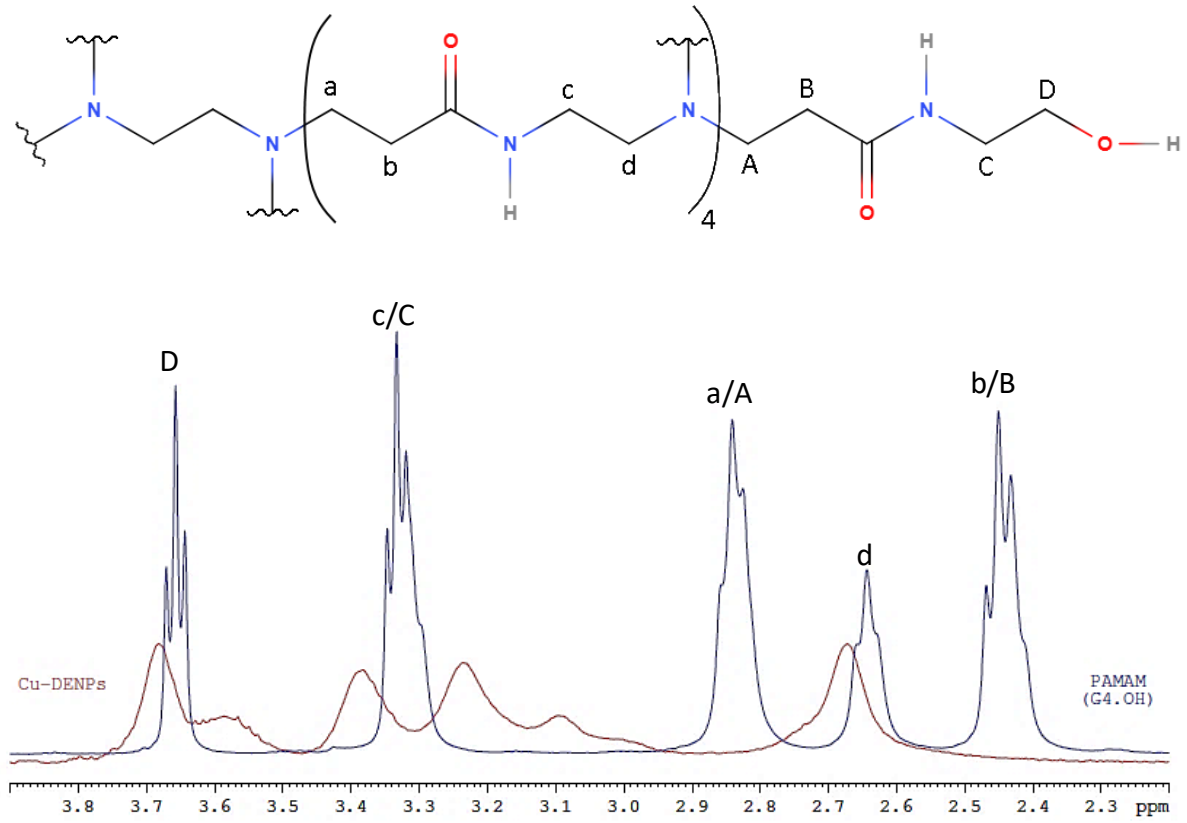

Fig. 34. ^{1}H NMR spectra of the Cu-DENPs (full addition, 1h) and the G4·OH PAMAM dendrimer. All samples were prepared in D_2O.

The correspondence of the ^{1}H NMR signals to the protons in the PAMAM structure (**Fig. 34**) are in agreement with the reported in the literature[199].

3.2.4 Modified procedure for the synthesis of Cu-DENPs – scale-up process of the AA approach

The scale-up of the synthesis procedure is important as a considerable amount of sample is required in order to perform a series of characterization techniques. Thus, a scale-up of the Cu-DENP synthesis procedure involving the slow addition of the complete AA volume and a 2h reaction time was performed. All parameters were maintained, except that here 12 times the volume of that used during the optimization process was used instead. Interestingly, the initial orange color from the crude solution gave rise to an orange precipitate and the solution gained a green hue after concentrating. Strangely, this outcome gave the same UV-Vis spectra (**Fig. 35**) as the equivalent solution prepared in section **3.2.3** (**Fig. 31** and **Fig. 32**). Alternatively, 12 times individual syntheses were done on a small scale and were then mixed into a single batch. This approach however did not prevent the formation of the precipitate.

In each case, the orange precipitate was separated from the remaining solution by decantation. This process was followed by the purification of the crude solution and the drying of the precipitate. The concentrate, precipitate and filtrate fractions from each synthesis route were each combined with their correspondent equivalent and treated as a single sample.

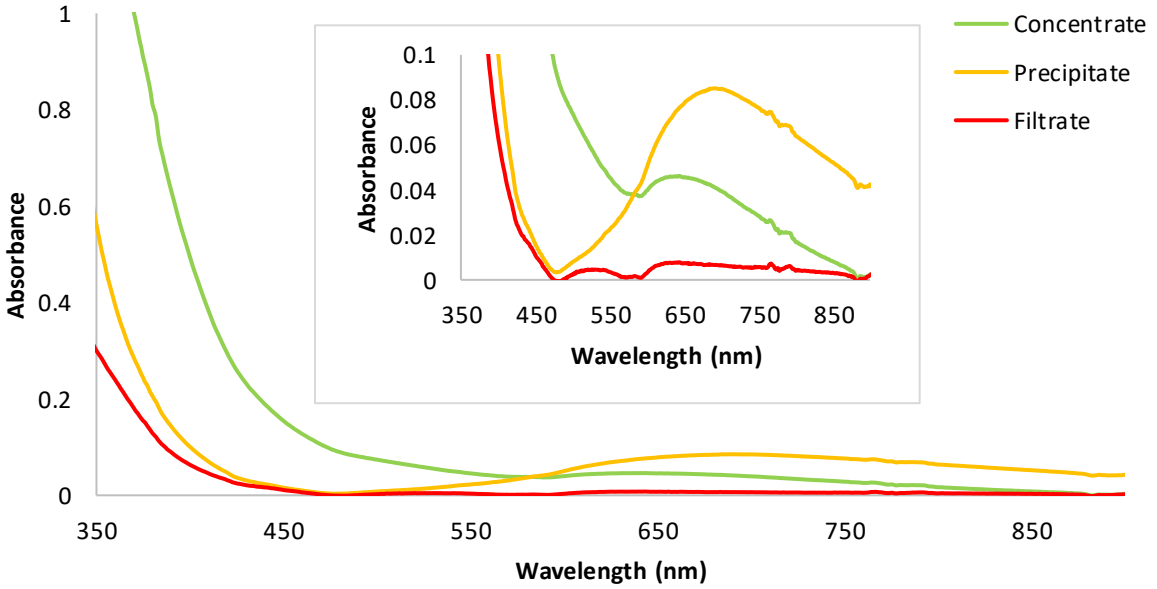

Fig. 35. UV-Vis analysis of the concentrate, precipitate, and filtrate fractions from the synthetized Cu-DENPs (scale-up). Inset: Amplification of the band at longer wavelengths. All spectra were aligned to zero at the wavelength correspondent to the minimum of absorbance.

In the ^{1}H NMR analysis (**Fig. 36**) it was evident that the scale-up synthesis was similar to the standard small scale synthesis procedure, with the exception of the appearance of a new signal in the ^{1}H NMR spectrum at around 3.9ppm.

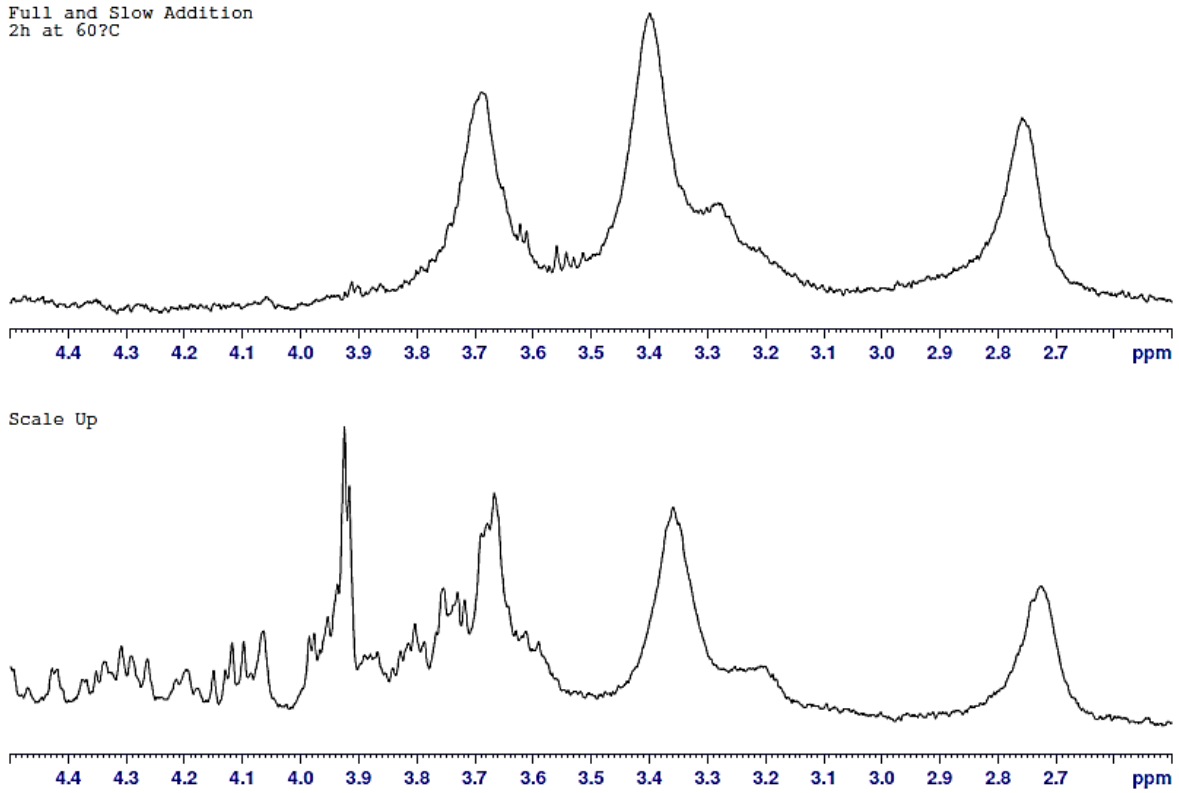

Fig. 36. ^{1}H NMR comparison between the crude solutions from both the small scale and scale-up synthesis procedures under the same conditions.

The precipitate along with the other lyophilized solutions were visualized under the SEM. SEM analysis of the precipitate sample showed spherical particles with sizes between 320 and 420nm (**Fig. 37**). Also, the particles were mostly surrounded by an organic phase that likely corresponds to the PAMAM dendrimer and some AA or AA by-products. EDX analysis indicated that the composition of this same sample was about 50% C, 32% O, 2% N, and 16% Cu. These results are quite different from the theoretical Cu^0_{16}DENPs composition: 61.5% C, 18.5% O, 18.4% N, 1.6% Cu.

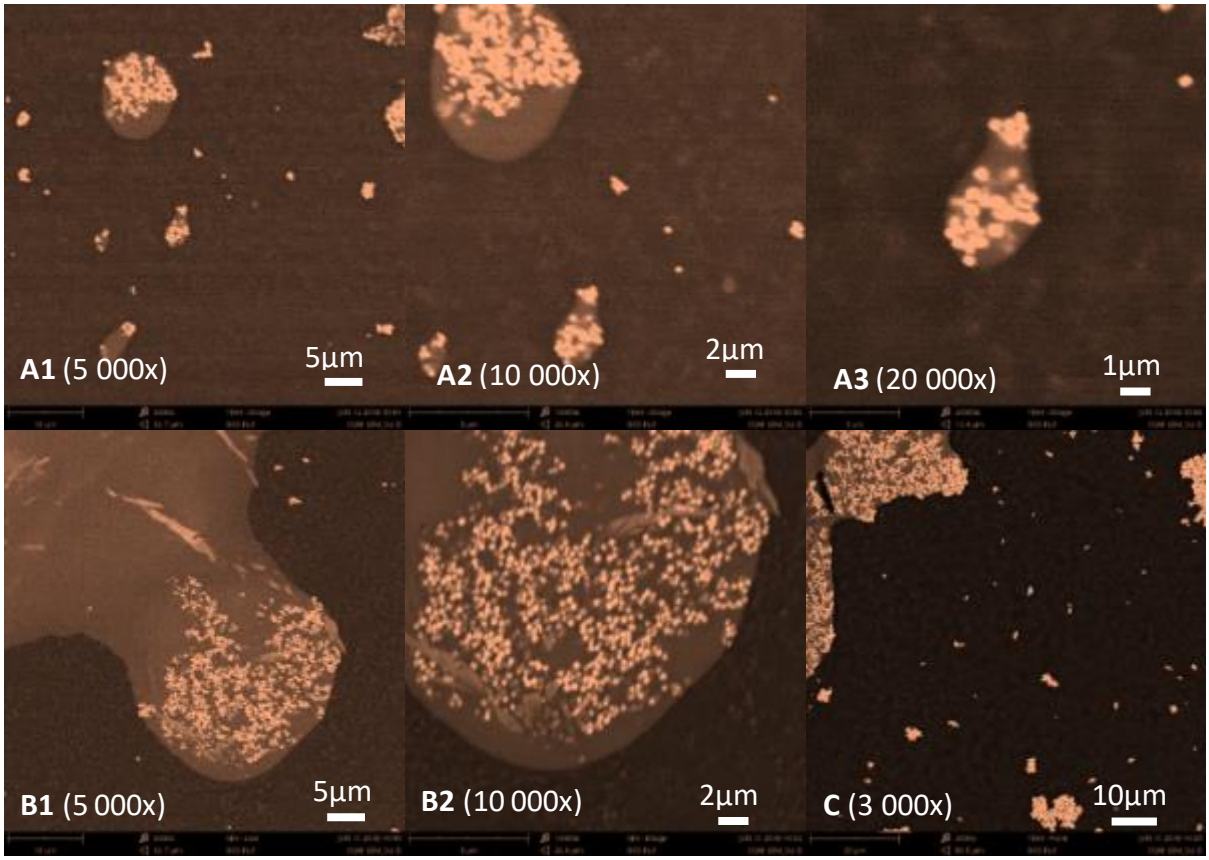

Fig. 37. SEM images of the precipitate sample coming from the scale-up process. The image color is a post-modification of each original image that mimics the real powder sample.

Two types of particles can be found in the concentrate fraction from the scale-up process for the synthesis of Cu-DENPs (**Table 15**), and indeed some Cu was still detected by EDX. Thus, the sphere-like particles may be associated with the Cu-DENPs. Yet, a steadier characterization, for instance with XPS would be required to confirm this. As expected, these particles appeared smaller than the ones from the precipitate. However, reliable size measurements could not be acquired because it was difficult to capture focused images of the particles. The needle-like structures evident in the concentrate fraction (SEM images in **Table 15**) should mostly be the result of sodium sulfate formation that arose from the $CuSO_4$, and from the pH adjustment with NaOH. As expected for the filtrate fraction, an amorphous appearance was detected. The sample was degraded by the beam as evident by the formation of holes in the SEM image at 5 000x, even though the analysis was done at -20°C. Knowing this fact *a priori*, and also that the CuNPs would be too small to be seen by SEM, this analysis was

not done for all the other Cu-DENPs described in previous sections (**3.2.1**, **3.2.2**, and **3.2.3**). Some crystals were also visualized, once again most likely attributable to sodium sulfate.

Table 15. SEM images of the concentrate and filtrate fractions. The image color is a post-modification of each original image and mimics the real powder sample.

	5 000x	10 000x	Composition by EDX (%)	
Concentrate	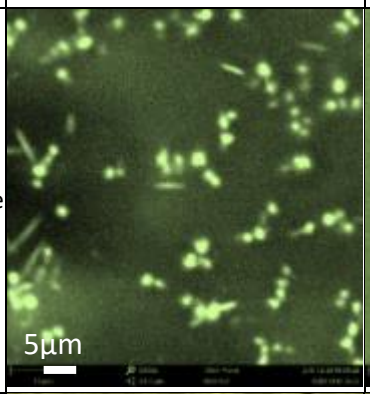	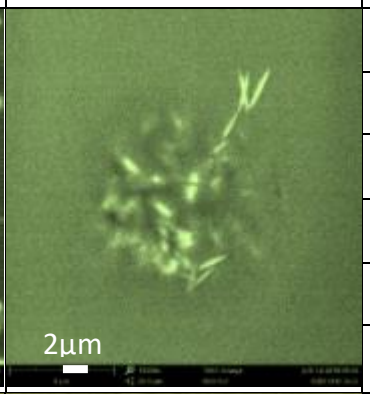	Oxygen	59.7
			Carbon	19.6
			Sodium	9.0
			Nitrogen	8.8
			Sulfur	2.1
			Copper	0.8
Filtrate	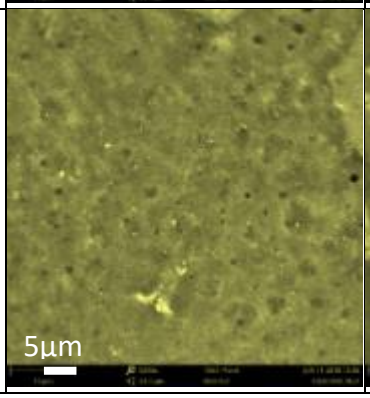	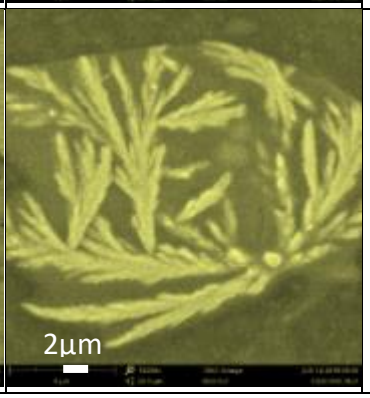	N/A	

Some concentrate fraction from the Cu-DENP synthesis via AA reduction (optimization and scale-up) were evaluated by DLS (**Fig. 38**). The precipitate sample could not be analyzed since it could not be resuspended in solvent. Distribution analysis placed the size of each sample between 2-4.5nm with the presence of aggregates, which contributed to a high correlation error. Thus, as seen in section **3.2.2**, a reliable analysis of the data was not possible.

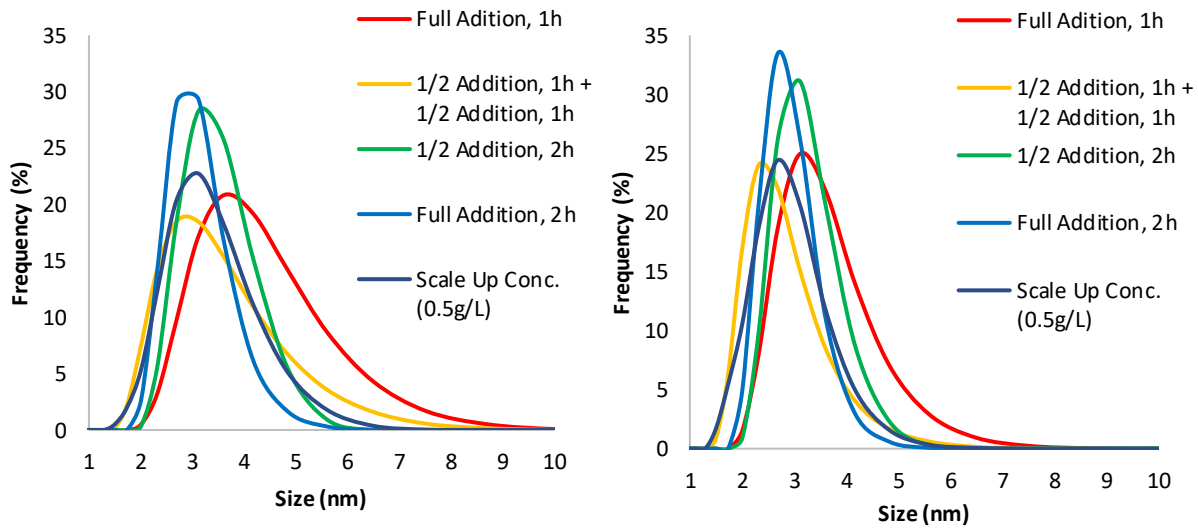

Fig. 38. Distribution analysis (**Left**) by Volume and (**Right**) by Number. PAMAM synthesis route, 2nd procedure. (Mean, n=3).

3.3 Liquid-Phase - Carbon-based Dots (C-Dots)

Given the possibility that Cu clusters with up to 13 atoms were synthesized, according to Wei *et al.*[7] this may be translated into the emission of fluorescence ($^{ex}\lambda$ ~ 250-325nm and $^{em}\lambda$ ~ 300-400nm). Indeed, a white colored fluorescence emission was seen upon irradiating the centrifuged solutions (liquid-phase) under a UV lamp (366nm). Even though the fluorescence properties of the solutions may come from the metal clusters, the lack of more substantial characterization and literature make it difficult to confirm this conclusion, especially since other species may be responsible for the emission properties. On this basis, most of the solutions from both the PVP and G4·OH PAMAM synthesis routes were analyzed by fluorescence spectroscopy.

The low probability of forming Cu clusters in the case of the PVP synthesis route, where large particles were obtained, leads our reasoning towards other hypotheses. Besides, the excitation-dependent emission observed in preliminary fluorescence spectroscopy studies pointed to the presence of more than one fluorochrome group that emits in a strict wavelength region. AA, PVP, and the PAMAM dendrimer alone should only have residual (if any) fluorescence, and some dim emission was certainly seen under a UV lamp (366nm). Nevertheless, the fluorescence spectra of the controls were studied along with their respective synthesis products. The controls passed through the same pH and temperature treatment as that used in their respective synthesis process. Also, all solutions had the same equivalent final concentrations for each compound, so it would be easier to compare their individual influence. It should be noted that fluorescence intensities are recorded in arbitrary units and that even using the same equipment and conditions the intensity may vary between measurements.

The only way to explain the fluorescence emission of AA is from a conjugation system that would cause a redshift of the absorption to the visible region of the electromagnetic spectrum. Depending on the pH, the deprotonation of the hydroxyl group on carbon-3 (**Fig. 39A**) may facilitate the delocalization of the electrons along the ring, thus explaining why AA has a more acidic character than expected. This delocalization is also known to occur in the ascorbate radical accounting for its stability and low reactivity compared to other radical species. In the case of PVP, it is known that it has intrinsic fluorescence from the aggregation-induced emission effect of its pyrrolidone ring luminophores ($^{em}\lambda$ ~ 380nm). Moreover, its oxidized hydrolysate has enhanced fluorescence from the formation of a secondary amine oxide (**Fig. 39B**)[200].

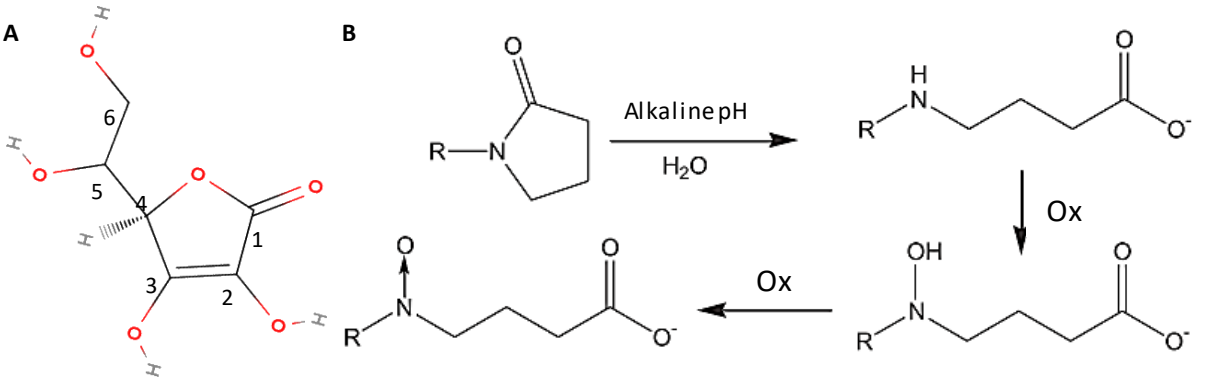

Fig. 39. (**A**) Structure of AA showing the numbering of the carbons. (**B**) Mechanism of the hydrolysis of the pyrrolidone ring and the oxidation of the secondary amine (adapt.[200]).

It is well established that the PAMAM dendrimer also has some intrinsic fluorescence. Although it is known that these emission properties can be enhanced by oxidation or protonation of some groups, the exact mechanism is still unknown[201–206]. Some of the reported groups that may be responsible for the PL properties are depicted in **Fig. 40**.

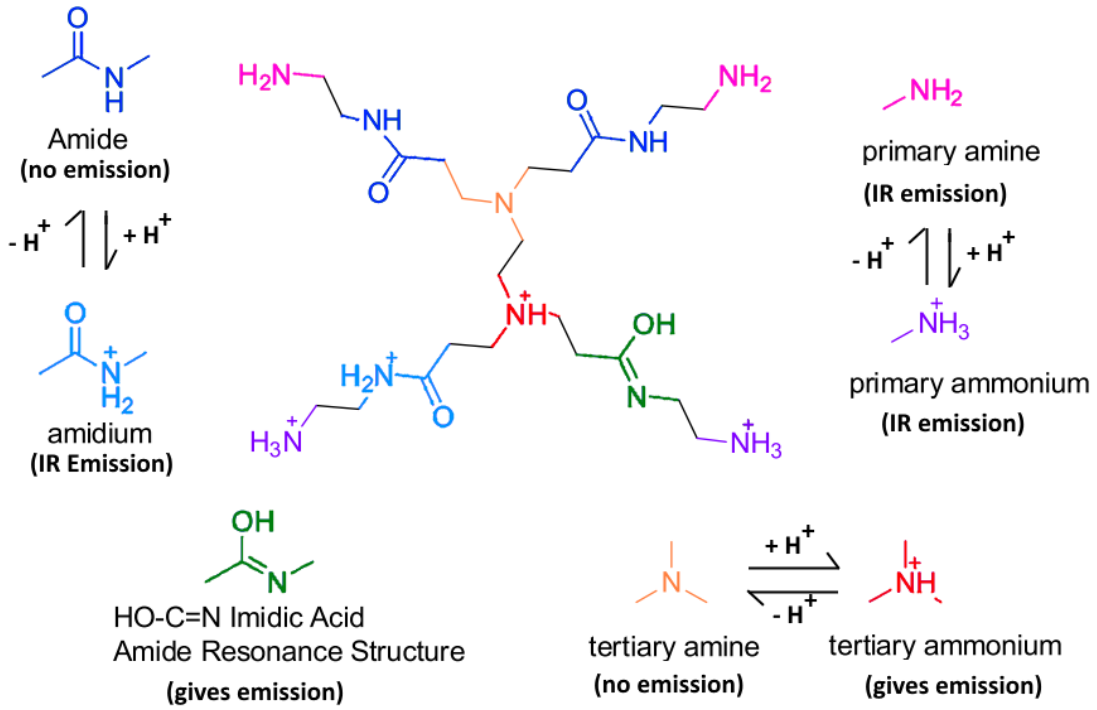

Fig. 40. Reported structures for the possible mechanisms that may explain the intrinsic properties of PAMAM dendrimers (adapt.[203]).

In light of similar results from work being developed by fellow researchers in our research group[207], a new hypothesis was made. With the aim of converting AA into C-Dots by a hydrothermal procedure, solutions having color and spectra similar to ours were obtained. Thus, upon the oxidation of the AA that was used to reduce the Cu ions in our study, C-Dots could unknowingly be formed as by-products. In this case, the different surface groups of the formed C-Dots would explain the excitation-dependent emission of fluorescence. Even if C-Dots can be formed from the oxidation of AA by itself, the reaction may occur faster and at lower temperatures and pressures if Cu is used as a kind of catalyst.

3.3.1 PL characterization of the liquid-phase from the PVP synthesis route – The effect of temperature (pH 2 and pH 4) over time

The fluorescence spectra obtained for the liquid-phase solutions from the prepared Cu-based particles via the PVP synthesis route are shown in **Fig. 41**. It is clear that both the PVP and AA controls were mostly confined in the shorter $^{ex}\lambda$. In the control synthesis (CuAA), where no PVP was used, a band at longer $^{ex}\lambda$ was evident after 4 to 5 days that was not observed in the AA control and that thus alludes to the fact that the metal is promoting the formation of a new fluorescent species independent of the PVP.

At pH 2 conditions (**Fig. 41A** and **Fig. 41C**), the reaction mixture with PVP (SN or SG) initially had fluorescence in the shorter $^{ex}\lambda$ similar to the CuAA. But an extra band at longer $^{ex}\lambda$ that does not belong to the controls was also recorded. This band may correspond to the formation of C-Dots. Over time, the second band became more intense as it shifted to higher $^{ex}\lambda$, while the first band gradually disappeared in approximately 9 days for the synthesis prepared at RT and in less than 15 days for the synthesis prepared at 60°C. This trend, which may potentially continue even more over time, was not investigated further.

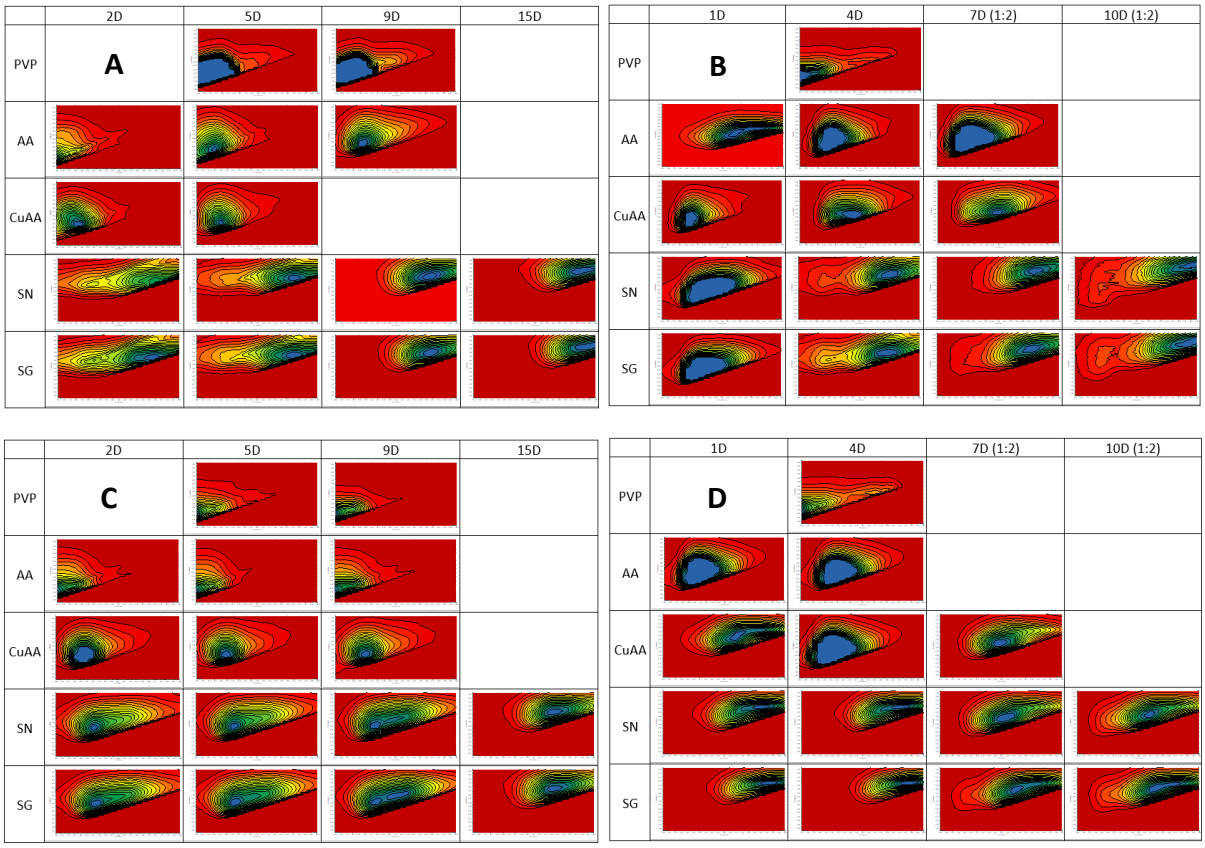

Fig. 41. Analysis over time of the EEM counter plots of the liquid-phase from the synthesis of Cu@PVP (growth-favored, **SG**, and nucleation-favored, **SN**) as well the controls: solution containing only the Cu^{2+}-PVP complex (**Cu-PVP**), solution containing only PVP (**PVP**), solution containing only AA (**AA**), and synthesis of the Cu particles without PVP (**CuAA**). The different pH and temperature conditions tested were (**A**) pH2 and RT, (**B**) pH 4 and RT, (**C**) pH 2 and 60°C, and (**D**) pH 4 and 60°C. The **Y-axis** represents the $^{em}\lambda$ (350-670nm) and the **X-axis** represents the $^{ex}\lambda$ (350-550nm). In **B** and **D**, the solutions after 7 and 10 days had to be diluted 1:2 in water since the spectra had signals greater than the maximum value measurable by the equipment. This phenomenon is evident in these spectra when a large blue stain is observed (e.g. pH 4 at RT condition, 1 day after the synthesis with PVP).

As for the liquid-phase solutions under pH 4 conditions (**Fig. 41B** and **Fig. 41D**), similar results were shown. Across all the recorded spectra, an excitation red-shift occurred that eventually ended with identical $^{ex/em}\lambda_{max}$ to those of the pH 2 conditions (but longer $^{ex}\lambda_{max}$ in the case of the controls). After 1 week, the synthesis at 60°C (pH 4) showed similar spectra to the CuAA, again suggesting that PVP was not necessary to obtain the new PL properties.

3.3.2 PL characterization of the liquid-phase from the PVP synthesis route - The effect of the AAeq and NVPeq (pH 4 and pH 7) over time

The fluorescence analysis of the liquid-phase solutions, where the NVPeq and AAeq were studied at a pH of 7 is shown in **Fig. 42**. The PL spectra were obtained 2 days after synthesis. Even without controls, the contribution of the PVP chemical groups towards the PL properties of the possible C-Dots appeared to be null, since, as the NVPeq increased, the shape of the EEM remained unaltered. Only at 16NVPeq, an overall decrease of the PL intensity was observed. Besides, as the AAeq was increased, there seemed to be a concentration-driven quenching that is hidden by the broadening of the emission bands and a red-shift of the $^{ex}\lambda_{max}$. As seen previously in the studies involving the pH 2 and 4 conditions (see section **3.3.1**.), it is possible that over time the band at $^{ex}\lambda_{max} \approx 390$nm ($^{em}\lambda_{max} \approx 450$) would disappear, and that a clear $^{ex}\lambda_{max}$ responsible for the $^{em}\lambda_{max} \approx 510$ would eventually be detected. This would probably be related with the C-Dots.

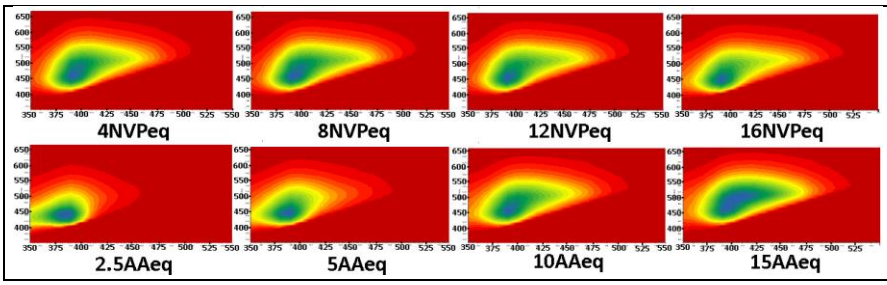

$^{Ex}\lambda_{max}/^{Em}\lambda_{max}$ (relative PL intensity)			
390/460 (1)	395/460 (1)	390/450 (1)	390/450 (0.6)
$^{Ex}\lambda_{max}/^{Em}\lambda_{max}$ (relative PL intensity)			
385/440 (1)	390/440 (0.6)	390/400 (0.4)	395/460 (0.3)

Fig. 42. Counter plots for the EEM plots of the liquid-phase of the Cu@PVP synthesis at pH 7 and at 60°C. Spectra were acquired 2 days after the synthesis procedure and the solution was diluted 1:2 in water. The $^{ex}\lambda$ (350-550nm) are depicted on the horizontal axis and the $^{em}\lambda$ (350-670nm) on the vertical axis. On the right, the values represent $^{ex}\lambda_{max}$ / $^{em}\lambda_{max}$ (the values in parentheses represent the relative intensity to that of the first equivalent in the series).

Overall, for the synthesis reactions performed at a pH of 4 and using different PVP and AA ratios, the PL spectra obtained (**Fig. 43**) were found to be very similar to those of pH 7 (**Fig. 42**). Here again, an excitation red-shift occurred when increasing the AA ratios. PVP had an effect on the PL properties of the solutions in some way because an increase in PL intensity maxima (up to 20-fold at 5 AAeq) occurred as the content of PVP was increased. However, the band responsible for the $^{em}\lambda_{max} \approx 495$nm exists in non-PVP-containing solutions and does not exist in PVP-containing solutions. From **Fig. 41** and **Fig. 42**, it was inferred that PVP does not contribute towards the PL properties of the expected C-Dots with its nitrogen atoms for example. The absence of significant $^{ex}\lambda_{max}$ and $^{em}\lambda_{max}$ variations as the PVP composition changes, reinforces this hypothesis.

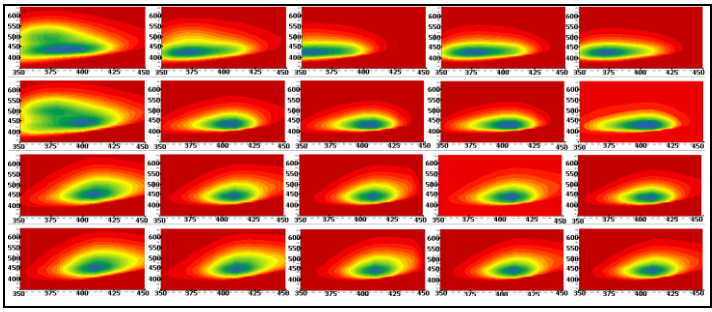

AA \ NVP	0eq	4eq	8eq	12eq	16eq
2.5eq	375/490 385/440	375/420	360/430	375/420	
5eq	380/500 400/450	405/430			
10eq	410/450	410/440			
12eq	410/460				

Fig. 43. Counter plots for the EEM plots of the liquid-phase of the Cu@PVP synthesis solutions at pH 4 and at 60°C. Spectra were acquired 2 to 3 days after the synthesis process. In the EEM plots, the $^{ex}\lambda$ are depicted on the horizontal axis and the $^{em}\lambda$ on the vertical axis. On the right, the values represent $^{ex}\lambda_{max}$ / $^{em}\lambda_{max}$.

3.3.3 PL characterization of the liquid-phase from the PAMAM synthesis route (pH 6)

The PL spectroscopy results for the initial test using AA as a reducing agent for the synthesis of Cu-DENPs are presented in **Fig. 44**. This was the first solution to be evaluated for PL since the presence of tiny clusters was more likely when using the synthesis route with the PAMAM dendrimer. Also, it was at this stage that we started to suspect that the PL had to come from another source since it showed the excitation-dependent emission usually related to multiple fluorochrome groups. The $^{ex}\lambda_{max}$ ~ 380nm and the $^{em}\lambda_{max}$ ~ 440nm found here are in accordance with those reported in the literature for the G4·OH PAMAM dendrimers ($^{ex}\lambda_{max}$ ~ 385nm and $^{em}\lambda_{max}$ ~ 450nm)[204,206]. The difference in the wavelengths may be from other species emitting at closer wavelengths to those of the dendrimer. In this case, it is assumed that the new PL properties should come from the C-Dots. These wavelengths are comparable to those recorded for the solutions prepared using the PVP synthesis route previously described in sections **3.3.1** and **3.3.2**. Moreover, these wavelengths are in accordance with the possibility of the new species with wavelengths close to those of the dendrimer being C-Dots. The band intensity at these wavelengths was followed over time. Both the excitation and emission spectra show that there is an increasing intensity over the course of 8 days (see **Fig. 44**).

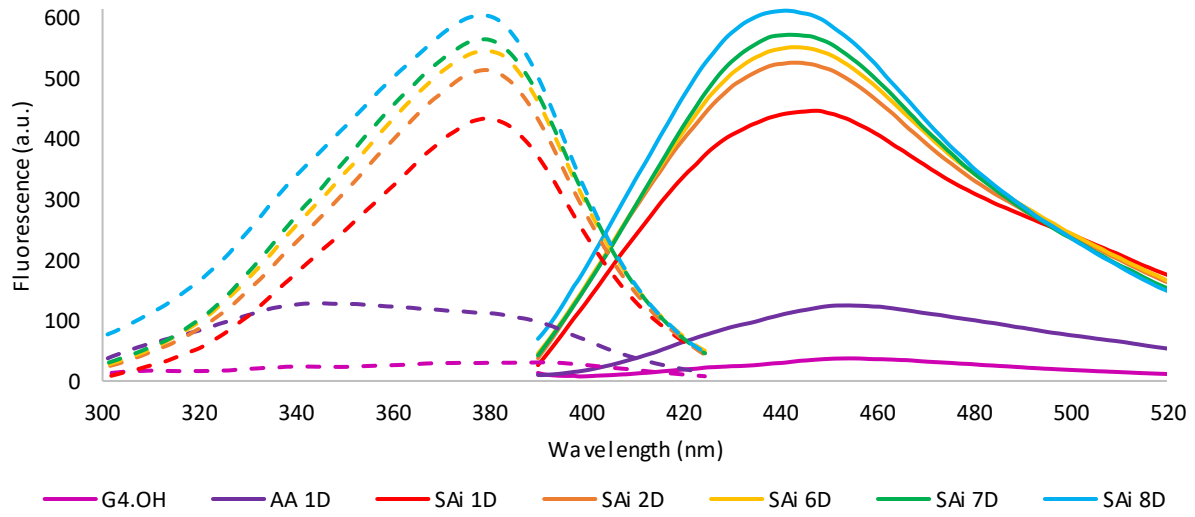

Fig. 44. PL spectra of the initial test of the Cu-DENPs synthesis (SAi) over an 8 day period. Emission spectra (solid line) were acquired by fixing the $^{ex}\lambda$ at 380nm and the excitation spectra (dashed line) were done by fixing the $^{em}\lambda$ at 440nm. Samples were diluted in water using a 1:10 factor.

Thereafter, a more in-depth analysis of the PL spectra was done using as controls the G4·OH PAMAM dendrimer alone, AA alone, the PAMAM dendrimer with AA, the Cu^{2+}_{16}DENPs, and water (**Fig. 45**). The influence of the Raman bands of water can be seen at $^{em}\lambda$ up to 400nm, while from $^{em}\lambda$ of 400nm onwards there are the excitation-dependent emissions related to multiple fluorochrome groups.

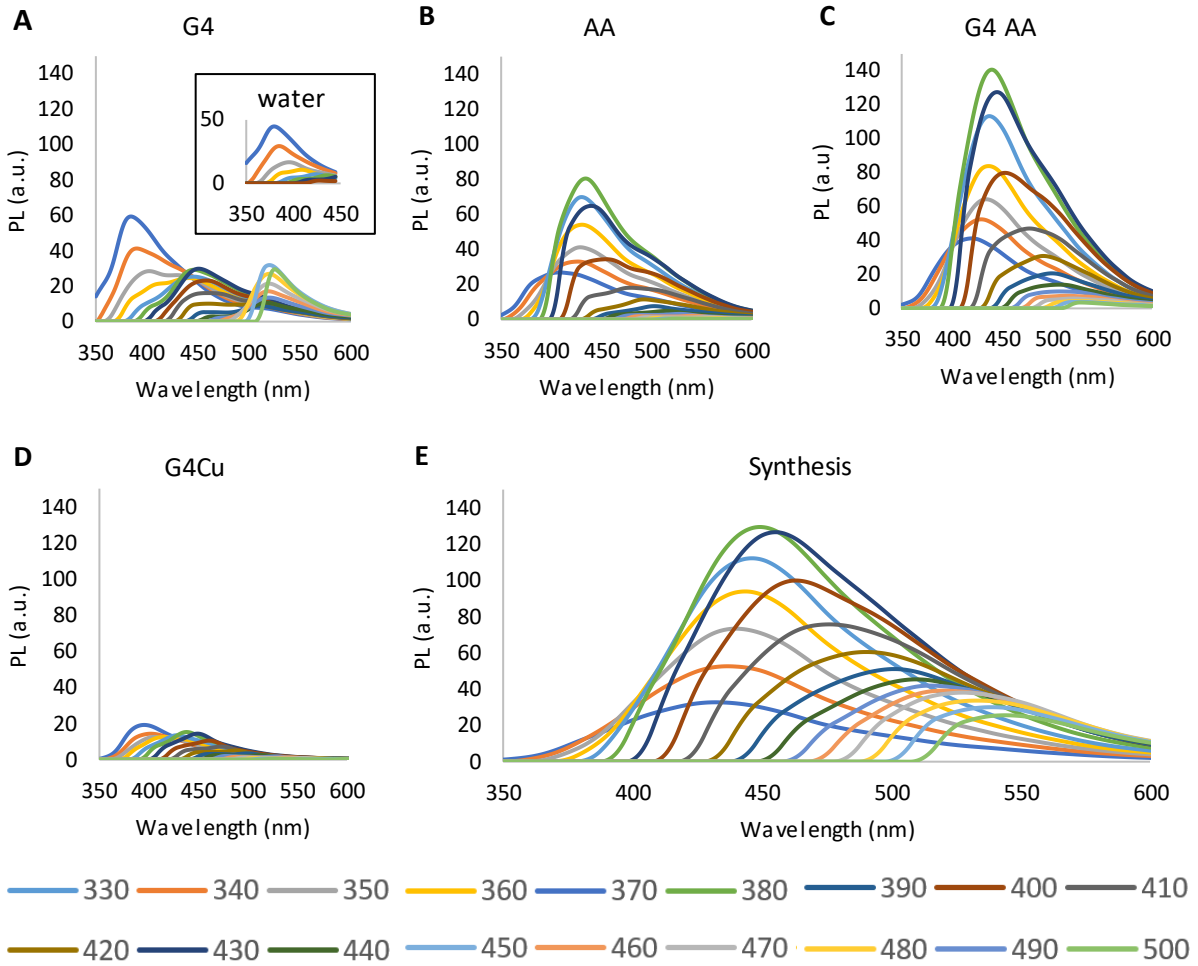

Fig. 45. Typical PL spectra obtained during the optimization process for the Cu-DENPs synthesis, in which the total amount of AA was slowly added to the reaction mixture (2h reaction time). The spectra correspond to (**A**) the G4·OH PAMAM dendrimer (inset: spectrum of water), (**B**) the AA, (**C**) the dendrimer with AA, and (**D**) the Cu^{2+}-PAMAM complex. These controls were done under the same conditions as (**E**) the synthesis of the Cu-DENPs.

The PAMAM dendrimer control also has at least two emission bands at around 450nm ($^{ex}\lambda_{max}$= 385nm) and 520nm ($^{ex}\lambda_{max}$= 490nm), plus the water Raman band. As evidenced previously, some groups like the amide/imidic acid resonance system and the tertiary ammonium may be responsible for the emissions. Complexation of the Cu^{2+} ions inside the dendrimer has a quenching effect on both bands. The band at $^{em}\lambda_{max}$= 450nm shows a decrease in the PL intensity by roughly half and the band at $^{ex}\lambda_{max}$= 520nm completely disappears. If it is assumed that each Cu ion complexes with 2 tertiary amines and 2 amides, and knowing that there are 16 ions per dendrimer, then, on average, about half of these groups in the dendrimer structure will be forming a complex with Cu. This hypothesis allows us to explain the quenching effect for the band at $^{em}\lambda$ ~ 450nm. As a consequence of the complexation, the energy absorbed by the fluorochrome group would be transferred to the

metal center instead of being emitted as light. Typically, it is assumed that both the tertiary ammonium and amide/imidic acid groups display very similar emission wavelengths, thus appearing to be a single broad band. In this case however, the most probable fluorochrome responsible for the PL properties would be the amide/imidic acid resonance system (**Fig. 40**), since it seems unlikely that the tertiary amines would be in the protonated form (*i.e.* tertiary ammonium) at the used pH of 5.75. Nonetheless, the band at $^{em}\lambda$ ~ 520nm is not reported in the literature. Thus, further studies would be needed to better understand the origin of the emission properties.

In the case of AA alone, at least 2 bands seem to be evident when using $^{ex}\lambda_{max}$= 380nm. More specifically, one band emitting at 435nm and the other emitting at ~500nm, probably from transitions such as π-π* and n-π*, respectively. In the case of adding the PAMAM dendrimer and AA together, an additive effect occurs for the band at $^{em}\lambda$ ~ 435nm in which the new spectrum recorded for the sample corresponds to the sum of each single spectrum. The second band on the other hand disappears for reasons unknown.

After the preparation of the complete reaction mixture, the acquired PL spectra are clearly a combination of the PAMAM and AA spectra with that of other fluorochromes. This is clearly evidenced by the emission dependency on the excitation wavelengths. This means that quenching from the Cu ions no longer occurs because they are no longer a complex and more importantly it is possible that the formation of the C-Dots has occurred.

The EEM plots of the filtrate and concentrate solutions from the scale-up process at different concentrations are compared in **Fig. 46**. The absence of a clear band at $^{ex}\lambda$= 490nm and $^{em}\lambda$= 520nm points to the fact that the filtrate solution does not have dendrimer (**Fig. 46A**). In contrast, the concentrate solution (**Fig. 46B, Fig. 46C,** and **Fig. 46D**) under all conditions has the same behavior as the small scale synthesis under equivalent conditions (**Fig. 45**).

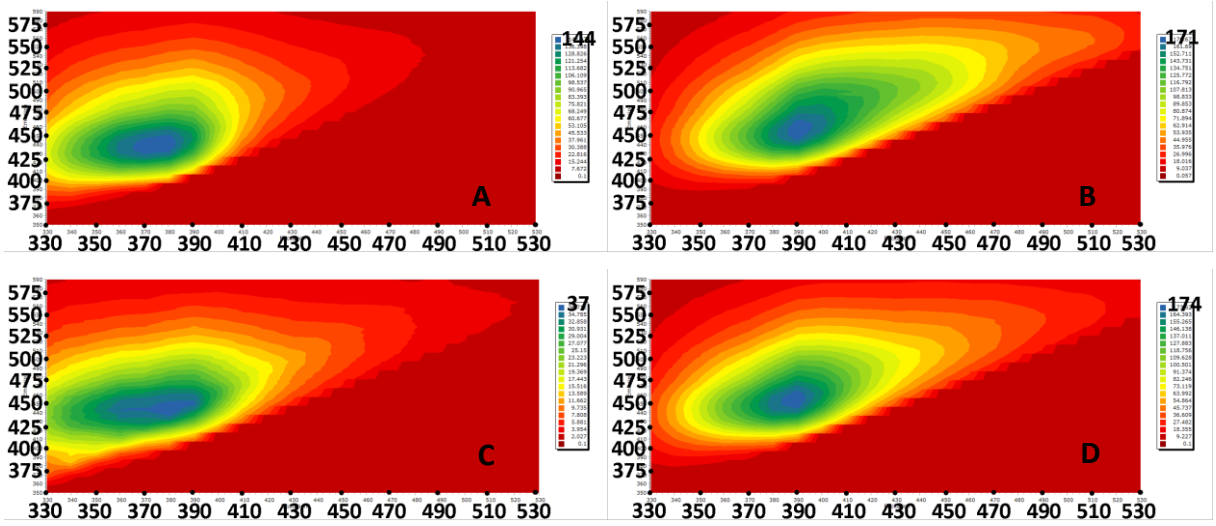

Fig. 46. Counter plots of the EEM for the solutions from the scale-up process: (**A**) filtrate, (**B**) concentrate, (**C**) concentrate at 0.5 mg/mL, and (**D**) concentrate at 5 mg/mL. The concentration of the samples for (**A**) and (**B**) are unknown as they were obtained prior to lyophilization, while the solutions for (**C**) and (**D**) were prepared by dissolving the lyophilized power in water at the respective concentrations. $^{ex}\lambda$ are depicted in the horizontal and the $^{em}\lambda$ in the vertical axis.

3.3.4 Additional characterization - Confirmation of the presence of C-Dots in the liquid-phase

Until now, the presence of C-Dots in the liquid-phase was only hypothesized. Confirmation came upon doing the analysis of some samples using TEM and XPS. Some NPs could clearly be seen in the images in **Fig. 47**. Only two samples were evaluated using this technique, both coming from the Cu@PVP synthesis route at pH=4 and 60°C, but with zero NVPeq. It should be noted that other samples are currently being tested. Only differing in the AAeq added, these particles are quite similar to each other, with rounded shape and low polydispersity. In terms of size, the particles prepared using 2.5AAeq are smaller (4.2-7.5nm, ~68% population) than when prepared with 5.0AAeq (4.4-5.9nm, ~68% population). The HR-TEM images allowed the measurement of the lattice fringes of the obtained NPs (**Fig. 47C**). The obtained value of around 2.1-2.2Å has been reported in the literature associated with graphene-based structures[208–211]. Although the particles resembled C-Dots, it was necessary to confirm the composition of the particles with another characterization technique.

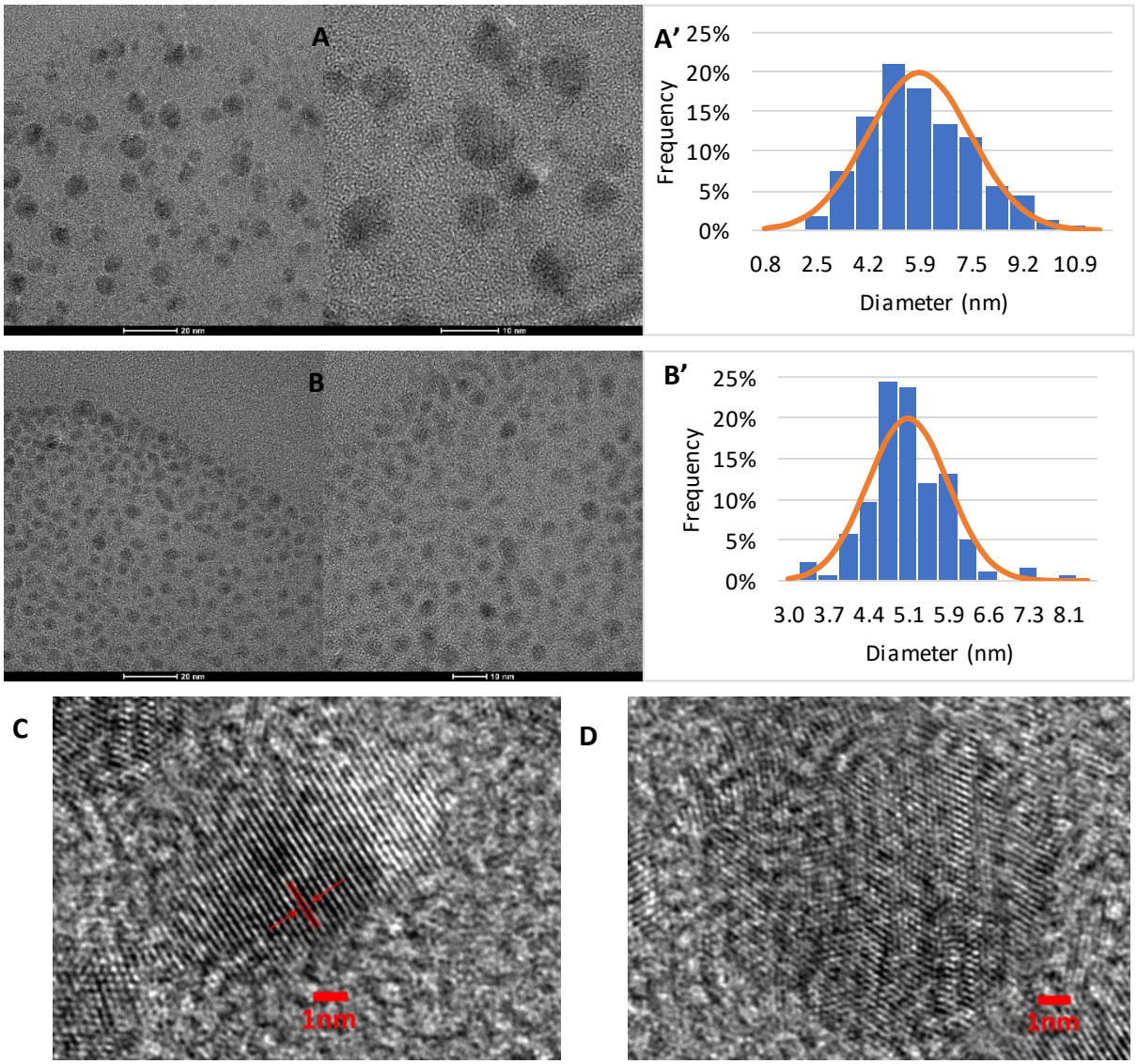

Fig. 47. TEM images of the liquid phase of the reaction mixtures prepared using the Cu@PVP synthesis route at pH 4 and a temperature of 60°C, namely (**A**) 2.5AAeq and (**B**) 5.0AAeq. The size distribution of the C-Dots obtained for (**A**) and (**B**) are depicted in (**A'**) and (**B'**), respectively. HR-TEM image with the (**C**) measured lattice spacing and (**D**) another example of other type of atom arrangement of the C-Dots.

Fig. 48 shows the survey XPS spectrum of the 2.5AAeq sample. The elements detected using this technique correspond well to the synthesis procedure used. The elements detected include C and O coming from $CuSO_4$ and AA, and sodium coming from the NaOH solution used for the pH adjustment, residual traces from the water, and impurities from the reagents. No Cu signal was found, showing that Cu was removed during the centrifugation process.

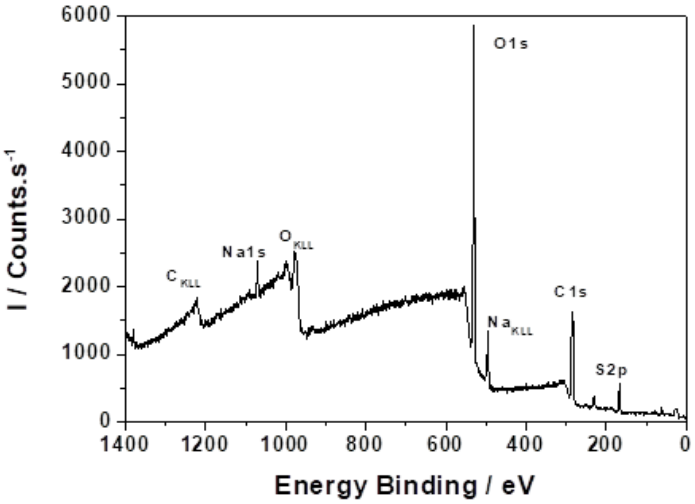

Fig. 48. Survey XPS spectrum for the 2.5AAeq sample.

The high-resolution C 1*s* core level for the 2.5AAeq sample is presented in **Fig. 49A** and compared with that obtained for the 5.0AAeq sample (**Fig. 49B**). In both samples, the C 1*s* signal can be decomposed into four main contributions, with the two main signals at 284.8 and 286.4eV corresponding to adventitious carbon (C-C or C-H) and to oxidized adventitious carbon (C-O or C-O-C), respectively. It is important to highlight the difference in the 286.4eV signal in each graph, which demonstrates the different AA concentrations used in each reaction as the carbon source. The third contribution observed at 287.6eV can be assigned to carbonyl groups (C=O). And finally, the contribution at the highest binding energy (288.9eV) can be assigned to the surface carboxylate groups (O=C-O), where the maximum appears at a lower binding energy than expected (>289eV), being significantly more important on the surface of the 2.5AAeq sample.

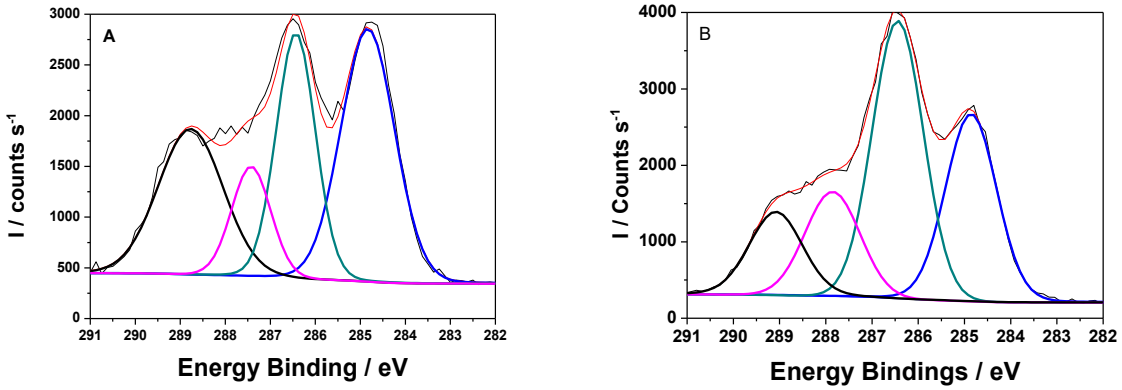

Fig. 49. C 1*s* XPS core level spectra for (**A**) the 2.5AAeq and (**B**) the 5.0AAeq samples.

In **Table 16** the different contributions found on the surface of the C-Dots are shown, with the ratio of "C-C/C-H" to "C-O/C-O-C" being 1.42 and 0.69 for the 2.5AAeq and the 5.0AAeq samples, respectively.

Table 16. Contribution to the C 1*s* signal.

	284.8 eV	**286.4 eV**	**287.6 eV**	**288.9 eV**
Group	C-C / C-H	C-O / C-O-C	C=O	O=C-O
2.5AAeq	36.8 %	26.0 %	11.7 %	25.5 %
5.0AAeq	27.4 %	39.8 %	25.1 %	7.7 %

The signal corresponding to S 2*p* (**Fig. 50A**) showed two significant peaks that can be associated with the presence of sulfate, which correspond to the spin-orbit components at 169.3eV for the S $2p_{3/2}$ and 170.0eV for the S $2p_{1/2}$. The N 1*s* core level signal presented a single peak centered at 401.8eV and was assigned to the known impurities from $CuSO_4$ (**Fig. 50B**). The O 1*s* signal seams to consist of two signals centered at 532.7eV with a contribution of 96.55% and 656.4eV with a contribution of 3.45% (**Fig. 50C**). Since the presence of at least 3 types of oxygen are expected, as seen in the XPS C 1*s* analysis, a more in-depth examination of the data is currently ongoing.

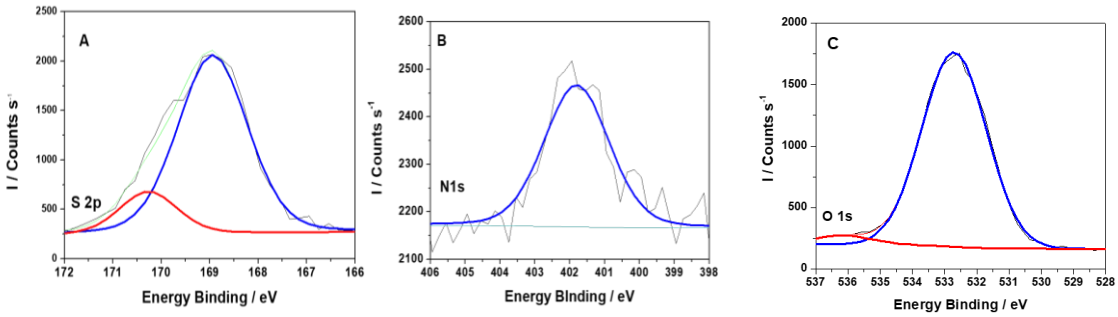

Fig. 50. XPS core level spectra of (**A**) S 2*p*, (**B**) N 1*s*, and (**C**) O 1*s* for the 2.5AAeq sample.

Atomic concentration (%) of the constituent elements was calculated by integration of the areas of the core level signals after application of a background subtraction and considering atomic sensitivity factors. These values were C 1*s* (47.6 %), O 1*s* (47.6 %), S 2*p* (4.3 %), N 1*s* (0.5 %) and Cu 2*p* (< 0.1 %) for the 2.5AAeq sample. For the 5.0AAeq sample, the values found were C 1*s* (53.5 %), O 1*s* (44.1 %), S 2*p* (1.9 %), N 1*s* (0.5 %) and Cu 2*p* (< 0.1 %).

Upon gathering the information of XPS, a model of the surface groups of the C-Dots could be built (**Fig. 51**). This analysis lacks complementary techniques like FTIR, ^{1}H NMR, X-ray diffraction, and Raman spectroscopy, especially regarding the composition/structure of the core. These characterization techniques are still an ongoing process.

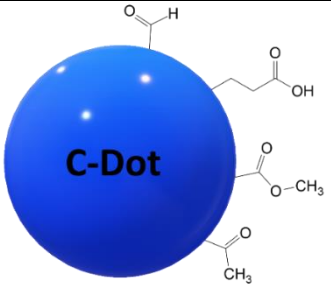

Fig. 51. Schematic representation of possible surface groups that could be found on the C-Dots based on the XPS.

Overall, the successful preparation of C-Dots using AA and Cu as a "catalyst" was demonstrated in this section. This work would be very interesting from an industrial point of view, especially since obtaining and maintaining the high temperatures typically used in the hydrothermal synthesis of C-Dots is very costly.

3.4 Preliminary cytotoxicity studies of the Cu-based particles and the C-Dots

The cytotoxicity of the Cu-based particles prepared using either PVP or the G4·OH PAMAM dendrimer, as well as that of the C-Dots, was evaluated after exposing the cells to the compounds for 48h and performing the MTT assay. A direct correlation exists between the cell metabolic activity acquired using this assay and sample toxicity. The assays performed here were a first attempt to evaluate the toxicity of the prepared particles and more research is needed in future.

One type of the Cu-based particles from either the PVP or the PAMAM dendrimer synthesis route, and one of the C-Dots were selected for testing. The particles made using the PVP route at pH=7 (8NVPeq, 10AAeq) were chosen since they were smaller and more monodisperse relative to the ones prepared at pH=4. Moreover, the particles selected here were also easier to disperse in solvent relative to the other Cu-based particles prepared using PVP. This sample will be identified as Cu_2O@PVP. From the synthesis procedure involving the preparation of Cu-DENPs using AA as a reducing agent, a small portion of sample of the concentrate from the scale-up process was withdrawn and simply identified as CuDENPs. Finally, the C-Dots sample used for cytotoxicity analysis corresponds to that acquired from the PVP route at pH=4 and under the 0NVPeq and 2.5AAeq conditions after the 2h centrifugation of the liquid-phase. This condition was selected since it was the sample that did not show agglomeration in the TEM images.

Fig. 52 shows the cytotoxicity of the Cu-based particles prepared using either PVP or the G4·OH PAMAM dendrimer, as well as that of the prepared C-Dots, on HEK 293T cells. In each case, the cells were exposed to increasing concentrations of the prepared materials in the range of 0-500μg/mL. Defining materials as being biocompatible when a metabolic activity of 80% or higher is obtained, it is clear that the Cu_2O@PVP sample demonstrates decreasing biocompatibility towards the HEK 293T cells when using sample concentrations of 0-50μg/mL (see **Fig. 52**, **orange bars**). For concentrations of 50μg/mL and higher, the Cu_2O@PVP sample is clearly toxic. The reason for these results may be linked to the PVP not protecting the surface of the particles and the Cu particles, which are known for their toxicity issues in healthy human cells [212–214], may exert their toxic effects on the HEK 293T cells. These results, combined with the fact that the sample cannot readily be suspended in solvent, limits the potential use of Cu_2O@PVP in biological applications. The use of surfactants in the preparation of the Cu_2O@PVP sample may however resolve these issues. An alternative would be to engineer a system that may be used to coat surfaces with this material, and that may then be suitable for antimicrobial and antifouling applications.

Analysis of **Fig. 52** (**green bars**) clearly shows that the CuDENPs had the best results across all the concentrations tested. This elucidates that the Cu clusters are indeed protected inside the PAMAM structure. As seen in the literature [128], dendrimers are generally used to improve the biocompatibility issues associated with toxic materials. Other controls such as the exposure of the HEK 293T cells to dendrimer alone and to CuNPs alone are needed, especially in the latter case, since it may be that copper occurs at such low concentrations within the Cu-DENPs that it would not affect the cytotoxicity.

Lastly, the prospect of the bioimaging properties of the C-Dots makes them attractive for biological applications. Thus, it was important to assess the cytotoxic effects of the C-Dots prepared in this study on HEK 293T cells. The data in **Fig. 52** (**yellow bars**) puts the C-Dots 80% threshold for low toxicity around 100µg/mL. Considering that C-Dots are generally used for bioimaging application at concentrations lower than 100µg/mL[215,216], these results demonstrate the potential of these materials for bioimaging.

This study is only a preliminary testing, a more appropriate analysis with proper controls was planned but was not possible for a lack of time.

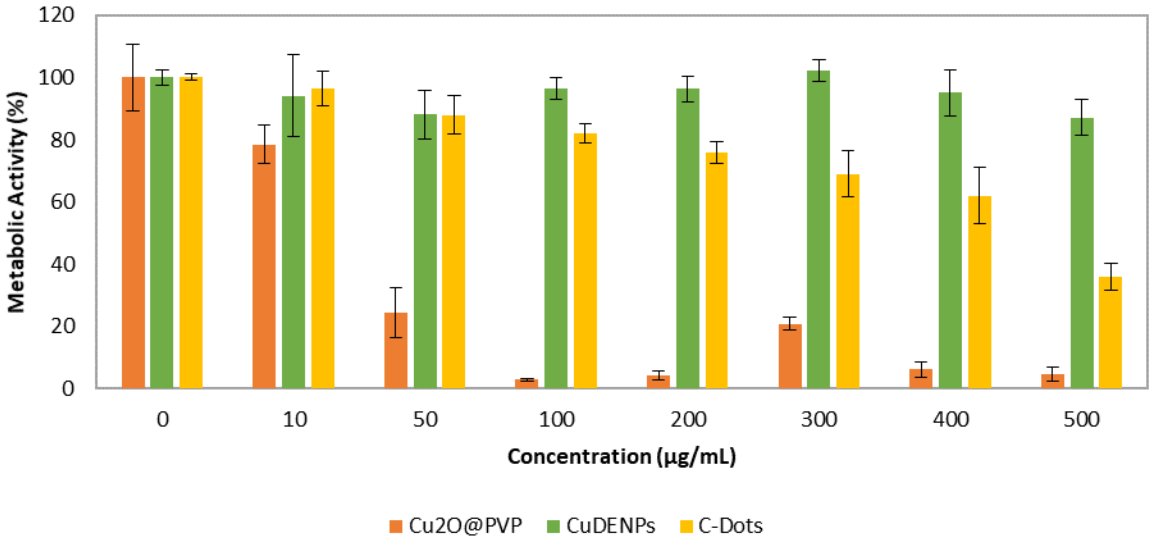

Fig. 52. Cell metabolic activity assessed by the MTT assay for the Cu_2O@PVP (in 0.5% DMSO), CuDENP (in water), C-Dots (in water) samples after 48h exposure. (Mean ± SD, N=3).

4 Conclusions

Different types of Cu-based particles were successfully synthesized using two distinct routes, although the Cu particles derived from the PVP route did not reach the desired nano-size (less than 100nm).

The crystal shape, the oxidation state, and to some extent the particle size could be tailored by changing the temperature and pH conditions when PVP was used as a capping agent. Room temperature conditions led to the formation of more amorphous structures, while at 60°C we managed to get disks and globular agglomerates, polyhedrons, and irregular spheres as we changed the pH from 2 to 5 to 7, respectively. Interestingly, at very acidic pH values there was a tendency for the formation of Cu species with a +2 oxidation state, passing through metallic copper at pH=5, while obtaining Cu^{+} at neutral pH. Generally, increasing the molar ratios of AA and PVP to Cu led to smaller and more homogeneous particles, especially in the case of the AA. Considering the tested conditions, the best parameters were at 10 AAeq and 8 NVPeq for pH=4, and 15 AAeq and 16 NVPeq for pH=7. Studies at higher ratios should be done to improve both size, size distribution, and yield.

Attempting to reproduce the works found in the literature for the synthesis of Cu-DENPs by chemical reduction with $NaBH_4$ led to the reversibility of the Cu clusters back to the ionic form. In an attempt to achieve satisfactory results, various modifications to the procedure were made (e.g. removing the dissolved oxygen from the solution to prevent oxidation) but they were ineffective. Replacing the reducing agent with AA yielded stable Cu-based NPs for several months, mainly because the unreacted AA still present in the solution prevented the metal from oxidizing. This new method has yet to be further optimized but it may be a good alternative to others that require hazardous reagents or solvents, as well as other conditions like high temperatures and specialized equipment.

The reactions involving the oxidation of AA to obtain metal-based particles currently explored in the literature may unknowingly have C-Dots in solution as an unexpected and unreported by-product. It is believed that the Cu ions may favor the formation of C-Dots. The presence of C-Dots was confirmed by the excitation-dependent emission of PL, as well as by TEM and XPS. The exact mechanism for the formation of the dots is unknown, but it should be associated with the dimerization of radical species coming from AA oxidation. Nevertheless, in terms of their PL properties, it is unknown if the C-Dots could compete with the fluorescence dyes already available on the market. Further studies are needed to better understand the optical properties of these particles, for instance, determine the quantum yield, and relate the surface groups with the emission bands.

In this work, the potential bioapplications of both the Cu-based particles and C-Dots were only explored by the preliminary evaluation of the cytotoxic effects of one of each type of particle. These tests were based on the MTT assay and only evaluated for the HEK 293T cell line.

Cu_2O@PVP expressed cell toxicity at concentrations of 50µg/mL and higher, which can be a problem in applications *in vivo.* Nevertheless, they may still be used for other biological applications involving, for instance, antimicrobial activity (not evaluated).

No significant cytotoxicity was detected for the Cu-DENPs for concentrations up to 500µg/mL, supporting the idea that the CuNPs were protected by the PAMAM dendrimer structure. This means that after verifying these results and further optimization, the next step in the scope of the bioapplications would be the creation of conjugates. For instance, the functionalization of the PAMAM end-groups with some targeting moieties like mannose. Moreover, there should be more available space for drug loading or conjugation which will add extra functionality.

In the case of the C-Dots, they start to present some cytotoxicity around the 100µg/mL concentrations. Considering that C-Dots are generally used for bioimaging application at concentrations lower than 100µg/mL[215,216], these results demonstrate the potential of these materials for bioimaging.

5 References

(1) Lewis, L. N. Chemical Catalysis by Colloids and Clusters. *Chem. Rev.* **1993**, *93*, 2693–2730. 10.1021/cr00024a006.

(2) Evano, G.; Blanchard, N.; Toumi, M. Copper-Mediated Coupling Reactions and Their Applications in Natural Products and Designed Biomolecules Synthesis. *Chem. Rev.* **2008**, *108*, 3054–3131. 10.1021/cr8002505.

(3) Baig, N.; Varma, R. Copper Modified Magnetic Bimetallic Nano-Catalysts Ligand Regulated Catalytic Activity. *Curr. Org. Chem.* **2013**, *17*, 2227–2237. 10.2174/13852728113179990045.

(4) Huang, H.; Huang, W.; Xu, Y.; Ye, X.; Wu, M.; Shao, Q.; Ou, G.; Peng, Z.; Shi, J.; Chen, J.; et al. Catalytic Oxidation of Gaseous Benzene with Ozone over Zeolite-Supported Metal Oxide Nanoparticles at Room Temperature. *Catal. Today* **2015**, *258*, 627–633. 10.1016/j.cattod.2015.01.006.

(5) Ahmed, A.; Elvati, P.; Violi, A. Size-and Phase-Dependent Structure of Copper(II) Oxide Nanoparticles. *RSC Adv.* **2015**, *5*, 35033–35041. 10.1039/c5ra04276c.

(6) Mondal, J.; Biswas, A.; Chiba, S.; Zhao, Y. Cu^0 Nanoparticles Deposited on Nanoporous Polymers: A Recyclable Heterogeneous Nanocatalyst for Ullmann Coupling of Aryl Halides with Amines in Water. *Sci. Rep.* **2015**, *5*, 8294. 10.1038/srep08294.

(7) Lu, Y. Z.; Wei, W. T.; Chen, W. Copper Nanoclusters: Synthesis, Characterization and Properties. *Chinese Sci. Bull.* **2012**, *57*, 41–47. 10.1007/s11434-011-4896-y.

(8) Din, M. I.; Rehan, R. Synthesis, Characterization, and Applications of Copper Nanoparticles. *Anal. Lett.* **2017**, *50*, 50–62. 10.1080/00032719.2016.1172081.

(9) Copper, Silver and Gold. In *Chemistry of the Elements*; Greenwood, N. N., Earnshaw, A., Eds.; Butterworth-Heinemann: Oxforad, U.K., 1997; pp 1173–1200. 10.1016/B978-0-7506-3365-9.50034-1.

(10) Gawande, M. B.; Goswami, A.; Felpin, F. X.; Asefa, T.; Huang, X.; Silva, R.; Zou, X.; Zboril, R.; Varma, R. S. Cu and Cu-Based Nanoparticles: Synthesis and Applications in Catalysis. *Chem. Rev.* **2016**, *116*, 3722–3811. 10.1021/acs.chemrev.5b00482.

(11) Yagi, S. Potential-PH Diagrams for Oxidation-State Control of Nanoparticles Synthesized via Chemical Reduction. In *Thermodynamics - Physical Chemistry of Aqueous Systems*; Piraján, J. C. M., Ed.; InTechOpen, 2011; pp 223–240. 10.5772/21548.

(12) Decan, M. R.; Impellizzeri, S.; Luisa Marin, M.; Scaiano, J. C. Copper Nanoparticle Heterogeneous Catalytic Click Cycloaddition Confirmed by Single-Molecule Spectroscopy. *Nat. Commun.* **2014**, *5*. 10.1038/ncomms5612.

(13) Shaygannia, A.; Rana, S.; Döhler, D.; Jirsa, F.; Meister, A.; Guadagno, L.; Koslowski, E.; Bron, M.; Binder, W. H. Carbon-Supported Copper Nanomaterials: Recyclable Catalysts for Huisgen [3+2] Cycloaddition Reactions. *Chem. - A Eur. J.* **2015**, *21*, 10763–10770. 10.1002/chem.201501217.

(14) Reymond, S.; Cossy, J. Copper-Catalyzed Diels−Alder Reactions. *Chem. Rev.* **2008**, *108*, 5359–5406. 10.1021/cr078346g.

(15) Ranu, B. C.; Saha, A.; Jana, R. Microwave-Assisted Simple and Efficient Ligand Free Copper Nanoparticle Catalyzed Aryl-Sulfur Bond Formation. *Adv. Synth. Catal.* **2007**, *349*, 2690–2696. 10.1002/adsc.200700289.

(16) Nasrollahzadeh, M.; Sajadi, S. M.; Rostami-Vartooni, A.; Bagherzadeh, M. Green Synthesis of Pd/CuO Nanoparticles by Theobroma Cacao L. Seeds Extract and Their Catalytic Performance for the Reduction of 4-Nitrophenol and Phosphine-Free Heck Coupling Reaction under Aerobic Conditions. *J. Colloid Interface Sci.* **2015**, *448*, 106–113. 10.1016/j.jcis.2015.02.009.

(17) Mitsudome, T.; Mikami, Y.; Ebata, K.; Mizugaki, T.; Jitsukawa, K.; Kaneda, K. Copper Nanoparticles on Hydrotalcite as a Heterogeneous Catalyst for Oxidant-Free Dehydrogenation of Alcohols. *Chem. Commun.* **2008**, *0*, 4804–4806. 10.1039/b809012b.

(18) Yoshida, K.; Gonzalez-Arellano, C.; Luque, R.; Gai, P. L. Efficient Hydrogenation of Carbonyl Compounds Using Low-Loaded Supported Copper Nanoparticles under Microwave Irradiation. *Appl. Catal. A Gen.* **2010**, *379*, 38–44. 10.1016/j.apcata.2010.02.028.

(19) Natesakhawat, S.; Lekse, J. W.; Baltrus, J. P.; Ohodnicki, P. R.; Howard, B. H.; Deng, X.; Matranga, C. Active Sites and Structure-Activity Relationships of Copper-Based Catalysts for Carbon Dioxide Hydrogenation to Methanol. *ACS Catal.* **2012**, *2*, 1667–1676. 10.1021/cs300008g.

(20) Tu, C. H.; Wang, A. Q.; Zheng, M. Y.; Wang, X. D.; Zhang, T. Factors Influencing the Catalytic Activity of SBA-15-Supported Copper Nanoparticles in CO Oxidation. *Appl. Catal. A Gen.* **2006**, *297*, 40–47. 10.1016/j.apcata.2005.08.035.

(21) Baik, J. H.; Yim, S. D.; Nam, I.-S.; Mok, Y. S.; Lee, J.-H.; Cho, B. K.; Oh, S. H. Control of NO x Emissions from Diesel Engine by Selective Catalytic Reduction (SCR) with Urea. *Top. Catal.* **2004**, *30*, 37–41. 10.1023/B:TOCA.0000029725.88068.97.

(22) Chen, C. S.; Lin, J. H.; Lai, T. W.; Li, B. H. Active Sites on Cu/SiO2 Prepared Using the Atomic Layer Epitaxy Technique for a Low-Temperature Water-Gas Shift Reaction. *J. Catal.* **2009**, *263*, 155–166. 10.1016/j.jcat.2009.02.004.

(23) Foo, W. J.; Zhang, C.; Ho, G. W. Non-Noble Metal Cu-Loaded TiO_2 for Enhanced Photocatalytic H_2 Production. *Nanoscale* **2013**, *5*, 759–764. 10.1039/C2NR33004K.

(24) Sun, S.; Song, X.; Sun, Y.; Deng, D.; Yang, Z. The Crystal-Facet-Dependent Effect of Polyhedral Cu_2O Microcrystals on Photocatalytic Activity. *Catal. Sci. Technol.* **2012**, *2*, 925–930. 10.1039/c2cy00530a.

(25) Huang, Z.; Cui, F.; Kang, H.; Chen, J.; Zhang, X.; Xia, C. Highly Dispersed Silica-Supported Copper Nanoparticles Prepared by Precipitation-Gel Method: A Simple but Efficient and Stable Catalyst for Glycerol Hydrogenolysis. *Chem. Mater.* **2008**, *20*, 5090–5099. 10.1021/cm8006233.

(26) Cheng, N.; Xue, Y.; Liu, Q.; Tian, J.; Zhang, L.; Asiri, A. M.; Sun, X. Cu/($Cu(OH)_2$-CuO) Core/Shell Nanorods Array: In-Situ Growth and Application as an Efficient 3D Oxygen Evolution Anode. *Electrochim. Acta* **2015**, *163*, 102–106. 10.1016/j.electacta.2015.02.099.

(27) Meyer, B. K.; Polity, A.; Reppin, D.; Becker, M.; Hering, P.; Kramm, B.; Klar, P. J.; Sander, T.; Reindl, C.; Heiliger, C.; et al. The Physics of Copper Oxide (Cu_2O). In *Semiconductors and Semimetals*; 2013; Vol. 88, pp 201–226. 10.1016/B978-0-12-396489-2.00006-0.

(28) Meyer, B. K.; Polity, A.; Reppin, D.; Becker, M.; Hering, P.; Klar, P. J.; Sander, T.; Reindl, C.; Benz, J.; Eickhoff, M.; et al. Binary Copper Oxide Semiconductors: From Materials towards Devices. *Phys. Status Solidi* **2012**, *249*, 1487–1509. 10.1002/pssb.201248128.

(29) Musa, A. O.; Akomolafe, T.; Carter, M. J. Production of Cuprous Oxide, a Solar Cell Material, by Thermal Oxidation and a Study of Its Physical and Electrical Properties. *Sol. Energy Mater. Sol. Cells* **1998**, *51*, 305–316. 10.1016/S0927-0248(97)00233-X.

(30) Poizot, P.; Laruelle, S.; Grugeon, S.; Dupont, L.; Tarascon, J. M. Nano-Sized Transition-Metal Oxides as Negative-Electrode Materials for Lithium-Ion Batteries. *Nature* **2000**, *407*, 496–499. 10.1038/35035045.

(31) Chen, L.; Zhang, Y.; Zhu, P.; Zhou, F.; Zeng, W.; Lu, D. D.; Sun, R.; Wong, C. Copper Salts Mediated Morphological Transformation of Cu_2O from Cubes to Hierarchical Flower-like or Microspheres and Their Supercapacitors Performances. *Sci. Rep.* **2015**, *5*, 9672. 10.1038/srep09672.

(32) Zhang, J.; Liu, J.; Peng, Q.; Wang, X.; Li, Y. Nearly Monodisperse Cu_2O and CuO Nanospheres: Preparation and Applications for Sensitive Gas Sensors. *Chem. Mater.* **2006**, *18*, 867–871. 10.1021/cm052256f.

(33) De Jongh, P. E.; Vanmaekelbergh, D.; Kelly, J. J. Cu_2O: A Catalyst for the Photochemical Decomposition of Water? *Chem. Commun.* **1999**, *0*, 1069–1070. 10.1039/a901232j.

(34) Hara, M.; Kondo, T.; Komoda, M.; Ikeda, S.; Kondo, J. N.; Domen, K.; Hara, M.; Shinohara, K.; Tanaka, A. Cu_2O as a Photocatalyst for Overall Water Splitting under Visible Light Irradiation. *Chem. Commun.* **1998**, *2*, 357–358. 10.1039/a707440i.

(35) Gao, D.; Zhang, J.; Zhu, J.; Qi, J.; Zhang, Z.; Sui, W.; Shi, H.; Xue, D. Vacancy-Mediated Magnetism in Pure Copper Oxide Nanoparticles. *Nanoscale Res. Lett.* **2010**, *5*, 769–772. 10.1007/s11671-010-9555-8.

(36) Anandakumar, B. S.; Reddy, M. B. M.; Tharamani, C. N.; Pasha, M. A.; Chandrappa, G. T. Combustion-Derived CuO Nanoparticles: An Effective and Environmentally Benign Catalyst in the Synthesis of Aromatic Nitriles from Aromatic Aldehydes. *Chinese J. Catal.* **2013**, *34*, 704–710. 10.1016/S1872-2067(11)60503-2.

(37) Reddy, K. J.; McDonald, K. J.; King, H. A Novel Arsenic Removal Process for Water Using Cupric Oxide Nanoparticles. *J. Colloid Interface Sci.* **2013**, *397*, 96–102. 10.1016/j.jcis.2013.01.041.

(38) Zaera, F. Nanostructured Materials for Applications in Heterogeneous Catalysis. *Chem. Soc. Rev.* **2013**, *42*, 2746–2762. 10.1039/C2CS35261C.

(39) Zhao, M.; Sun, L.; Crooks, R. M. Preparation of Cu Nanoclusters within Dendrimer Templates. *J. Am. Chem. Soc.* **1998**, *120*, 4877–4878. 10.1021/ja980438n.

(40) Sampath, M.; Vijayan, R.; Tamilarasu, E.; Tamilselvan, A.; Sengottuvelan, B. Green Synthesis of Novel Jasmine Bud-Shaped Copper Nanoparticles. *J. Nanotechnol.* **2014**, *2014*, 1–7. 10.1155/2014/626523.

(41) Crooks, R. M.; Lemon, B. I.; Sun, L.; Yeung, L. K.; Zhao, M. Dendrimer-Encapsulated Metals and Semiconductors: Synthesis, Characterization, and Applications. In *Dendrimers III: Design, Dimension, Function*; Vögtle, F., Ed.; Springer Berlin Heidelberg: Berlin, Heidelberg, 2001; Vol. 212, pp 81–135. 10.1007/3-540-44924-8_3.

(42) Chen, P. C.; Li, Y. C.; Ma, J. Y.; Huang, J. Y.; Chen, C. F.; Chang, H. T. Size-Tunable Copper Nanocluster Aggregates and Their Application in Hydrogen Sulfide Sensing on Paper-Based Devices. *Sci. Rep.* **2016**, *6*. 10.1038/srep24882.

(43) Rao, H.; Ge, H.; Lu, Z.; Liu, W.; Chen, Z.; Zhang, Z.; Wang, X.; Zou, P.; Wang, Y.; He, H.; et al. Copper Nanoclusters as an On-off-on Fluorescent Probe for Ascorbic Acid. *Microchim. Acta* **2016**, *183*, 1651–1657. 10.1007/s00604-016-1794-7.

(44) Guo, Y.; Cao, F.; Lei, X.; Mang, L.; Cheng, S.; Song, J. Fluorescent Copper Nanoparticles: Recent Advances in Synthesis and Applications for Sensing Metal Ions. *Nanoscale* **2016**, *8*, 4852–4863. 10.1039/c6nr00145a.

(45) Cao, H.; Chen, Z.; Zheng, H.; Huang, Y. Copper Nanoclusters as a Highly Sensitive and Selective Fluorescence Sensor for Ferric Ions in Serum and Living Cells by Imaging. *Biosens. Bioelectron.* **2014**, *62*, 189–195. https:/doi.org/10.1016/j.bios.2014.06.049.

(46) Das, N. K.; Ghosh, S.; Priya, A.; Datta, S.; Mukherjee, S. Luminescent Copper Nanoclusters as a Specific Cell-Imaging Probe and a Selective Metal Ion Sensor. *J. Phys. Chem. C* **2015**, *119*, 24657–24664. 10.1021/acs.jpcc.5b08123.

(47) Zhang, L.; Wang, E. Metal Nanoclusters: New Fluorescent Probes for Sensors and Bioimaging. *Nano Today* **2014**, *9*, 132–157. 10.1016/j.nantod.2014.02.010.

(48) Ghosh, S.; Das, N. K.; Anand, U.; Mukherjee, S. Photostable Copper Nanoclusters: Compatible Förster Resonance Energy-Transfer Assays and a Nanothermometer. *J. Phys. Chem. Lett.* **2015**, *6*, 1293–1298. 10.1021/acs.jpclett.5b00378.

(49) Ghosh, R.; Goswami, U.; Ghosh, S. S.; Paul, A.; Chattopadhyay, A. Synergistic Anticancer Activity of Fluorescent Copper Nanoclusters and Cisplatin Delivered through a Hydrogel Nanocarrier. *ACS Appl. Mater. Interfaces* **2015**, *7*, 209–222. 10.1021/am505799q.

(50) Li, J.; Zhu, J.-J.; Xu, K. Fluorescent Metal Nanoclusters: From Synthesis to Applications. *TrAC Trends Anal. Chem.* **2014**, *58*, 90–98. 10.1016/j.trac.2014.02.011.

(51) Ghosh, R.; Sahoo, A. K.; Ghosh, S. S.; Paul, A.; Chattopadhyay, A. Blue-Emitting Copper Nanoclusters Synthesized in the Presence of Lysozyme as Candidates for Cell Labeling. *ACS Appl. Mater. Interfaces* **2014**, *6*, 3822–3828. 10.1021/am500040t.

(52) Athanassiou, E. K.; Grass, R. N.; Stark, W. J. Large-Scale Production of Carbon-Coated Copper Nanoparticles for Sensor Applications. *Nanotechnology* **2006**, *17*, 1668–1673. 10.1088/0957-4484/17/6/022.

(53) Tan, Y.; Xue, X.; Peng, Q.; Zhao, H.; Wang, T.; Li, Y. Controllable Fabrication and Electrical Performance of Single Crystalline Cu_2O Nanowires with High Aspect Ratios. *Nano Lett.* **2007**, *7*, 3723–3728. 10.1021/nl0721259.

(54) Park, B. K.; Kim, D.; Jeong, S.; Moon, J.; Kim, J. S. Direct Writing of Copper Conductive Patterns by Ink-Jet Printing. *Thin Solid Films* **2007**, *515*, 7706–7711. 10.1016/j.tsf.2006.11.142.

(55) Hokita, Y.; Kanzaki, M.; Sugiyama, T.; Arakawa, R.; Kawasaki, H. High-Concentration Synthesis of Sub-10-Nm Copper Nanoparticles for Application to Conductive Nanoinks. *ACS Appl. Mater. Interfaces* **2015**, *7*, 19382–19389. 10.1021/acsami.5b05542.

(56) Sreeprasad, T. S.; Pradeep, T. Noble Metal Nanoparticles. In *Springer Handbook of Nanomaterials*; Springer Berlin Heidelberg: Berlin, Heidelberg, 2013; pp 303–388. 10.1007/978-3-642-20595-8_9.

(57) Ruparelia, J. P.; Chatterjee, A. K.; Duttagupta, S. P.; Mukherji, S. Strain Specificity in Antimicrobial Activity of Silver and Copper Nanoparticles. *Acta Biomater.* **2008**, *4*, 707–716. 10.1016/j.actbio.2007.11.006.

(58) Cioffi, N.; Torsi, L.; Ditaranto, N.; Tantillo, G.; Ghibelli, L.; Sabbatini, L.; Bleve-Zacheo, T.; D'Alessio, M.; Zambonin, P. G.; Traversa, E. Copper Nanoparticle/Polymer Composites with Antifungal and Bacteriostatic Properties. *Chem. Mater.* **2005**, *17*, 5255–5262. 10.1021/cm0505244.

(59) Esteban-Cubillo, A.; Pecharromán, C.; Aguilar, E.; Santarén, J.; Moya, J. S. Antibacterial Activity of Copper Monodispersed Nanoparticles into Sepiolite. *J. Mater. Sci.* **2006**, *41*, 5208–5212. 10.1007/s10853-006-0432-x.

(60) Wang, Y.; Zi, X.-Y.; Su, J.; Zhang, H.-X.; Zhang, X.-R.; Zhu, H.-Y.; Li, J.-X.; Yin, M.; Yang, F.; Hu, Y.-P. Cuprous Oxide Nanoparticles Selectively Induce Apoptosis of Tumor Cells. *Int. J. Nanomedicine* **2012**, *7*, 2641–2652. 10.2147/IJN.S31133.

(61) Chakraborty, I.; Pradeep, T. Atomically Precise Clusters of Noble Metals: Emerging Link between Atoms and Nanoparticles. *Chem. Rev.* **2017**, *117*, 8208–8271. 10.1021/acs.chemrev.6b00769.

(62) Yoon, K. Y.; Hoon Byeon, J.; Park, J. H.; Hwang, J. Susceptibility Constants of Escherichia Coli and Bacillus Subtilis to Silver and Copper Nanoparticles. *Sci. Total Environ.* **2007**, *373*, 572–575. 10.1016/j.scitotenv.2006.11.007.

(63) Hong, X.; Wang, G.; Zhu, W.; Shen, X.; Wang, Y. Synthesis of Sub-10 nm Cu_2O Nanowires by Poly(Vinyl Pyrrolidone)-Assisted Electrodeposition. *J. Phys. Chem. C* **2009**, *113*, 14172–14175. 10.1021/jp9039786.

(64) Siegfried, M. J.; Choi, K. S. Electrochemical Crystallization of Cuprous Oxide with Systematic Shape Evolution. *Adv. Mater.* **2004**, *16*, 1743–1746. 10.1002/adma.200400177.

(65) Siegfried, M. J.; Choi, K. S. Elucidating the Effect of Additives on the Growth and Stability of Cu_2O Surfaces via Shape Transformation of Pre-Grown Crystals. *J. Am. Chem. Soc.* **2006**, *128*, 10356–10357. 10.1021/ja063574y.

(66) Sastry, A. B. S.; Karthik Aamanchi, R. B.; Sree Rama Linga Prasad, C.; Murty, B. S. Large-Scale Green Synthesis of Cu Nanoparticles. *Environ. Chem. Lett.* **2013**, *11*, 183–187. 10.1007/s10311-012-0395-x.

(67) Joshi, S. S.; Patil, S. F.; Iyer, V.; Mahumuni, S. Radiation Induced Synthesis and Characterization of Copper Nanoparticles. *Nanostructured Mater.* **1998**, *10*, 1135–1144. 10.1016/S0965-9773(98)00153-6.

(68) Zhao, X.; Bao, Z.; Sun, C.; Xue, D. Polymorphology Formation of Cu2O: A Microscopic Understanding of Single Crystal Growth from Both Thermodynamic and Kinetic Models. *J. Cryst. Growth* **2009**, *311*, 711–715. 10.1016/j.jcrysgro.2008.09.081.

(69) Yeh, Y.-H.; Yeh, M.-S.; Lee, Y.-P.; Yeh, C.-S. Formation of Cu Nanoparticles from CuO Powder by Laser Ablation in 2-Propanol. *Chem. Lett.* **1998**, *27*, 1183–1184. 10.1246/cl.1998.1183.

(70) Kshirsagar, J.; Shrivastava, R.; Adwani, P. Preparation and Characterization of Copper Oxide Nanoparticles and Determination of Enhancement in Critical Heat Flux. *Therm. Sci.* **2017**, *21*, 233–242. 10.2298/TSCI140619026K.

(71) Rahimi-Nasrabadi, M.; Pourmortazavi, S. M.; Davoudi-Dehaghani, A. A.; Hajimirsadeghi, S. S.; Zahedi, M. M. Synthesis and Characterization of Copper Oxalate and Copper Oxide Nanoparticles by Statistically Optimized Controlled Precipitation and Calcination of Precursor. *Cryst. Eng. Comm.* **2013**, *15*, 4077–4086. 10.1039/c3ce26930b.

(72) Kim, Y. H.; Lee, D. K.; Jo, B. G.; Jeong, J. H.; Kang, Y. S. Synthesis of Oleate Capped Cu Nanoparticles by Thermal Decomposition. *Colloids Surfaces A Physicochem. Eng. Asp.* **2006**, *284–285*, 364–368. 10.1016/j.colsurfa.2005.10.067.

(73) Hambrock, J.; Becker, R.; Birkner, A.; Weiß, J.; Fischer, R. A. A Non-Aqueous Organometallic Route to Highly Monodispersed Copper Nanoparticles Using [Cu(OCH(Me)CH2NMe2)2]. *Chem. Commun.* **2002**, *2*, 68–69. 10.1039/b108797e.

(74) Sui, Y.; Fu, W.; Yang, H.; Zeng, Y.; Zhang, Y.; Zhao, Q.; Li, Y.; Zhou, X.; Leng, Y.; Li, M.; et al. Low Temperature Synthesis of Cu_2O Crystals: Shape Evolution and Growth Mechanism. *Cryst. Growth Des.* **2010**, *10*, 99–108. 10.1021/cg900437x.

(75) Alzahrani, E.; Ahmed, R. A. Synthesis of Copper Nanoparticles with Various Sizes and Shapes: Application as a Superior Non-Enzymatic Sensor and Antibacterial Agent. *Int. J. Electrochem. Sci.* **2016**, *11*, 4712–4723. 10.20964/2016.06.83.

(76) Haas, I.; Shanmugam, S.; Gedanken, A. Pulsed Sonoelectrochemical Synthesis of Size-Controlled Copper Nanoparticles Stabilized by Poly(N-Vinylpyrrolidone). *J. Phys. Chem. B* **2006**, *110*, 16947–16952. 10.1021/jp064216k.

(77) Ponce, A. A.; Klabunde, K. J. Chemical and Catalytic Activity of Copper Nanoparticles Prepared via Metal Vapor Synthesis. *J. Mol. Catal. A Chem.* **2005**, *225*, 1–6. 10.1016/j.molcata.2004.08.019.

(78) Wu, S. H.; Chen, D. H. Synthesis of High-Concentration Cu Nanoparticles in Aqueous CTAB Solutions. *J. Colloid Interface Sci.* **2004**, *273*, 165–169. 10.1016/j.jcis.2004.01.071.

(79) Ben Aissa, M. A.; Tremblay, B.; Andrieux-Ledier, A.; Maisonhaute, E.; Raouafi, N.; Courty, A. Copper Nanoparticles of Well-Controlled Size and Shape: A New Advance in Synthesis and Self-Organization. *Nanoscale* **2015**, *7*, 3189–3195. 10.1039/C4NR06893A.

(80) Gou, L.; Murphy, C. J. Controlling the Size of Cu_2O Nanocubes from 200 to 25 nm. *J. Mater. Chem.* **2004**, *14*, 735–738. 10.1039/b311625e.

(81) Vázquez-Vázquez, C.; Bañobre-López, M.; Mitra, A.; López-Quintela, M. A.; Rivas, J. Synthesis of Small Atomic Copper Clusters in Microemulsions. *Langmuir* **2009**, *25*, 8208–8216. 10.1021/la900100w.

(82) Suramwar, N. V.; Thakare, S. R.; Khaty, N. T. One Pot Synthesis of Copper Nanoparticles at Room Temperature and Its Catalytic Activity. *Arab. J. Chem.* **2016**, *9*, S1807–S1812. 10.1016/j.arabjc.2012.04.034.

(83) Liu, K.; Song, Y.; Chen, S. Electrocatalytic Activities of Alkyne-Functionalized Copper Nanoparticles in Oxygen Reduction in Alkaline Media. *J. Power Sources* **2014**, *268*, 469–475. 10.1016/j.jpowsour.2014.06.054.

(84) Wei, W.; Lu, Y.; Chen, W.; Chen, S. One-Pot Synthesis, Photoluminescence, and Electrocatalytic Properties of Subnanometer-Sized Copper Clusters. *J. Am. Chem. Soc.* **2011**, *133*, 2060–2063. 10.1021/ja109303z.

(85) Abdulla-Al-Mamun, M.; Kusumoto, Y.; Muruganandham, M. Simple New Synthesis of Copper Nanoparticles in Water/Acetonitrile Mixed Solvent and Their Characterization. *Mater. Lett.* **2009**, *63*, 2007–2009. 10.1016/j.matlet.2009.06.037.

(86) Ang, T. P.; Wee, T. S. A.; Chin, W. S. Three-Dimensional Self-Assembled Monolayer (3D SAM) of n-Alkanethiols on Copper Nanoclusters. *J. Phys. Chem. B* **2004**, *108*, 11001–11010. 10.1021/jp049006r.

(87) Chen, L.; Zhang, D.; Chen, J.; Zhou, H.; Wan, H. The Use of CTAB to Control the Size of Copper Nanoparticles and the Concentration of Alkylthiols on Their Surfaces. *Mater. Sci. Eng. A* **2006**, *415*, 156–161. 10.1016/j.msea.2005.09.060.

(88) Grouchko, M.; Kamyshny, A.; Magdassi, S. Formation of Air-Stable Copper-Silver Core-Shell Nanoparticles for Inkjet Printing. *J. Mater. Chem.* **2009**, *19*, 3057–3062. 10.1039/b821327e.

(89) Khanna, P. K.; Gaikwad, S.; Adhyapak, P. V.; Singh, N.; Marimuthu, R. Synthesis and Characterization of Copper Nanoparticles. *Mater. Lett.* **2007**, *61*, 4711–4714. 10.1016/j.matlet.2007.03.014.

(90) Khanna, P. K.; More, P.; Jawalkar, J.; Patil, Y.; Koteswar Rao, N. Synthesis of Hydrophilic Copper Nanoparticles: Effect of Reaction Temperature. *J. Nanoparticle Res.* **2009**, *11*, 793–799. 10.1007/s11051-008-9441-9.

(91) Athawale, A. A.; Katre, P. P.; Kumar, M.; Majumdar, M. B. Synthesis of CTAB-IPA Reduced Copper Nanoparticles. *Mater. Chem. Phys.* **2005**, *91*, 507–512. 10.1016/j.matchemphys.2004.12.017.

(92) Chandra, S.; Kumar, A.; Tomar, P. K. Synthesis and Characterization of Copper Nanoparticles by Reducing Agent. *J. Saudi Chem. Soc.* **2014**, *18*, 149–153. 10.1016/j.jscs.2011.06.009.

(93) Qiao, S.; Fan, B.; Yang, Y.; Liu, N.; Huang, H.; Liu, Y. Copper Nanoparticle/Carbon Quantum Dots Hybrid as Green Photocatalyst for High-Efficiency Oxidation of Cyclohexane. *RSC Adv.* **2015**, *5*, 43058–43064. 10.1039/c5ra04753f.

(94) Hu, R.; Liu, Y. R.; Kong, R. M.; Donovan, M. J.; Zhang, X. B.; Tan, W.; Shen, G. L.; Yu, R. Q. Double-Strand DNA-Templated Formation of Copper Nanoparticles as Fluorescent Probe for Label Free Nuclease Enzyme Detection. *Biosens. Bioelectron.* **2013**, *42*, 31–35. 10.1016/j.bios.2012.10.037.

(95) Shang, Y.; Zhang, D.; Guo, L. CuCl-Intermediated Construction of Short-Range-Ordered Cu2O Mesoporous Spheres with Excellent Adsorption Performance. *J. Mater. Chem.* **2012**, *22*, 856–861. 10.1039/c1jm14258e.

(96) Xu, H.; Wang, W.; Zhu, W. Shape Evolution and Size-Controllable Synthesis of Cu_2O Octahedra and Their Morphology-Dependent Photocatalytic Properties. *J. Phys. Chem. B* **2006**, *110*, 13829–13834. 10.1021/jp061934y.

(97) Chen, K.; Xue, D. Chemoaffinity-Mediated Crystallization of Cu_2O: A Reaction Effect on Crystal Growth and Anode Property. *Cryst. Eng. Comm.* **2013**, *15*, 1739–1746. 10.1039/c2ce26500a.

(98) Kaur, R.; Giordano, C.; Gradzielski, M.; Mehta, S. K. Synthesis of Highly Stable, Water-Dispersible Copper Nanoparticles as Catalysts for Nitrobenzene Reduction. *Chem. - An Asian J.* **2014**, *9*, 189–198. 10.1002/asia.201300809.

(99) Zhang, Z.; Che, H.; Gao, J.; Wang, Y.; She, X.; Sun, J.; Gunawan, P.; Zhong, Z.; Su, F. Shape-Controlled Synthesis of Cu2O Microparticles and Their Catalytic Performances in the Rochow Reaction. *Catal. Sci. Technol.* **2012**, *2*, 1207–1212. 10.1039/c2cy20070h.

(100) Liang, X.; Gao, L.; Yang, S.; Sun, J. Facile Synthesis and Shape Evolution of Single-Crystal Cuprous Oxide. *Adv. Mater.* **2009**, *21*, 2068–2071. 10.1002/adma.200802783.

(101) Kesharwani, P.; Jain, K.; Jain, N. K. Dendrimer as Nanocarrier for Drug Delivery. *Prog. Polym. Sci.* **2014**, *39*, 268–307. 10.1016/j.progpolymsci.2013.07.005.

(102) Yu, W.; Xie, H.; Chen, L.; Li, Y.; Zhang, C. Synthesis and Characterization of Monodispersed Copper Colloids in Polar Solvents. *Nanoscale Res. Lett.* **2009**, *4*, 465–470. 10.1007/s11671-009-9264-3.

(103) Li, Y.; Tang, X.; Zhang, Y.; Li, J.; Lv, C.; Meng, X.; Huang, Y.; Hang, C.; Wang, C. Cu Nanoparticles of Low Polydispersity Synthesized by a Double-Template Method and Their Stability. *Colloid Polym. Sci.* **2014**, *292*, 715–722. 10.1007/s00396-013-3123-6.

(104) Li, Q.; Xu, P.; Zhang, B.; Tsai, H.; Zheng, S.; Wu, G.; Wang, H. L. Structure-Dependent Electrocatalytic Properties of Cu_2O Nanocrystals for Oxygen Reduction Reaction. *J. Phys. Chem. C* **2013**, *117*, 13872–13878. 10.1021/jp403655y.

(105) Luo, H.; Zhou, J.; Zhong, H.; Zhou, L.; Jia, Z.; Tan, X. Polyhedron Cu_2O@Ag Composite Microstructures: Synthesis, Mechanism Analysis and Structure-Dependent SERS Properties. *RSC Adv.* **2016**, *6*, 99105–99113. 10.1039/c6ra20856h.

(106) Wu, S.; Liu, T.; Zeng, W.; He, J.; Yu, W.; Gou, Z. Rose-like Cu_2O Synthesized by Assisted PVP K30 Hydrothermal Method. *J. Mater. Sci. Mater. Electron.* **2013**, *24*, 2404–2409. 10.1007/s10854-013-1109-2.

(107) Wang, Z.; Susha, A. S.; Chen, B.; Reckmeier, C.; Tomanec, O.; Zboril, R.; Zhong, H.; Rogach, A. L. Poly(Vinylpyrrolidone) Supported Copper Nanoclusters: Glutathione Enhanced Blue Photoluminescence for Application in Phosphor Converted Light Emitting Devices. *Nanoscale* **2016**, *8*, 7197–7202. 10.1039/c6nr00806b.

(108) Jiang, J.; Kim, S.-H.; Piao, L. The Facile Synthesis of Cu@SiO_2 Yolk–shell Nanoparticles via a Disproportionation Reaction of Silica-Encapsulated Cu 2 O Nanoparticle Aggregates. *Nanoscale* **2015**, *7*, 8299–8303. 10.1039/C5NR01484K.

(109) Oseghale, C. I.; Abdalla, A. H.; Posada, J. O. G.; Hall, P. J. A New Synthesis Route for Sustainable Gold Copper Utilization in Direct Formic Acid Fuel Cells. *Int. J. Hydrogen Energy* **2016**, *41*, 16394–16401. 10.1016/j.ijhydene.2016.05.204.

(110) Liu, Q. M.; Yasunami, T.; Kuruda, K.; Okido, M. Preparation of Cu Nanoparticles with Ascorbic Acid by Aqueous Solution Reduction Method. *Trans. Nonferrous Met. Soc. China (English Ed.* **2012**, *22*, 2198–2203. 10.1016/S1003-6326(11)61449-0.

(111) Huang, L.; Peng, F.; Yu, H.; Wang, H. Synthesis of Cu_2O Nanoboxes, Nanocubes and Nanospheres by Polyol Process and Their Adsorption Characteristic. *Mater. Res. Bull.* **2008**, *43*, 3047–3053. 10.1016/j.materresbull.2007.11.011.

(112) Nemanashi, M.; Meijboom, R. Synthesis and Characterization of Cu, Ag and Au Dendrimer-Encapsulated Nanoparticles and Their Application in the Reduction of 4-Nitrophenol to 4-Aminophenol. *J. Colloid Interface Sci.* **2013**, *389*, 260–267. 10.1016/j.jcis.2012.09.012.

(113) Scott, R. W. J.; Wilson, O. M.; Crooks, R. M. Synthesis, Characterization, and Applications of Dendrimer-Encapsulated Nanoparticles. *J. Phys. Chem. B* **2005**, *109*, 692–704. 10.1021/jp0469665.

(114) Crooks, R. M.; Zhao, M.; Sun, L.; Chechik, V.; Yeung, L. K. Dendrimer-Encapsulated Metal Nanoparticles: Synthesis, Characterization, and Applications to Catalysis. *Acc. Chem. Res.* **2001**, *34*, 181–190. 10.1021/ar000110a.

(115) Tran, M. L.; Zvyagin, A. V.; Plakhotnik, T. Synthesis and Spectroscopic Observation of Dendrimer-Encapsulated Gold Nanoclusters. *Chem. Commun.* **2006**, *0*, 2400. 10.1039/b602079h.

(116) Esumi, K.; Torigoe, K. Preparation and Characterization of Noble Metal Nanoparticles Using Dendrimers as Protective Colloids. In *Adsorption and Nanostructure*; Springer Berlin Heidelberg: Berlin, Heidelberg, 2001; Vol. 117, pp 80–87. 10.1007/3-540-45405-5_15.

(117) Zhao, M.; Crooks, R. M. Intradendrimer Exchange of Metal Nanoparticles. *Chem. Mater.* **1999**, *11*, 3379–3385. 10.1021/cm990435p.

(118) Buhleier, E.; Wehner, W.; Vögtle, F. "Cascade"- and "Nonskid-Chain-like" Syntheses of Molecular Cavity Topologies. *Synthesis (Stuttg).* **1978**, *1978*, 155–158. 10.1055/s-1978-24702.

(119) Tomalia, D. A.; Baker, H.; Dewald, J.; Hall, M.; Kallos, G.; Martin, S.; Roeck, J.; Ryder, J.; Smith, P. A New Class of Polymers: Starburst-Dendritic Macromolecules. *Polym. J.* **1985**, *17*, 117–132. 10.1295/polymj.17.117.

(120) Watkins, D. M.; Sayed-Sweet, Y.; Klimash, J. W.; Turro, N. J.; Tomalia, D. A. Dendrimers with Hydrophobic Cores and the Formation of Supramolecular Dendrimer–Surfactant Assemblies. *Langmuir* **1997**, *13*, 3136–3141. 10.1021/la9620263.

(121) Hawker, C. J.; Fréchet, J. M. J. Preparation of Polymers with Controlled Molecular Architecture. A New Convergent Approach to Dendritic Macromolecules. *J. Am. Chem. Soc.* **1990**, *112*, 7638–7647. 10.1021/ja00177a027.

(122) Zeng, F.; Zimmerman, S. C. Dendrimers in Supramolecular Chemistry: From Molecular Recognition to Self-Assembly. *Chem. Rev.* **1997**, *97*, 1681–1712. 10.1021/cr9603892.

(123) Feng, Z. V.; Lyon, J. L.; Croley, J. S.; Crooks, R. M.; Vanden Bout, D. A.; Stevenson, K. J. Synthesis and Catalytic Evaluation of Dendrimer-Encapsulated Cu Nanoparticles. An Undergraduate Expirement Catalytic Nanomaterials. *J. Chem. Educ.* **2009**, *86*, 368–372. 10.1021/ed086p368.

(124) Abbasi, E.; Aval, S. F.; Akbarzadeh, A.; Milani, M.; Nasrabadi, H. T.; Joo, S. W.; Hanifehpour, Y.; Nejati-Koshki, K.; Pashaei-Asl, R. Dendrimers: Synthesis, Applications, and Properties. *Nanoscale Res. Lett.* **2014**, *9*, 1–10. 10.1186/1556-276X-9-247.

(125) Baig, T.; Nayak, J.; Dwivedi, V.; Singh, A.; Tripathi, P. K. A Review about Dendrimers : Synthesis , Types , Characterization and Applications. *Int. J. Adv. Pharmacy, Biol. Chem.* **2015**, *4*, 44–59. http://www.ijapbc.com/files/07-4105.pdf.

(126) Mignani, S.; Rodrigues, J.; Tomas, H.; Caminade, A.-M.; Laurent, R.; Shi, X.; Majoral, J.-P. Recent Therapeutic Applications of the Theranostic Principle with Dendrimers in Oncology. *Sci. China Mater.* **2018**, *61*, 1367–1386. 10.1007/s40843-018-9244-5.

(127) Vögtle, F.; Richardt, G.; Werner, N. Types of Dendrimers and Their Syntheses. In *Dendrimer Chemistry*; Wiley-Blackwell, 2009; pp 81–167. 10.1002/9783527626953.ch4.

(128) Malik, N.; Wiwattanapatapee, R.; Klopsch, R.; Lorenz, K.; Frey, H.; Weener, J. W.; Meijer, E. W.; Paulus, W.; Duncan, R. Dendrimers: Relationship between Structure and Biocompatibility in Vitro, and Preliminary Studies on the Biodistribution of 125I-Labelled Polyamidoamine Dendrimers in Vivo. *J. Control. Release* **2000**, *65*, 133–148. 10.1016/S0168-3659(99)00246-1.

(129) Jevprasesphant, R.; Penny, J.; Jalal, R.; Attwood, D.; McKeown, N. B.; D'Emanuele, A. The Influence of Surface Modification on the Cytotoxicity of PAMAM Dendrimers. *Int. J. Pharm.* **2003**, *252*, 263–266. 10.1016/S0378-5173(02)00623-3.

(130) Tran, M. L.; Gahan, L. R.; Gentle, I. R. Structural Studies of Copper(II)-Amine Terminated Dendrimer Complexes by EXAFS. *J. Phys. Chem. B* **2004**, *108*, 20130–20136. 10.1021/jp037569h.

(131) Shakhbazau, A.; Isayenka, I.; Kartel, N.; Goncharova, N.; Seviaryn, I.; Kosmacheva, S.; Potapnev, M.; Shcharbin, D.; Bryszewska, M. Transfection Efficiencies of PAMAM Dendrimers Correlate Inversely with Their Hydrophobicity. *Int. J. Pharm.* **2010**, *383*, 228–235. 10.1016/j.ijpharm.2009.09.020.

(132) Nishikawa, Y.; Toyoshima, Y.; Kurata, T. Identification of 3,4-Dihydroxy-2-Oxo-Butanal (L-Threosone) as an Intermediate Compound in Oxidative Degradation of Dehydro-L-Ascorbic Acid and 2,3-Diketo-L-Gulonic Acid in a Deuterium Oxide Phosphate Buffer. *Biosci. Biotechnol. Biochem.* **2001**, *65*, 1707–1712. 10.1271/bbb.65.1707.

(133) Simpson, G. L. W.; Ortwerth, B. J. The Non-Oxidative Degradation of Ascorbic Acid at Physiological Conditions. *Biochim. Biophys. Acta - Mol. Basis Dis.* **2000**, *1501*, 12–24. 10.1016/S0925-4439(00)00009-0.

(134) Kurata, T.; Nishikawa, Y. Chemical Characteristics of Dehydro-L-Ascorbic Acid. *Biosci. Biotechnol. Biochem.* **2000**, *64*, 1651–1655. 10.1271/bbb.64.1651.

(135) Deutsch, J. C. Spontaneous Hydrolysis and Dehydration of Dehydroascorbic Acid in Aqueous Solution. *Anal. Biochem.* **1998**, *260*, 223–229. 10.1006/abio.1998.2700.

(136) Mujika, J. I.; Matxain, J. M. Theoretical Study of the PH-Dependent Antioxidant Properties of Vitamin C. *J. Mol. Model.* **2013**, *19*, 1945–1952. 10.1007/s00894-012-1465-5.

(137) Kushner, D. J.; Baker, A.; Dunstall, T. G. Pharmacological Uses and Perspectives of Heavy Water and Deuterated Compounds. *Can. J. Physiol. Pharmacol.* **1999**, *77*, 79–88. 10.1139/y99-005.

(138) Rangappa, K. S.; Raghavendra, M. P.; Mahadevappa, D. S.; Gowda, D. C. Kinetics and Mechanism of Oxidation of Erythro-Series Pentoses and Hexoses by N-Chloro-p-Toluenesulfonamide. *Carbohydr. Res.* **1998**, *306*, 57–67. 10.1016/S0008-6215(97)00243-7.

(139) Bielski, B. H. J. Chemistry of Ascorbic Acid Radicals. In *Ascorbic Acid: Chemistry, Metabolism, and Uses*; Advances in Chemistry; American Chemical Society, 1982; Vol. 200, pp 81–100. 10.1021/ba-1982-0200.ch004.

(140) Deakin, M. R.; Kovach, P. M.; Stutts, K. J.; Wightman, R. M. Heterogeneous Mechanisms of the Oxidation of Catechols and Ascorbic Acid at Carbon Electrodes. *Anal. Chem.* **1986**, *58*, 1474–1480. 10.1021/ac00298a046.

(141) Bielski, B. H. J.; Allen, A. O.; Schwarz, H. A. Mechanism of Disproportionation of Ascorbate Radicals. *J. Am. Chem. Soc.* **1981**, *103*, 3516–3518. 10.1021/ja00402a042.

(142) Kerber, R. C. "As Simple as Possible, but Not Simpler"—The Case of Dehydroascorbic Acid. *J. Chem. Educ.* **2008**, *85*, 1237. 10.1021/ed085p1237.

(143) Nishikawa, Y.; Kurata, T. Interconversion between Dehydro-L-Ascorbic Acid and L-Ascorbic Acid. *Biosci. Biotechnol. Biochem.* **2000**, *64*, 476–483. 10.1271/bbb.64.476.

(144) Sapper, H.; Institut für Biophysik der Justus-L, S.-O.; Paul, H.-H.; Lohmann, W. The Reversibility of the Vitamin C Redox System: Electrochemical Reasons and Biological Aspects. *Z. Naturforsch. C* **1982**, *37*, 942–946. 10.1515/znc-1982-1015.

(145) Tu, Y.-J.; Njus, D.; Schlegel, H. B. A Theoretical Study of Ascorbic Acid Oxidation and $HOO^{\cdot}$/ $O_2^{\cdot-}$ Radical Scavenging. *Org. Biomol. Chem.* **2017**, *15*, 4417–4431. 10.1039/C7OB00791D.

(146) Matsui, T.; Kitagawa, Y.; Okumura, M.; Shigeta, Y. Accurate Standard Hydrogen Electrode Potential and Applications to the Redox Potentials of Vitamin C and NAD/NADH. *J. Phys. Chem. A* **2015**, *119*, 369–376. 10.1021/jp508308y.

(147) Bichara, L. C.; Brandán, S. A. Hydration of Species Derived from Ascorbic Acid in Aqueous Solution. An Experimental and Theoretical Study by Using DFT Calculations. *J. Mol. Liq.* **2013**, *181*, 34–43. 10.1016/j.molliq.2013.02.009.

(148) Laroff, G. P.; Fessenden, R. W.; Schuler, R. H. The Electron Spin Resonance Spectra of Radical Intermediates in the Oxidation of Ascorbic Acid and Related Substances. *J. Am. Chem. Soc.* **1972**, *94*, 9062–9073. 10.1021/ja00781a013.

(149) Williams, N. H.; Yandell, J. K. Outer-Sphere Electron-Transfer Reactions of Ascorbate Anions. *Aust. J. Chem.* **1982**, *35*, 1133–1144. 10.1071/CH9821133.

(150) Steenken, S.; Neta, P. Electron Transfer Rates and Equilibriums between Substituted Phenoxide Ions and Phenoxyl Radicals. *J. Phys. Chem.* **1979**, *83*, 1134–1137. 10.1021/j100472a005.

(151) Tur'yan, Y. I.; Kohen, R. Formal Redox Potentials of the Dehydro-l-Ascorbic Acid/l-Ascorbic Acid System. *J. Electroanal. Chem.* **1995**, *380*, 273–277. 10.1016/0022-0728(94)03524-7.

(152) Bode, A. M.; Cunningham, L.; Rose, R. C. Spontaneous Decay of Oxidized Ascorbic Acid (Dehydro-l-Ascorbic Acid) Evaluated by High-Pressure Liquid Chromatography. *Clin. Chem.* **1990**, *36*, 1807–1809. clinchem.aaccjnls.org/content/36/10/1807.long.

(153) Nagaraj, R. H.; Monnier, V. M. Protein Modification by the Degradation Products of Ascorbate: Formation of a Novel Pyrrole from the Maillard Reaction of l-Threose with Proteins. *Biochim. Biophys. Acta (BBA)/Protein Struct. Mol.* **1995**, *1253*, 75–84. 10.1016/0167-4838(95)00161-M.

(154) Cayuela, A.; Soriano, M. L.; Carrillo-Carrión, C.; Valcárcel, M. Semiconductor and Carbon-Based Fluorescent Nanodots: The Need for Consistency. *Chem. Commun.* **2016**, *52*, 1311–1326. 10.1039/c5cc07754k.

(155) Zuo, P.; Lu, X.; Sun, Z.; Guo, Y.; He, H. A Review on Syntheses, Properties, Characterization and Bioanalytical Applications of Fluorescent Carbon Dots. *Microchim. Acta* **2016**, *183*, 519–542. 10.1007/s00604-015-1705-3.

(156) Lim, S. Y.; Shen, W.; Gao, Z. Carbon Quantum Dots and Their Applications. *Chem. Soc. Rev.* **2015**, *44*, 362–381. 10.1039/c4cs00269e.

(157) Gupta, S.; Smith, T.; Banaszak, A.; Boeckl, J. Graphene Quantum Dots Electrochemistry and Sensitive Electrocatalytic Glucose Sensor Development. *Nanomaterials* **2017**, *7*, 301. 10.3390/nano7100301.

(158) Liu, H.; Li, Z.; Sun, Y.; Geng, X.; Hu, Y.; Meng, H.; Ge, J.; Qu, L. Synthesis of Luminescent Carbon Dots with Ultrahigh Quantum Yield and Inherent Folate Receptor-Positive Cancer Cell Targetability. *Sci. Rep.* **2018**, *8*, 1086. 10.1038/s41598-018-19373-3.

(159) Bianco, A.; Cheng, H. M.; Enoki, T.; Gogotsi, Y.; Hurt, R. H.; Koratkar, N.; Kyotani, T.; Monthioux, M.; Park, C. R.; Tascon, J. M. D.; et al. All in the Graphene Family - A Recommended Nomenclature for Two-Dimensional Carbon Materials. *Carbon N. Y.* **2013**, *65*, 1–6. 10.1016/j.carbon.2013.08.038.

(160) Georgakilas, V.; Perman, J. A.; Tucek, J.; Zboril, R. Broad Family of Carbon Nanoallotropes: Classification, Chemistry, and Applications of Fullerenes, Carbon Dots, Nanotubes, Graphene, Nanodiamonds, and Combined Superstructures. *Chem. Rev.* **2015**, *115*, 4744–4822. 10.1021/cr500304f.

(161) Wu, B. R. Field Modulation of the Electronic Structure of Trilayer Graphene. *Appl. Phys. Lett.* **2011**, *98*, 263107. 10.1063/1.3604019.

(162) Haque, E.; Kim, J.; Malgras, V.; Reddy, K. R.; Ward, A. C.; You, J.; Bando, Y.; Hossain, M. S. A.; Yamauchi, Y. Recent Advances in Graphene Quantum Dots: Synthesis, Properties, and Applications. *Small Methods* **2018**, *2*, 1800050. 10.1002/smtd.201800050.

(163) Dong, Y.; Lin, J.; Chen, Y.; Fu, F.; Chi, Y.; Chen, G. Graphene Quantum Dots, Graphene Oxide, Carbon Quantum Dots and Graphite Nanocrystals in Coals. *Nanoscale* **2014**, *6*, 7410–7415. 10.1039/c4nr01482k.

(164) Cailotto, S.; Amadio, E.; Facchin, M.; Selva, M.; Pontoglio, E.; Rizzolio, F.; Riello, P.; Toffoli, G.; Benedetti, A.; Perosa, A. Carbon-Dots from Sugars and Ascorbic Acid: Role of the Precursors on Morphology, Properties, Toxicity and Drug Uptake. *ACS Med. Chem. Lett.* **2018**, *9*, 832–837. 10.1021/acsmedchemlett.8b00240.

(165) Cao, L.; Meziani, M. J.; Sahu, S.; Sun, Y. P. Photoluminescence Properties of Graphene versus Other Carbon Nanomaterials. *Acc. Chem. Res.* **2013**, *46*, 171–182. 10.1021/ar300128j.

(166) Shen, J.; Zhu, Y.; Yang, X.; Li, C. Graphene Quantum Dots: Emergent Nanolights for Bioimaging, Sensors, Catalysis and Photovoltaic Devices. *Chem. Commun.* **2012**, *48*, 3686–3699. 10.1039/c2cc00110a.

(167) Ping, J.; Wu, J.; Wang, Y.; Ying, Y. Simultaneous Determination of Ascorbic Acid, Dopamine and Uric Acid Using High-Performance Screen-Printed Graphene Electrode. *Biosens. Bioelectron.* **2012**, *34*, 70–76. 10.1016/j.bios.2012.01.016.

(168) Wang, Y.; Hu, A. Carbon Quantum Dots: Synthesis, Properties and Applications. *J. Mater. Chem. C* **2014**, *2*, 6921–6939. 10.1039/c4tc00988f.

(169) Jia, X.; Li, J.; Wang, E. One-Pot Green Synthesis of Optically PH-Sensitive Carbon Dots with Upconversion Luminescence. *Nanoscale* **2012**, *4*, 5572–5575. 10.1039/c2nr31319g.

(170) Radovic, L. R.; Bockrath, B. On the Chemical Nature of Graphene Edges: Origin of Stability and Potential for Magnetism in Carbon Materials. *J. Am. Chem. Soc.* **2005**, *127*, 5917–5927. 10.1021/ja050124h.

(171) Gokus, T.; Nair, R. R.; Bonetti, A.; Böhmler, M.; Lombardo, A.; Novoselov, K. S.; Geim, A. K.; Ferrari, A. C.; Hartschuh, A. Making Graphene Luminescent by Oxygen Plasma Treatment. *ACS Nano* **2009**, *3*, 3963–3968. 10.1021/nn9012753.

(172) Sun, Y. P.; Zhou, B.; Lin, Y.; Wang, W.; Fernando, K. A. S.; Pathak, P.; Meziani, M. J.; Harruff, B. A.; Wang, X.; Wang, H.; et al. Quantum-Sized Carbon Dots for Bright and Colorful Photoluminescence. *J. Am. Chem. Soc.* **2006**, *128*, 7756–7757. 10.1021/ja062677d.

(173) Wang, S.; Talirz, L.; Pignedoli, C. A.; Feng, X.; Müllen, K.; Fasel, R.; Ruffieux, P. Giant Edge State Splitting at Atomically Precise Graphene Zigzag Edges. *Nat. Commun.* **2016**, *7*, 11507. 10.1038/ncomms11507.

(174) Pan, D.; Zhang, J.; Li, Z.; Wu, M. Hydrothermal Route for Cutting Graphene Sheets into Blue-Luminescent Graphene Quantum Dots. *Adv. Mater.* **2010**, *22*, 734–738. 10.1002/adma.200902825.

(175) Xu, X.; Ray, R.; Gu, Y.; Ploehn, H. J.; Gearheart, L.; Raker, K.; Scrivens, W. A. Electrophoretic Analysis and Purification of Fluorescent Single-Walled Carbon Nanotube Fragments. *J. Am. Chem. Soc.* **2004**, *126*, 12736–12737. 10.1021/ja040082h.

(176) Kakaei, K.; Javan, H.; Mohammadi, H. B. Synthesis of Carbon Quantum Dots Nanoparticles by Cyclic Voltammetry and Its Application as Methanol Tolerant Oxygen Reduction Reaction Electrocatalyst. *J. Chinese Chem. Soc.* **2016**, *63*, 432–437. 10.1002/jccs.201500534.

(177) Wang, S.; Cole, I. S.; Zhao, D.; Li, Q. The Dual Roles of Functional Groups in the Photoluminescence of Graphene Quantum Dots. *Nanoscale* **2016**, *8*, 7449–7458. 10.1039/C5NR07042B.

(178) Han, L.; Ghosh, D.; Chen, W.; Pradhan, S.; Chang, X.; Chen, S. Nanosized Carbon Particles from Natural Gas Soot. *Chem. Mater.* **2009**, *21*, 2803–2809. 10.1021/cm900709w.

(179) Li, D.; Han, D.; Qu, S. N.; Liu, L.; Jing, P. T.; Zhou, D.; Ji, W. Y.; Wang, X. Y.; Zhang, T. F.; Shen, D. Z. Supra-(Carbon Nanodots) with a Strong Visible to near-Infrared Absorption Band and Efficient Photothermal Conversion. *Light Sci. Appl.* **2016**, *5*, 1–8. 10.1038/lsa.2016.120.

(180) Gong, J.; An, X.; Yan, X. A Novel Rapid and Green Synthesis of Highly Luminescent Carbon Dots with Good Biocompatibility for Cell Imaging. *New J. Chem.* **2014**, *38*, 1376–1379. 10.1039/c3nj01320k.

(181) Nawaz, F.; Wang, L.; Zhu, L. feng; Meng, X. ju; Xiao, F. S. Ascorbic Acid Assisted Green Route for Synthesis of Water Dispersible Carbon Dots. *Chem. Res. Chinese Univ.* **2013**, *29*, 401–403. 10.1007/s40242-013-2339-9.

(182) Zhang, B.; Liu, C.; Liu, Y. A Novel One-Step Approach to Synthesize Fluorescent Carbon Nanoparticles. *Eur. J. Inorg. Chem.* **2010**, *2010*, 4411–4414. 10.1002/ejic.201000622.

(183) Zhu, H.; Wang, X.; Li, Y.; Wang, Z.; Yang, F.; Yang, X. Microwave Synthesis of Fluorescent Carbon Nanoparticles with Electrochemiluminescence Properties. *Chem. Commun.* **2009**, *0*, 5118–5120. 10.1039/b907612c.

(184) Liu, R.; Wu, D.; Feng, X.; Müllen, K. Bottom-up Fabrication of Photoluminescent Graphene Quantum Dots with Uniform Morphology. *J. Am. Chem. Soc.* **2011**, *133*, 15221–15223. 10.1021/ja204953k.

(185) Yan, X.; Cui, X.; Li, L. S. Synthesis of Large, Stable Colloidal Graphene Quantum Dots with Tunable Size. *J. Am. Chem. Soc.* **2010**, *132*, 5944–5945. 10.1021/ja1009376.

(186) De, B.; Karak, N. A Green and Facile Approach for the Synthesis of Water Soluble Fluorescent Carbon Dots from Banana Juice. *RSC Adv.* **2013**, *3*, 8286–8290. 10.1039/c3ra00088e.

(187) Li, H.; Shao, F. Q.; Zou, S. Y.; Yang, Q. J.; Huang, H.; Feng, J. J.; Wang, A. J. Microwave-Assisted Synthesis of N,P-Doped Carbon Dots for Fluorescent Cell Imaging. *Microchim. Acta* **2016**, *183*, 821–826. 10.1007/s00604-015-1714-2.

(188) Li, H.; He, X.; Liu, Y.; Huang, H.; Lian, S.; Lee, S. T.; Kang, Z. One-Step Ultrasonic Synthesis of Water-Soluble Carbon Nanoparticles with Excellent Photoluminescent Properties. *Carbon N. Y.* **2011**, *49*, 605–609. 10.1016/j.carbon.2010.10.004.

(189) Jin, L.; Yang, S. P.; Tian, Q. W.; Wu, H. X.; Cai, Y. J. Preparation and Characterization of Copper Metal Nanoparticles Using Dendrimers as Protectively Colloids. *Mater. Chem. Phys.* **2008**, *112*, 977–983. 10.1016/j.matchemphys.2008.06.073.

(190) Berridge, M. V.; Herst, P. M.; Tan, A. S. Tetrazolium Dyes as Tools in Cell Biology: New Insights into Their Cellular Reduction. In *Biotechnology Annual Review*; Elsevier, 2005; Vol. 11, pp 127–152. 10.1016/S1387-2656(05)11004-7.

(191) Stockert, J. C.; Horobin, R. W.; Colombo, L. L.; Blázquez-Castro, A. Tetrazolium Salts and Formazan Products in Cell Biology: Viability Assessment, Fluorescence Imaging, and Labeling Perspectives. *Acta Histochem.* **2018**, *120*, 159–167. 10.1016/j.acthis.2018.02.005.

(192) Menges, F. Spectragryph - Optical Spectroscopy Software, version 1.2.9, 2018, effemm2.de/spectragryph.

(193) Schindelin, J.; Arganda-Carreras, I.; Frise, E.; Kaynig, V.; Longair, M.; Pietzsch, T.; Preibisch, S.; Rueden, C.; Saalfeld, S.; Schmid, B.; et al. Fiji: An Open-Source Platform for Biological-Image Analysis. *Nat. Methods* **2012**, *9*, 676–682. 10.1038/nmeth.2019.

(194) Rueden, C. T.; Schindelin, J.; Hiner, M. C.; DeZonia, B. E.; Walter, A. E.; Arena, E. T.; Eliceiri, K. W. ImageJ2: ImageJ for the next Generation of Scientific Image Data. *BMC Bioinformatics* **2017**, *18*, 529. 10.1186/s12859-017-1934-z.

(195) Eliceiri, K.; Schneider, C. A.; Rasband, W. S.; Eliceiri, K. W. NIH Image to ImageJ : 25 Years of Image Analysis Historical Commentary NIH Image to ImageJ : 25 Years of Image Analysis. *Nat. Methods* **2012**, *9*, 671–675. 10.1038/nmeth.2089.

(196) Hotaling, N. A.; Bharti, K.; Kriel, H.; Simon, C. G. DiameterJ: A Validated Open Source Nanofiber Diameter Measurement Tool. *Biomaterials* **2015**, *61*, 327–338. 10.1016/j.biomaterials.2015.05.015.

(197) Kleinwächter, M.; Selmar, D. A Novel Approach for Reliable Activity Determination of Ascorbic Acid Depending Myrosinases. *J. Biochem. Biophys. Methods* **2004**, *59*, 253–265. 10.1016/j.jbbm.2004.03.005.

(198) Newkome, G. R.; Shreiner, C. D. Poly(Amidoamine), Polypropylenimine, and Related Dendrimers and Dendrons Possessing Different 1 → 2 Branching Motifs: An Overview of the Divergent Procedures. *Polymer (Guildf).* **2008**, *49*, 1–173. 10.1016/j.polymer.2007.10.021.

(199) Gomez, M. V.; Guerra, J.; Velders, A. H.; Crooks, R. M. NMR Characterization of Fourth-Generation PAMAM Dendrimers in the Presence and Absence of Palladium Dendrimer-Encapsulated Nanoparticles. *J. Am. Chem. Soc.* **2009**, *131*, 341–350. 10.1021/ja807488d.

(200) Song, G.; Lin, Y.; Zhu, Z.; Zheng, H.; Qiao, J.; He, C.; Wang, H. Strong Fluorescence of Poly (N-Vinylpyrrolidone) and Its Oxidized Hydrolyzate. *Macromol. Rapid Commun.* **2015**, *36*, 278–285. 10.1002/marc.201400516.

(201) Konopka, M.; Janaszewska, A.; Klajnert-Maculewicz, B. Intrinsic Fluorescence of PAMAM Dendrimers-Quenching Studies. *Polymers (Basel).* **2018**, *10*, 540. 10.3390/polym10050540.

(202) Ji, Y.; Yang, X.; Qian, Y. Poly-Amidoamine Structure Characterization: Amide Resonance Structure of Imidic Acid (HO-CN) and Tertiary Ammonium. *RSC Adv.* **2014**, *4*, 49535–49540. 10.1039/c4ra09081k.

(203) Ji, Y.; Qian, Y. A Study Using Quantum Chemical Theory Methods on the Intrinsic Fluorescence Emission and the Possible Emission Mechanisms of PAMAM. *RSC Adv.* **2014**, *4*, 58788–58794. 10.1039/c4ra09184a.

(204) Lee, W. I.; Bae, Y.; Bard, A. J. Strong Blue Photoluminescence and ECL from OH-Terminated PAMAM Dendrimers in the Absence of Gold Nanoparticles. *J. Am. Chem. Soc.* **2004**, *126*, 8358–8359. 10.1021/ja0475914.

(205) Larson, C. L.; Tucker, S. A. Intrinsic Fluorescence of Carboxylate-Terminated Polyamido Amine Dendrimers. *Appl. Spectrosc.* **2001**, *55*, 679–683. 10.1366/0003702011952596.

(206) Wang, D.; Imae, T. Fluorescence Emission from Dendrimers and Its PH Dependence. *J. Am. Chem. Soc.* **2004**, *126*, 13204–13205. 10.1021/ja0454992.

(207) Martins, I. J. V. Carboxylated and Aminated Carbon Dots: Hydrothermal Synthesis, Photostability, and DNA Interaction Studies, University of Madeira, 2018, hdl.handle.net/10400.13/2106.

(208) Park, S.; An, J.; Piner, R. D.; Jung, I.; Yang, D.; Velamakanni, A.; Nguyen, S. T.; Ruoff, R. S. Aqueous Suspension and Characterization of Chemically Modified Graphene Sheets. *Chem. Mater.* **2008**, *20*, 6592–6594. 10.1021/cm801932u.

(209) Matassa, R.; Terranova, M. L.; Orlanducci, S.; Passeri, D.; Rossi, M.; Sordi, D.; Tamburri, E.; Guglielmotti, V. Characterization of Carbon Structures Produced by Graphene Self-Assembly. *J. Appl. Crystallogr.* **2014**, *47*, 222–227. 10.1107/s1600576713029488.

(210) You, Y.; Zhang, H.; Liu, Y.; Lei, B. Transparent Sunlight Conversion Film Based on Carboxymethyl Cellulose and Carbon Dots. *Carbohydr. Polym.* **2016**, *151*, 245–250. 10.1016/j.carbpol.2016.05.063.

(211) Tan, X.; Li, Y.; Li, X.; Zhou, S.; Fan, L.; Yang, S. Electrochemical Synthesis of Small-Sized Red Fluorescent Graphene Quantum Dots as a Bioimaging Platform. *Chem. Commun.* **2015**, *51*, 2544–2546. 10.1039/c4cc09332a.

(212) Ingle, A. P.; Duran, N.; Rai, M. Bioactivity, Mechanism of Action, and Cytotoxicity of Copper-Based Nanoparticles: A Review. *Appl. Microbiol. Biotechnol.* **2014**, *98*, 1001–1009. 10.1007/s00253-013-5422-8.

(213) Hejazy, M.; Koohi, M. K.; Bassiri Mohamad Pour, A.; Najafi, D. Toxicity of Manufactured Copper Nanoparticles - A Review. *Nanomedicine Res. J.* **2018**, *3*, 1–9. 10.22034/NMRJ.2018.01.001.

(214) Keller, A. A.; Adeleye, A. S.; Conway, J. R.; Garner, K. L.; Zhao, L.; Cherr, G. N.; Hong, J.; Gardea-Torresdey, J. L.; Godwin, H. A.; Hanna, S.; et al. Comparative Environmental Fate and Toxicity of Copper Nanomaterials. *NanoImpact* **2017**, *7*, 28–40. 10.1016/j.impact.2017.05.003.

(215) Algarra, M.; Pérez-Martín, M.; Cifuentes-Rueda, M.; Jiménez-Jiménez, J.; Esteves Da Silva, J. C. G.; Bandosz, T. J.; Rodríguez-Castellón, E.; López Navarrete, J. T.; Casado, J. Carbon Dots Obtained Using Hydrothermal Treatment of Formaldehyde. Cell Imaging in Vitro. *Nanoscale* **2014**, *6*, 9071–9077. 10.1039/c4nr01585a.

(216) Ray, S. C.; Saha, A.; Jana, N. R.; Sarkar, R. Fluorescent Carbon Nanoparticles: Synthesis, Characterization, and Bioimaging Application. *J. Phys. Chem. C* **2009**, *113*, 18546–18551. 10.1021/jp905912n.

6 Annexes

Annex 1

➢ Here some considerations about the dimerization process of the ascorbate radical are presented (adapted from Schlegel *et. al.* [145]).

- Direct electron transfer between two $A^{\bullet -}$ is not favorable.
  - It would yield higher energy products, DHA_1 and A^{2-}, which would make it endothermic.
    - Calculated ΔG = 7.75 kcal/mol.
- Protonation, hydration and/or cyclization of $A^{\bullet -}$ before electron transfer is also endothermic because these reactions destroy the delocalization of the unpaired electron in the radical.
  - Bielski *et al.* [141] proposed that two $A^{\bullet -}$ disproportionate by forming a dimer.
    - Estimated ΔG = −4.1 kcal/mol, and dimerization constant, $K \approx 10^3$.
  - Schlegel *et. al.* [145] propose the dimer structure shown in **Fig. 53**.
    - Calculated ΔG = −1.28 kcal/mol.
    - It permits the transfer of the unpaired electron from one unit to the other.
    - It allows the cyclization of the donor unit.

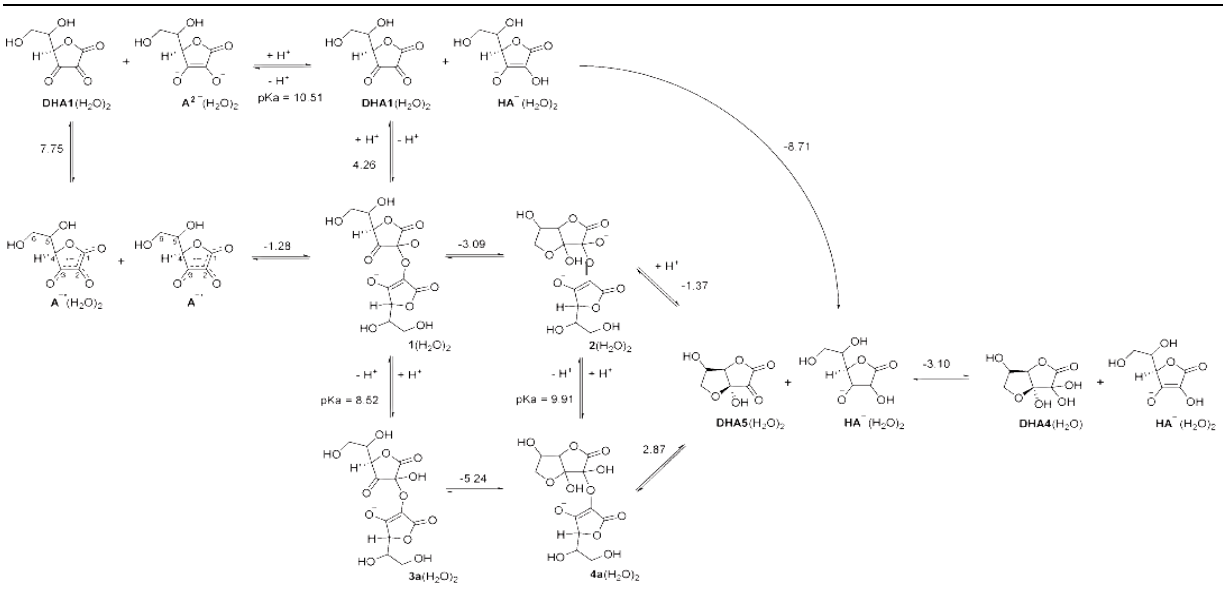

Fig. 53. The mechanism for the dimerization of the ascorbate radical (adapted from [145]).

- Dissociation of the uncyclized dimer to form DHA_1 and HA^- is unfavorable, but one of the fragments of the dimer can cyclize (calculated: ΔG = 4.26 kcal/mol).
  - Estimated $\Delta G_{(cyclization)}$ = −3.09 kcal/mol for the unprotonated dimer, dimer $_{(1\rightarrow 2)}$.
  - Estimated $\Delta G_{(cyclization)}$ = −5.24 kcal/mol for the protonated dimer, dimer $_{(3a\rightarrow 4a)}$.
- Dimer $_{(2)}$ can dissociate to DHA_5 and HA^- which is exothermic (calculated ΔG = −1.37 kcal/mol) but endothermic for the dimer $_{(4a)}$ (calculated ΔG = 2.87 kcal/mol).
  - The calculated pKa of the dimer is 8.52, which is in accordance with the pH dependence of the disproportionation rate observed by Bielski *et al*. [141].
- Hydration of the bond in carbon-2 of the DHA_5 yields the final products, DHA_4 and HA^-.

Annex 2

- Average size of the liquid-phase from the PVP route, pH=4 at different PVP and AA ratios:

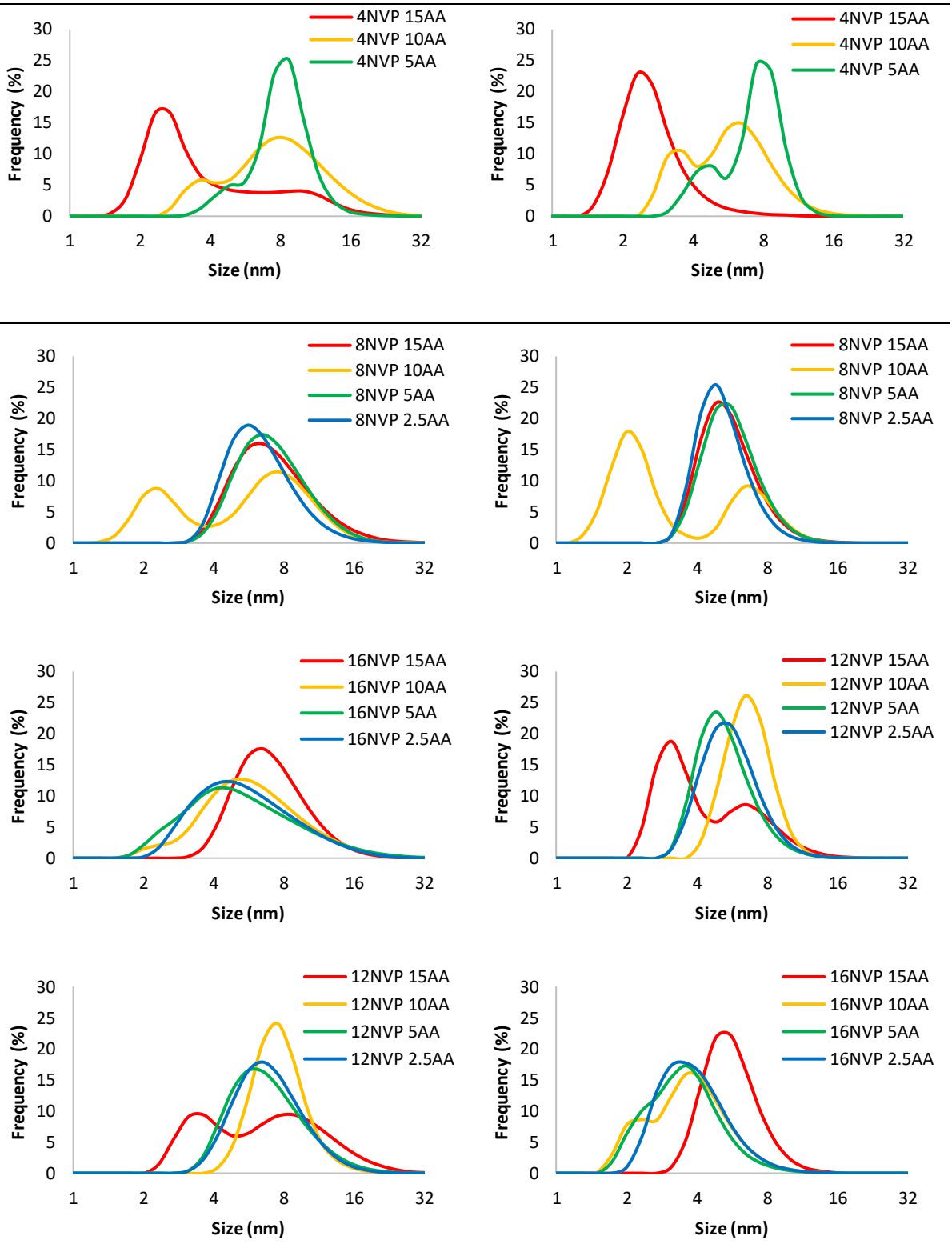

Fig. 54. Distribution analysis (**Left column**) by Volume and (**Right column**) by Number. Liquid-phase from the PVP route at pH=4. Samples were diluted at 1:10 with Mili-Q water (mean, n=3).

Annex 3

Stability study of the Cu^{2+}-PAMAM complex at different pH values over time

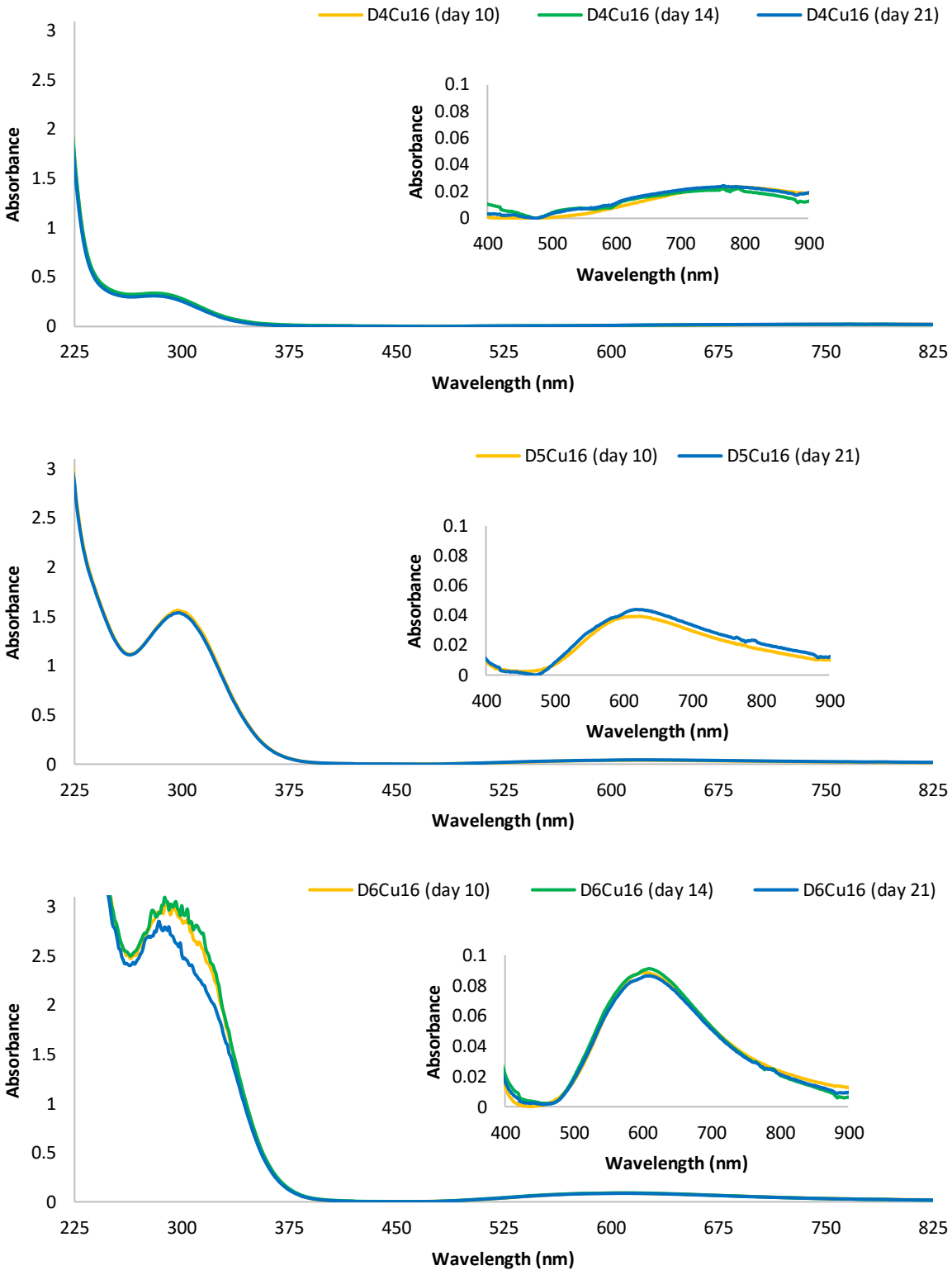

Fig. 55. UV-Vis spectra of Cu^{2+}-DENPs solutions at (**top**) pH 4, (**middle**) pH 5, and (**bottom**) pH 6.

PEst-OE/QUI/UI0674/2013

M1420-01-0145-FEDER-000005

Centro de Química da Madeira - CQM^{+} (Madeira 14-20 Program).

Cofinanciado por:

A Nossa Universidade

Colégio dos Jesuítas
Rua dos Ferreiros - 9000-082, Funchal

Tel: +351 291 209400
Fax: +351 291 209410
Email: gabinetedareitoria@uma.pt